Volume 6 Issue 1

MERSIN PHOTOGRAMMETRY JOURNAL

The MERSİN PHOTOGRAMMETRY JOURNAL (MEPHOJ)

THE MERSİN PHOTOGRAMMETRY JOURNAL (MEPHOJ) publishes original and innovative contributions in photogrammetric applications ranging from the integration of instruments, methodologies, and technologies and their respective uses in the environmental sciences, engineering, and other natural sciences. Mersin Photogrammerty Journal is a branch of science that widely applied in many scientific disciplines. MEPHOJ aims to cover the entirety of Photogrammetry and Photogrammetric aplications about Geosciences, including their application domains. MEPHOJ strives to encourage scientists to publish experimental, theoretical, and computational results as detailed as possible so that results can be easily reproduced.

MEPHOJ is a double peer-reviewed (blind) OPEN ACCESS JOURNAL that publishes professional level research articles and subject reviews exclusively in English. It allows authors to submit articles online and track his or her progress via its web interface. All manuscripts will undergo a refereeing process; acceptance for publication is based on at least two positive reviews. The journal publishes research and review papers, professional communication, and technical notes. MEPHOJ does not charge for any article submissions or for processing.

CORRESPONDENCE ADDRESS
Journal Contact: myakar@mersin.edu.tr

CONTENTS

Volume 6 - Issue 1

RESEARCH ARTICLES

Mersin Photogrammetry Journal

https://dergipark.org.tr/en/pub/mephoj

e-ISSN 2687-654X

UAV-based topographical mapping and accuracy assessment of orthophoto using GCP

Sagar Pathak [*1], Samrat Acharya [1], Saugat Bk [1], Gaurab Karn [1], Ujjowl Thapa [1]

[1]*Kathmandu University, Department of Geomatics Engineering, Nepal,* sgrpathak2001@gmail.com, samratacharya088@gmail.com, bksaugat975@gmail.com, gauravkarn789@gmail.com, ujjwolthapa23@gmail.com

Cite this study: Pathak, S., Acharya, S., Bk, S., Karn, G., & Thapa, U. (2024). UAV-based topographical mapping and accuracy assessment of orthophoto using GCP. Mersin Photogrammetry Journal, 6(1), 1-8

https://doi.org/10.53093/mephoj.1350426

Keywords
UAV
DSM
DTM
Orthophoto
GCP

Research Article

Received: 26.08.2023
Revised: 05.10.2023
Accepted:09.10.2023
Published:16.03.2024

Abstract

For smaller locations, the traditional aerial photogrammetry techniques utilizing helicopters or airplanes are expensive and difficult. A new competitive strategy is necessary for quick spatial data collecting at a low cost and in a short amount of time for a developing nation like Nepal where geospatial data is in great demand. Currently, the Unmanned Aerial Vehicle (UAV) has become an alternative for different engineering applications, especially in surveying, one of these applications is for making a topographical map. This study demonstrates how this can be achieved using one of the evolving remote sensing technologies, Unmanned Aerial Vehicles (UAV). Besides, this study also involves image processing and topographic map production using Pix4D and GIS environments. For this study, the DJI Mavic Air-2 Advanced quadcopter collected about 207 images at a flying height of 80 m above the Kathmandu University area. An orthophoto of 2.4 cm GSD covering 127064 sq. Meter of the area was produced. The RMSE of 5.37 cm in X 4.94 cm in Y and 6.1 cm in Z was achieved with appropriate checkpoints. The measurements in the orthophoto replicated the field measurements to an error of less than 0.5% of the actual dimensions.

1. Introduction

Topographical maps are the types of maps that show detailed ground relief, including landforms and scenery, drainage (lakes and streams), forest cover, administrative zones, and population areas, as well as transportation routes, structures (including streets and railroads), and other man-made features. For roads, railroads, canals, pipelines, transmission lines, reservoirs, and other facilities, engineers utilize them to determine the most desirable and cost-effective locations. They are also utilized in soil conservation work by architects, geologists, and agriculturalists. Topographical maps are necessary because they contain basic map features such as earth surface terrain information with respect to their proper geometric accuracy. The use of geospatial data, using a topographic map as a base reference, is mandatory to ensure accurate rapid response to emergencies, often referred to as quick mapping. This critical aspect marked the beginning of worldwide cooperation under the International Charter on Space and Major Disasters, in which the use of satellite data, including data from very high resolution (VHRS) will indeed be provided immediately during major catastrophes around the world [1,2].

Topographical mapping is the first application of surveying, and it is a method that is constantly evolving. With the rapid advancement of computer vision science and the increasing use of small unmanned aerial vehicles (UAVs), photogrammetry has shown incredible potential in providing topographic information with comparable resolution and precision to lidar surveys, but at a much lower cost. By using photogrammetry techniques, UAV surveys produce orthophotos that are georeferenced and then further processed for geographic data with the aid of software [3].UAVs are aircraft that can either fly autonomously using pre-programmed flight plans or more advanced dynamic automation systems, or they can fly remotely controlled by a pilot at a ground station. The creation of high-resolution, high-quality digital elevation models (DEMs) demands a large investment in staff time, technology, and/or software despite the variety of accessible approaches However, image-based methods such as digital photogrammetry have been decreasing in costs [2].

In recent years, advances in technology have allowed for the creation of more accurate and detailed topographical maps of Nepal. The use of satellite imagery and GPS has made it possible to create high-resolution digital maps that are more accurate and up-to-date than

ever before. These digital maps are used for a variety of purposes, including land use planning, resource management, and disaster preparedness. This study seeks to address the use of drone technology and the GIS environment how efficient and effective of this technology in mapping operations and what is the difficulties faced by this approach, if any.

For surveillance and reconnaissance reasons during World Wars I & II, the US military developed the unmanned aerial vehicle (UAV) in prototype form. From the 1960s to 1980s in the early 20th century, UAV was frequently deployed [4]. In the past few years, unmanned aerial vehicles (UAV) or drones have been a hot topic encompassing technology, security issues, rules, and regulations globally due to its remarkable advancements and uses in remote sensing and photogrammetry applications. The largest percentage of uses for unmanned aerial vehicles is in agriculture and infrastructure. Autonomous UAV use in agriculture is expanding quickly in areas including crop health monitoring, early warning systems, forestry, fisheries, and wildlife protection [5,6]. The two main types of UAVs are rotary-wing and fixed-wing. Fixed-wing UAVs function similarly to small unmanned aircraft in terms of structure, rotary-wing UAVs also known as multirotor, rotorcraft, or multi-copter UAVs are comparable to small unmanned helicopters Propellers, which are fans that provide thrust by rotating rotor blades on a rotor mast, provide lift for these craft. But unlike helicopters, which normally have a single rotor with two blades, most rotary-wing UAVs need more than one rotor to handle the forces placed on the rotor blades during flight [7,8]. According to the American Society for Photogrammetry and Remote Sensing, photogrammetry is the art, science, and technology of gathering accurate data about real-world objects and their surroundings through the recording, measuring, and interpretation of photographic images and patterns of electromagnetic radiation and other phenomena [9]. To accurately establish the geometric relationship between the image and the object as it appeared at the time of the imaging event is the crucial task of photogrammetry. Once this connection has been appropriately established, it is possible to infer details about an object just from its images [10]. In aerial triangulation, integrating GPS/inertial orientations offers flexibility and high accuracy [11]. The Direct Georeferencing method achieves 1:5000 scale accuracy, reducing reliance on Ground Control Points (GCPs) while maintaining precision [12,13].

2. Study area

The study area for the study is the Kathmandu University premises which is located in Dhulikhel Municipality (Figure 1). The university has an area of 35518 square meters. The area of study consists of an undulating terrain, vegetation, a settlement area, roads, departmental and administrative buildings, and water bodies.

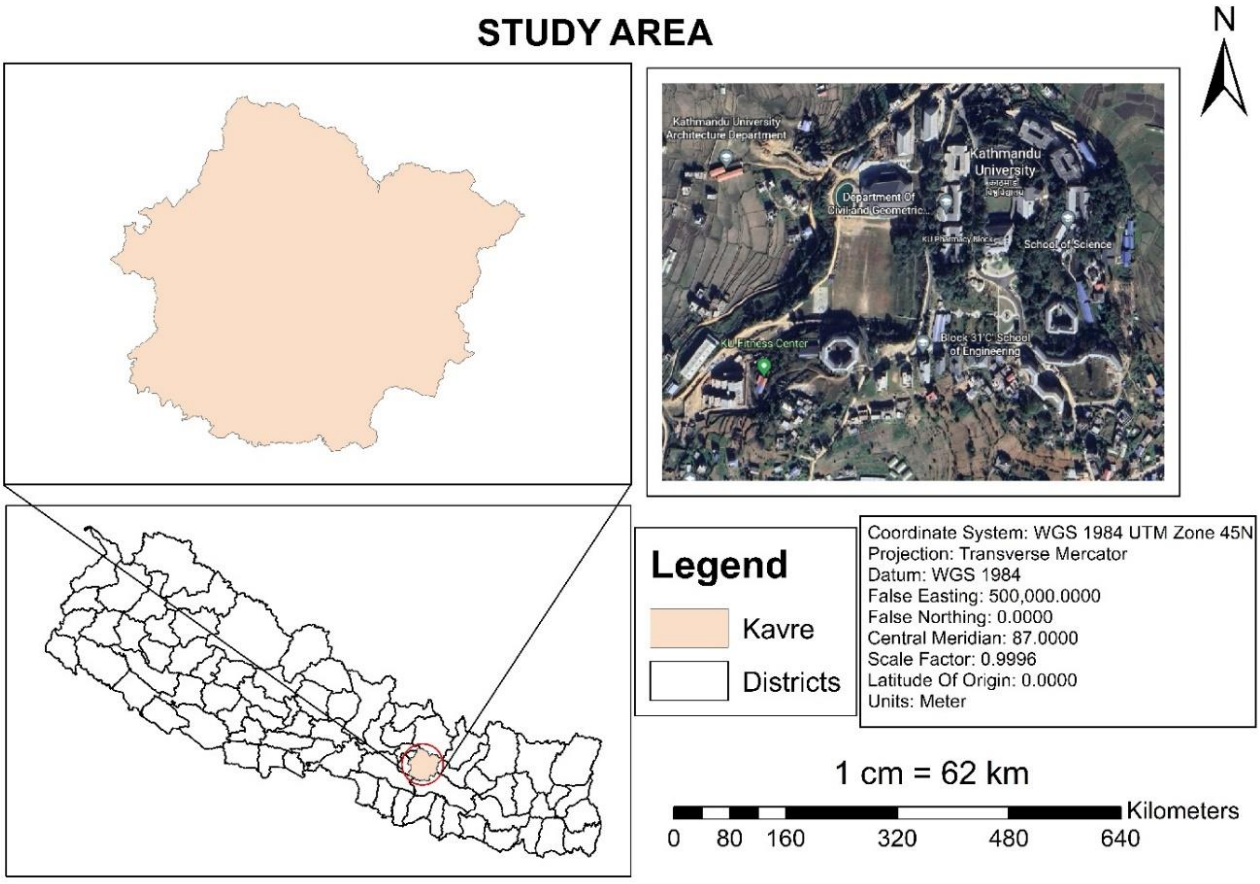

Figure 1. Location map of the study area.

3. Material and methods

This study mainly focuses on the primary data sources to achieve the motive of this study. The study is based upon primary data collected from field surveys using both ground survey using DGPS and UAV-based survey (Mavic air-2). UAV-based topographical mapping refers to the use of unmanned aerial vehicles (UAV) to capture aerial images of the topography. This data can be used to create maps and 3D models of the terrain, which can be useful for a variety of purposes, such as land management, planning, and engineering. The workflow is shown in Figure 2.

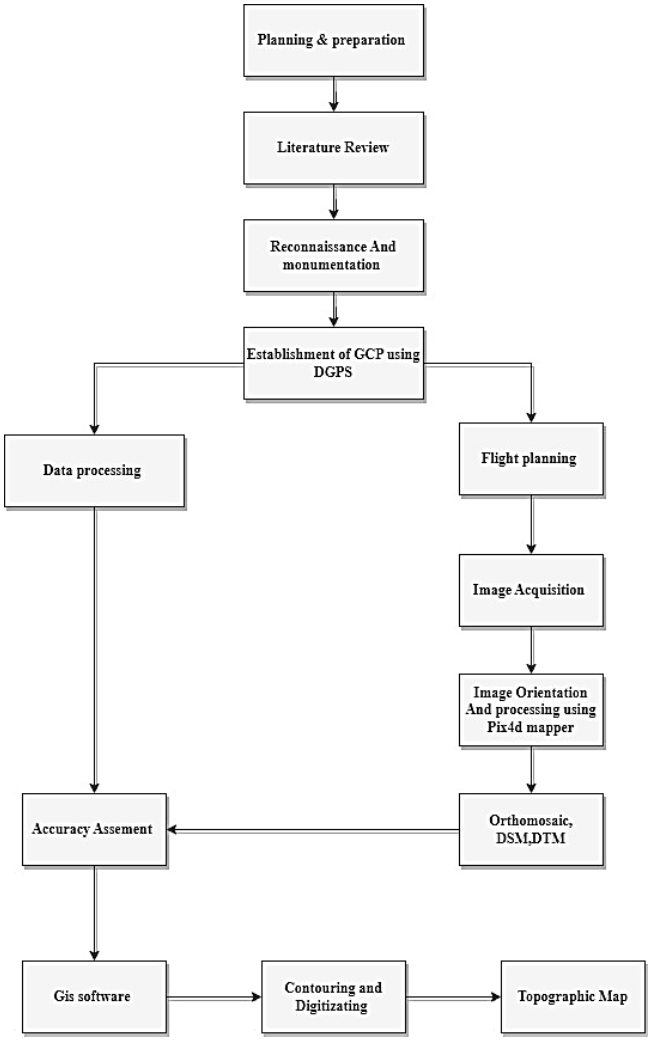

Figure 2. Study workflow.

An unmanned aerial vehicle was used to acquire aerial images of the study area. The Specification of the UAV is shown in Table 1.

3.1. Reconnaissance

Preparation of topographic mapping using UAV in this study includes preliminary surveys and preparation of instruments. The study area, software, and instrument selection, including the choice of digital camera and UAV platform types, are all part of this phase. This is the stage where the reconnaissance survey of the site was done by visiting the site. With the help of Google Earth images, the points for placing the control points were visualized. In the case of an Area with Undulating Terrain the most suitable arrangement of GCPs is one with GCP placed in a die shape (i.e. GCP at the central region and other GCPs well distributed along the boundary Furthermore, the GCPs should be arranged such that they cover all elevations [14]. A minimum number of 3 GCPs is required but 5 to 10 GCPs are usually enough, even for large projects More GCPs do not contribute significantly to increasing the accuracy [15]. The distribution of control points should be even and well-distributed to get better output with better accuracy throughout the project area. The Recommended Number of [16] Checkpoints Based on Area is shown in Annex 3. Keeping the above-mentioned criteria 12 wooden pegs were monumented throughout the study area to establish ground control points. Then these points were covered by a GCP marker board. These boards helped to identify the control points on the images taken by the drone.

Table 1. UAV specification.

Specification	Details
Brand	DJI
Type	Quadcopter
Camera Model Name(s)	L1D-20c_10.3_5472x3648 (RGB)
Remote	2.4GHz wireless remote control
Aperture	F2.8-F11
Shutter speed	8-1/8000s
Max. image size	5472*3648
Maximum takeoff altitude	6000m
Max flight time	31 minutes
Geolocation	Onboard GPS

3.2. Establishment and processing of GCP

The Ground Control Points and Checkpoints are established before the aerial photography. Based on the above-mentioned criteria Using the Differential Global Positioning System (DGPS), 12 ground control points (vertical and horizontal) of fourth order were established. The coordinates of these control points were determined by static DGPS survey using Stonex S8 Plus. The raw data (dat file) were transferred from the instrument to the computer. The dat file was converted to a Rinex file using static to Rinex converter. The Observation file was renamed as (1000. O) and was emailed to CSRS PPP, which is a Canadian website, to calculate the coordinates of the base station. A Trimble business center was used for post-processing the raw data files. During post-processing in TBC, the coordinate system was changed to UTM 45 N and the horizontal datum to WGS 1984. For distance measurement, the unit was changed to a meter and GPS time was from local to GPS. Baseline processing was used to calculate the distance and direction of the other control point reference to the base station whose coordinates were obtained from the Canadian Spatial Reference System Precise Point Positioning (CSRS-PPP) service.

3.3. Flight planning and image acquisition

Before imaging the study area, suitable flight plans that contain many variables, such as flight height, GSD,

and the total number of photos, are designed. Flight planning is conducted with the DJI Pilot App, a mobile phone application for drone flight planning. Within this application, the user must specify several parameters, such as the area of interest, photograph overlap percentage, and flight height or desired GSD. The digital aerial imagery is collected using a camera mounted in a UAV. The aerial photographs are acquired in such a way, resulting in a series of digital aerial photographs with a percentage of overlap.

3.4. Image processing

After the geotagged images were captured, they were processed to get the outputs like Orthophoto, contour lines, DTM, DSM, etc. The images were prepared before processing by removing unnecessary and tilted photographs through visual inspection. Then filtered images were added to Pix4d Software (trial version) for processing. The overlapped and geotagged images were processed utilizing image-matching algorithms like the SIFT algorithm [17,18]. The output of the initial processing is the tie points initially matched by this algorithm. These tie points are generated by matching the same feature within the overlapped images. The first part of this is that it finds thousands of contrasting features in each image, which are saved as key points. It then compares key-point patterns between images to identify and create automatic tie points (ATPs). Once the ATPs are identified, the software uses aerial triangulation to estimate the camera calibration parameters and to refine the image coordinates. Doing so improves the accuracy of the 3D model and products [15]. Image orientation was done using 7 ground control points (GCPs). Figure 3 shows the 12 points statically surveyed on the ground using a DGPS/GNSS receiver. These points were marked using a notable GCP marker during image acquisition. Out of the 12 points, seven were selected as GCP for the exterior orientation process, and 5 were considered Check Points for the accuracy assessment of orthophoto. It was ensured that each point got marked in at least six images to avoid distortion [19].

4. Results and Discussion

The processed coordinates that were obtained with mean root mean square (RMS) error of 0. 012 m. the coordinates of GCPs (Table 2), which were used to georeferenced the images, whereas Table 3 represents the coordinates of CPs used for the horizontal accuracy assessment of the orthophoto.

4.1. Orthophoto

After the point cloud and mesh generation DSM (Figure 4) is obtained and finally, the georeferenced orthophoto (Figure 5) of the study area has been generated based on orthorectification in pix4D. the orthophoto with 2.4 cm/pixel resolution was produced as shown in the quality of the orthophoto is outstanding as all the objects have been orthorectified, and the features can be detected very clearly. This orthophoto can be a reliable source for digitization, feature extraction, various map preparation, and other spatial planning activities. Digital Surface Model (DSM) can also be seen in Figure 4. The elevation of DSM ranges from 1461.23 m to 1538.55 m.

Table 2. GCP coordinates.

GCP	Easting (m)	Northing (m)	Elevation (m)
1000	355802.59	3055780.31	1516.122
1001	355909.6	3055684.34	1503.161
1002	355935.224	3055814.76	1487.662
1003	355811.562	3055894.42	1523.546
1005	355762.658	3056029.14	1500.202
1006	355598.916	3055878.11	1483.878
1007	355597.231	3055670.47	1497.402
1009	355396.553	3055643.22	1469.869

Table 3. Control points.

CP	Easting	Northing	Elevation
1004	355824.502	3055988.345	1500.606
1008	355689.318	3055801.706	1487.794
1010	355817.104	3055753.569	1513.776
1011	355772.97	3055780.097	1514.345
1012	355717.808	3055737.732	1491.353

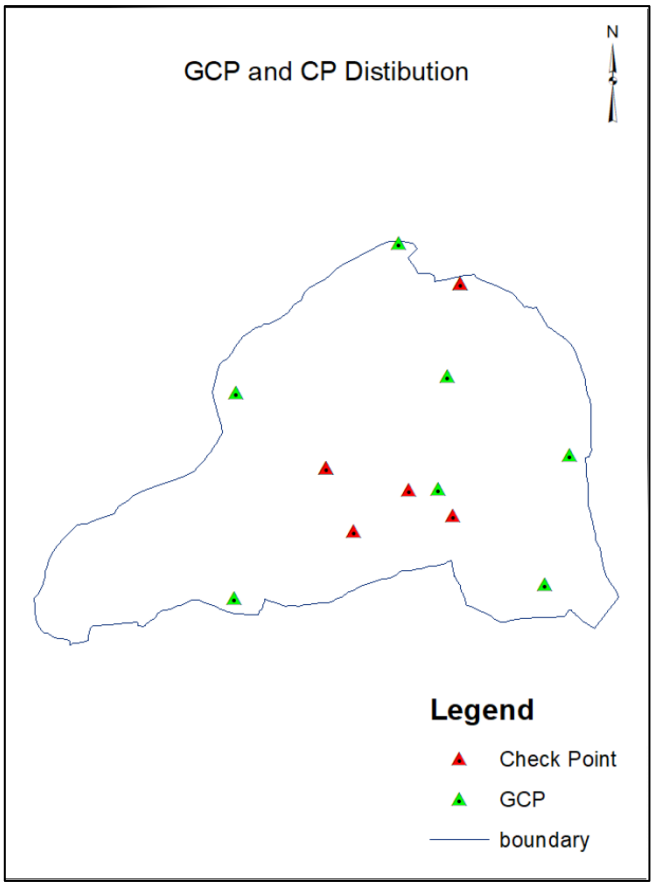

Figure 3. GCP and CP distribution.

4.2. Feature extraction and topo map creation

The final orthophoto and the DSM are very useful for manual or semi-automatic feature extraction for map creation and updating. The orthophoto was then used to extract features to produce a topographical map of study area (Figure 6). During feature extraction a geodatabase is created assigning different feature class and datasets for the features to be digitized. There after each feature

were digitized manually. While digitization topological rules were followed to minimize the topological errors such as silver polygons. Similarly, contours were used with 2m interval to show the shape of the Earth's surface. The high resolution and level of detail of the UAV orthophoto enables additional objects of interest to be visible. This provides the opportunity for creating new vector datasets representing topological features (such as drainage and narrow footpaths, electric poles), potentially enabling a more informed decision-making for planning activities. Finally, the topographical map of Kathmandu university at a scale of 1:1250 is produced. In total, 21921.44 m^2 of permanent school buildings, 90428.71 m^2 of Open area, 21295.24 m^2 of forest and 45169.84 m^2 of vegetation were digitized.

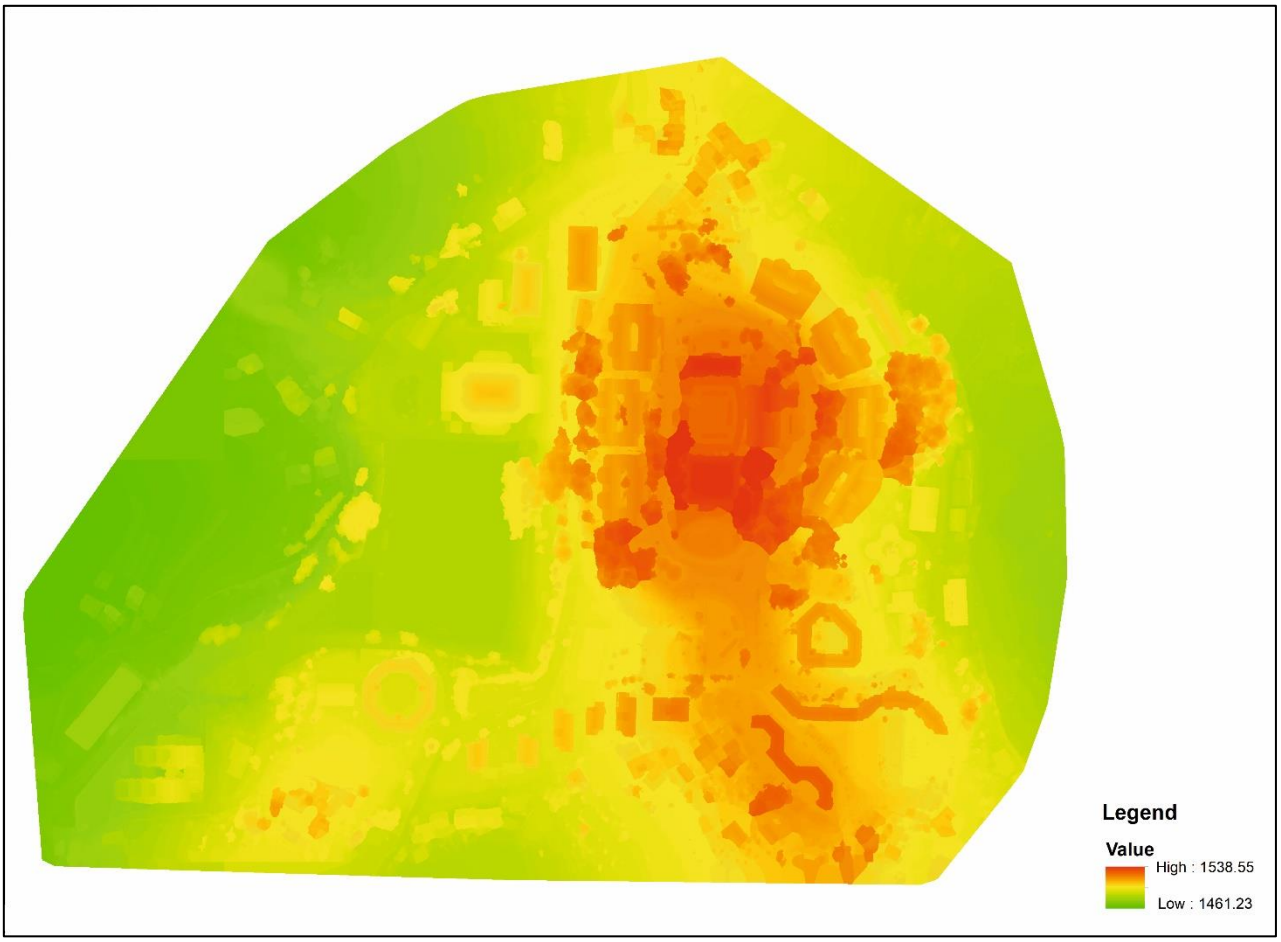

Figure 4. DSM.

4.2. Accuracy assessment of orthophoto

For qualitative assessment of orthophoto visual inspection was made which indicates that of the image was suitable for visual interpretation, as features are clearly visible and objects can be easily extracted. The quantitative assessment of the orthophoto consists of two aspects: (i) the planimetric accuracy assessment at the measured control points and (ii) the geometric accuracy of objects measured in the orthophoto. The RMSE of 5.37 cm in X and 4.94 cm in Y and 6.1 cm in Z as shown in Table 4. According to the horizontal accuracy standard mentioned in [20], the obtained error meets the requirements for the horizontal accuracy class of 7.5 cm (Table 5) [20].

5. Conclusion

This work demonstrates that UAVs provide promising opportunities to create a high-resolution and accurate orthophoto, thus facilitating map creation and updating. Through an example in Kathmandu University premises, this study has ensured that UAV is a reliable and portable technology to acquire data remotely and provide a result with a very high spatial and temporal resolution even in inaccessible terrain at a relatively low cost. The study showed that the UAV photogrammetry for large scale topographic mapping could replace other methods effectively such as GPS and Total station because the accuracies obtained were within the limits of specifications. In addition to that, the time required are reduced remarkably, more extensive coverage capability, less human interference, different types of output at the same time, and finally, the aerial images are permanent documents that can be referred to at any time in future. UAVs are currently more suitable for map updating projects over a limited study area and incremental map updating.

The article emphasizes the benefits of UAV technology, such as cost-effectiveness and speedy data acquisition. Nevertheless, it also faces constraints like restricted coverage, weather-related interruptions, cost factors, and the requirement for precise ground control points.

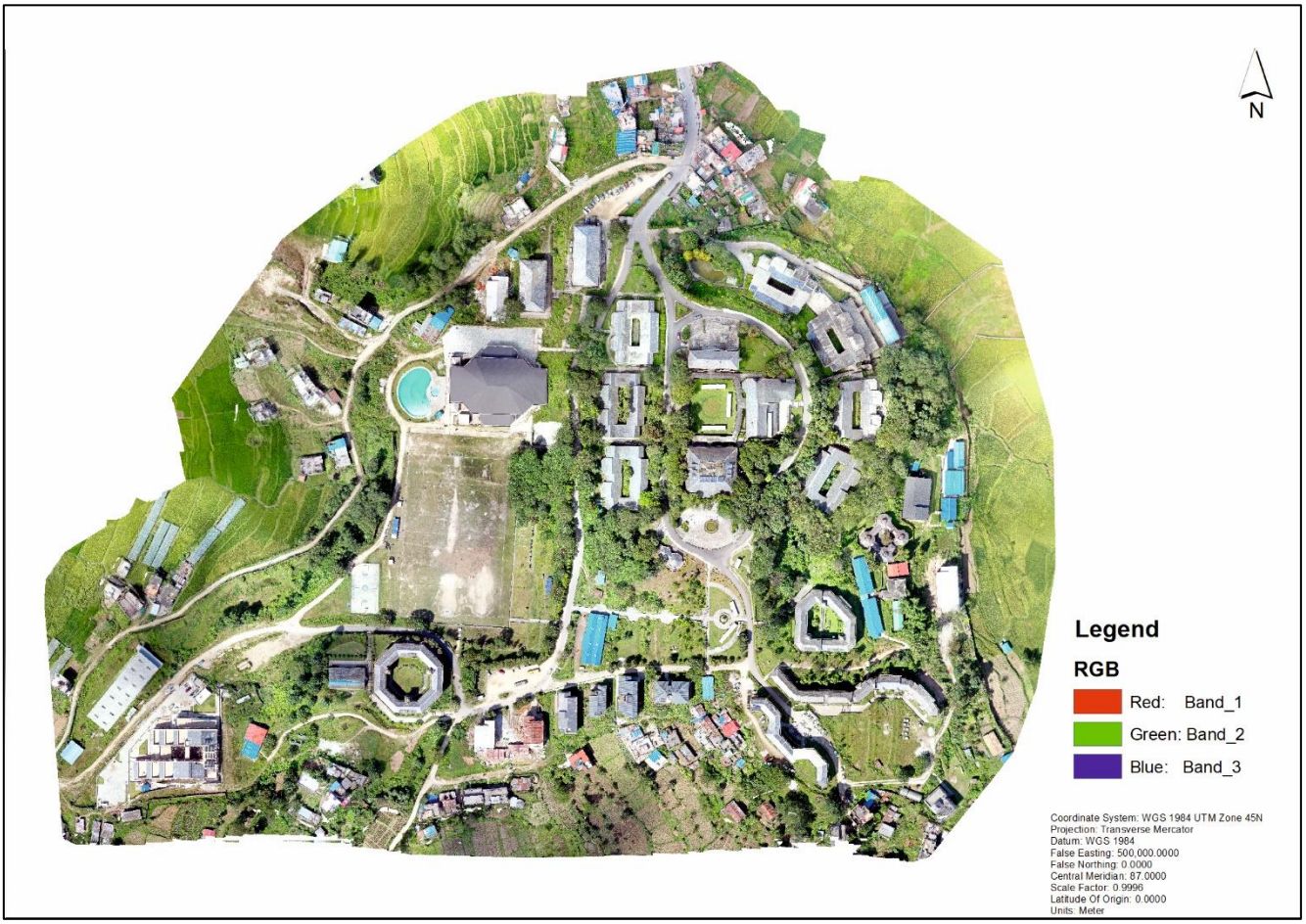

Figure 5. Orthophoto.

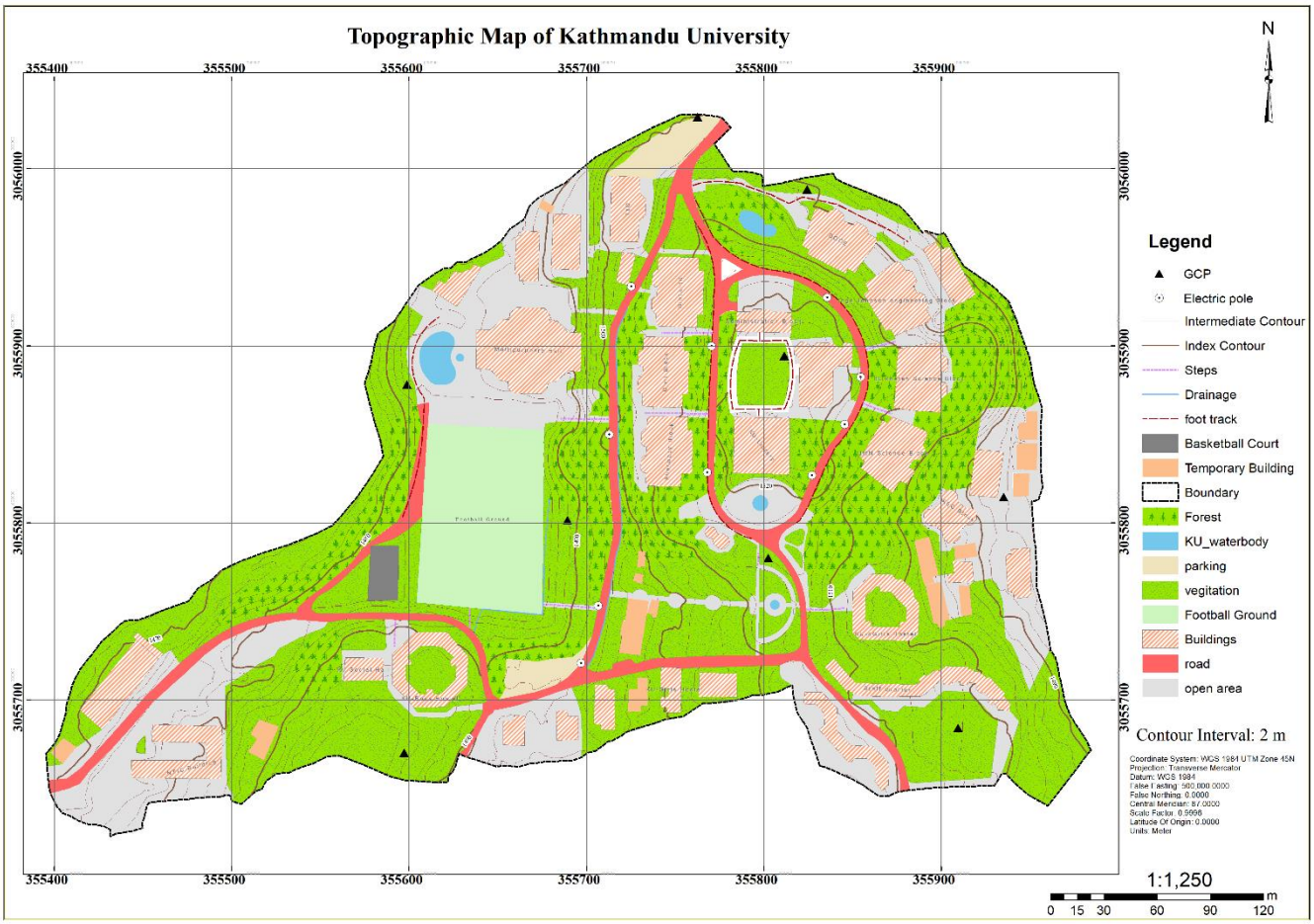

Figure 6. Topographic Map.

Table 4. Checkpoints error.

Station	Error in x	Error in y	Error in z
1004	-0.003	-0.064	0.04
1008	-0.004	-0.033	-0.12
1010	0.002	-0.013	-0.05
1011	-0.005	0.0059	-0.06
1012	0.12	0.012	-0.01
RMSE(CM)	5.373	4.94392	6.10508

Table 5. Length measured on ground and orthophoto.

Feature	L Field (m)	L Ortho (m)	Error	Relative Error
1	15.400	15.404	0.004	0.03%
2	29.120	29.157	0.037	0.13%
3	2.620	2.631	0.011	0.42%
4	2.450	2.458	0.008	0.33%
5	7.420	7.428	0.008	0.11%

Acknowledgment

Efforts were invested in the project with gratitude towards numerous individuals. Prof. Dr. Reshma Shrestha's opportunity, the Geomatics Engineering faculty's support, and Mr. Hareram Yadav's guidance were essential. Gratitude is extended to all who contributed to the project's success.

Author contributions

Sagar Pathak: Conceptualization, Methodology, Software, **Samrat Acharya and Ujjowl Thapa:** Data curation, Writing-Original draft preparation, Software, Validation, Visualization, **Gaurab Karn and Saugat Bk:** Investigation, Writing-Reviewing and Editing.

Conflicts of interest

The authors declare no conflicts of interest.

References

1. Tampubolon, W., & Reinhardt, W. (2014). UAV data processing for large scale topographical mapping. The International Archives of the Photogrammetry, Remote Sensing and Spatial Information Sciences, 40, 565-572. https://doi.org/10.5194/isprsarchives-XL-5-565-2014, 2014.
2. Fonstad, M. A., Dietrich, J. T., Courville, B. C., Jensen, J. L., & Carbonneau, P. E. (2013). Topographic structure from motion: a new development in photogrammetric measurement. Earth Surface Processes and Landforms, 38(4), 421-430. https://doi.org/10.1002/esp.3366
3. Quaye-Ballard, N. L., Asenso-Gyambibi, D., & Quaye-Ballard, J. (2020). Unmanned aerial vehicle for topographical mapping of inaccessible land areas in Ghana: A Cost-Effective Approach. FIG Working Week.
4. Ahmad, M. J., Ahmad, A., & Kanniah, K. D. (2018, June). Large scale topographic mapping based on unmanned aerial vehicle and aerial photogrammetric technique. In IOP Conference Series: Earth and Environmental Science, 169(1), 012077. https://doi.org/10.1088/1755-1315/169/1/012077
5. Singhal, G., Bansod, B., & Mathew, L. (2018). Unmanned aerial vehicle classification, applications and challenges: A review. PrePrints, 2018110601. https://doi.org/10.20944/preprints201811.0601.v1
6. Bi, H., Zheng, W., Ren, Z., Zeng, J., & Yu, J. (2017). Using an unmanned aerial vehicle for topography mapping of the fault zone based on structure from motion photogrammetry. International Journal of Remote Sensing, 38(8-10), 2495-2510. https://doi.org/10.1080/01431161.2016.1249308
7. Isaac-Medina, B. K., Poyser, M., Organisciak, D., Willcocks, C. G., Breckon, T. P., & Shum, H. P. (2021). Unmanned aerial vehicle visual detection and tracking using deep neural networks: A performance benchmark. In Proceedings of the IEEE/CVF International Conference on Computer Vision, 1223-1232.
8. Remondino, F., Barazzetti, L., Nex, F., Scaioni, M., & Sarazzi, D. (2012). UAV photogrammetry for mapping and 3d modeling–current status and future perspectives. The International Archives of the Photogrammetry, Remote Sensing and Spatial Information Sciences, 38, 25-31. https://doi.org/10.5194/isprsarchives-XXXVIII-1-C22-25-2011
9. Wolf, P. R., Dewitt, B. A., & Wilkinson, B. E. (2014). Elements of Photogrammetry with Applications in GIS. McGraw-Hill Education.
10. Mikhail, E. M., Bethel, J. S., & McGlone, J. C. (2001). Introduction to modern photogrammetry. John Wiley & Sons.
11. Cramer, M., Stallmann, D., & Haala, N. (2000). Direct georeferencing using GPS/inertial exterior orientations for photogrammetric applications. International Archives of Photogrammetry and Remote Sensing, 33(B3/1; PART 3), 198-205.
12. Syetiawan, A., Gularso, H., Kusnadi, G. I., & Pramudita, G. N. (2020). Precise topographic mapping using direct georeferencing in UAV. In IOP Conference Series: Earth and Environmental Science, 500(1), 012029. https://doi.org/10.1088/1755-1315/500/1/012029
13. Chi, Y. Y., Lee, Y. F., & Tsai, S. E. (2016). Study on high accuracy topographic mapping via UAV-based images. In IOP Conference Series: Earth and Environmental Science, 44(3), 032006. https://doi.org/10.1088/1755-1315/44/3/032006
14. Awasthi, B., Karki, S., Regmi, P., Dhami, D. S., Thapa, S., & Panday, U. S. (2020). Analyzing the effect of distribution pattern and number of GCPs on overall accuracy of UAV photogrammetric results. In Proceedings of UASG 2019: Unmanned Aerial System in Geomatics, 1, 339-354. https://doi.org/10.1007/978-3-030-37393-1_29
15. Pix4D S. A., (2017). User manual Pix4Dmapper 4.1, 305p.
16. ASPRS (2014). ASPRS positional accuracy standards for digital geospatial data. Photogrammetric Engineering & Remote Sensing, 81(3), A1-A26. https://doi.org/10.14358/PERS.81.3.A1-A26

17. Chudal, K. K., Lamsal, P., & Oli, P. P. (2020). Drone based urban planning in Nepal. FIG Working Week.
18. Barry, P., & Coakley, R. (2013). Accuracy of UAV photogrammetry compared with network RTK GPS. The International Archives of the Photogrammetry, Remote Sensing and Spatial Information Sciences, 2, 2731.
19. Udin, W. S., & Ahmad, A. (2014). Assessment of photogrammetric mapping accuracy based on variation flying altitude using unmanned aerial vehicle. In IOP conference series: Earth and Environmental Science, 18(1), 012027. https://doi.org/10.1088/1755-1315/18/1/012027
20. ASPRS (2013). ASPRS accuracy standards for digital geospatial data. Photogrammetric Engineering & Remote Sensing, 1073-1085

Mersin Photogrammetry Journal
https://dergipark.org.tr/en/pub/mephoj
e-ISSN 2687-654X

Assessing the contribution of RGB VIs in improving building extraction from RGB-UAV images

Richmond Akwasi Nsiah [*1], **Saviour Mantey** [1], **Yao Yevenyo Ziggah** [1]

[1] *University of Mines and Technology, Department of Geomatics Engineering, Tarkwa, Ghana, ransiah94@gmail.com, smantey@umat.edu.gh, yyziggah@umat.edu.gh*

Cite this study: Nsiah, R. A., Mantey, S., & Ziggah, Y. Y. (2024). Assessing the contribution of RGB VIs in improving building extraction from RGB-UAV images. Mersin Photogrammetry Journal, 6 (1), 9-21

https://doi.org/10.53093/mephoj.1399083

Keywords
Building extraction
UAV
GeoBIA
RGB vegetative indices
Random forest

Research Article

Received:01.12.2023
Revised: 13.01.2024
Accepted: 22.01.2024
Published:16.03.2024

Abstract

Buildings are a fundamental component of the built environment, and accurate information regarding their size, location, and distribution is vital for various purposes. The ever-increasing capabilities of unmanned aerial vehicles (UAVs) have sparked an interest in exploring various techniques to delineate buildings from the very high-resolution images obtained from UAV photogrammetry. However, the limited spectral information in UAV images, particularly the number of bands, can hinder the differentiation between various materials and objects. This setback can affect the ability to distinguish between different materials and objects. To address this limitation, vegetative ındices (VIs) have been employed to enhance the spectral strength of UAV orthophotos, thereby improving building classification. The objective of this study is to evaluate the contribution of four specific VIs: the green leaf index (GLI), red-green-blue vegetation index (RGBVI), visual atmospherically resistant index (VARI), and triangular greenness index (TGI). The significance of this contribution lies in assessing the potential of each VI to enhance building classification. The approach utilized the geographic object-based image analysis (GeoBIA) approach and a random forest classifier. To achieve this aim, five datasets were created, with each dataset comprising the RGB-UAV image and a corresponding RGB VI. The experimental results on the test dataset and a post-classification assessment indicated a general improvement in the classification when the VIs were added to the RGB orthophoto.

1. Introduction

Among the myriad of urban features, buildings represent a fundamental component [1]. As such, obtaining accurate and detailed information on buildings is crucial for urban planning, infrastructure development, disaster management, and other applications [2]. In remote sensing, the term 'building extraction' is used to describe the process of delineating building footprints or roof outlines from remotely sensed data, such as very high-resolution (VHR) aerial and satellite images. These datasets are the most widely used as they offer rich spatial details. Furthermore, the enhanced spatial resolution of these datasets improves the ability to distinguish various objects in urban settings, thereby facilitating the extraction of individual building information [3].

The recent advancements in unmanned aerial vehicle (UAV) technologies, coupled with the sophistication of imaging sensor systems, have resulted in an increased use of these systems to capture aerial images of areas of interest. The VHR images obtained can be quickly processed to obtain orthophotos, thus providing an alternative dataset to extract building outlines [4]. This development has sparked an interest in exploring various methods to delineate building objects from VHR UAV imagery.

Conventional methods for building extraction involve manual approaches, which include delineating the outlines of buildings using various computer-aid designs (CAD). Also, rule-based techniques that leverage knowledge of buildings have been employed in building extraction. While the manual approach shows promise, it is repetitive and time-consuming when applied to larger areas [5-6]. In contrast, rule-based techniques rely on straight lines and use low-level edge detection and perceptual grouping to extract building outlines [7-8]. However, these line-based approaches encounter limitations with certain building geometries and struggle with low signal-to-noise ratio (SNR) in VHR images [9–10]. Some methods employ template matching, which involves the use of manually generated templates and similarity measures for building extraction [11–14]. Despite their flexibility and accuracy, template-based approaches require extensive prior knowledge of the geometrical shape parameters for the design and

generation of the templates. Moreover, the need to develop different templates for different applications increases the computational costs and reduces the ability to process extensive data [9, 11].

Other studies utilise knowledge of building geometries, such as box-shape, T-shape, L-shape, or E-shape, and the spatial or contextual relationship between buildings and the background, such as shadows, are used to delineate buildings [15–19]. The drawback of these approaches is their reliance on building knowledge, and the task of transferring implicit knowledge into explicit detection rules is challenging. If the rules are too strict, buildings may be missed, whereas overly loose rules can lead to many false detections [9–11]. Furthermore, several factors can make the extraction of buildings using rule-based techniques a challenging task. These factors include such as the intricate shape and size of buildings, occlusion, and imaging angles.

Contrastingly, image classification approaches (pixel-based and object-based) categorize pixels in images into specific classes, primarily buildings, and non-buildings in the building extraction domain [20]. Pixel-based classification operates by examining pixels in isolation and leverages the spectral characteristics of each pixel to assign them to distinct classes. While this approach is relatively simple, it encounters difficulties with spatial variability when applied to VHR images. On the other hand, the object-based approach groups image pixels into spectrally homogenous segments using various image-segmentation algorithms. Subsequently, an algorithm is adopted to classify the segments into predefined categories. This transition from focusing on individual pixels to evaluating at the segment level introduces complexity into the classification process. As a result, this approach can capture spatial relationships and complex patterns in VHR images [21–22]. The object-based approach, alternatively referred to as geographic object-based image analysis (GeoBIA), has emerged as an efficient approach for automating the extraction of objects from remote sensing data [23]. GeoBIA integrates image segmentation algorithms to segment VHR images into image objects, extract and employs machine learning algorithms such as support vector machine (SVM), random forest (RF), and decision trees (DT), among others, to classify the image objects, based on their spatial information, and spectral characteristics. This process makes GeoBIA particularly suited for building extraction [24 – 25].

Several researchers have since explored the use of GeoBIA for extracting buildings from VHR images. Aminipouri et al. [24] conducted a study that leveraged VHR satellite imagery to extract spatial information about slum settlements using object-oriented techniques. The study aimed to determine the feasibility of using VHR orthophotos to create an accurate inventory of buildings for estimating the slum population. The researchers used eCognition software for image segmentation and classification of building roofs in three different slum areas in Dar-Es-Salaam. The proposed model achieved a roof extraction accuracy of 91%. The estimated population represented 82.2%, 72.5%, and 68.3% for the wards of Charambe, Manzese, and Tandale, respectively. In another study, Benarchid et al. [26] presented an automatic building extraction approach in Tetuan City. This method employed an object-based classification and shadow information derived from VRH multispectral images. The shadow information was extracted using invariant color features. The quality assessment was performed at two different levels: area and object. The area level evaluated the building delineation performance, whereas the object level assessed the accuracy in the spatial location of individual buildings. The results showed an overall building detection percentage of 87.60% when the parameters were properly adjusted and adapted to the type of areas considered.

The methodology adopted by Chen et al. [9] presented an object-based and machine learning-based approach for automatic house detection from RGB high-resolution images. The study utilised thresholding, watershed transformation, and hierarchical merging for image segmentation. In addition, the study proposed two new features, namely edge regularity indices (ERI) and shadow line indices (SLI), to capture the characteristics of house regions effectively. The researchers employed three classifiers, namely AdaBoost, random forests, and support vector machine (SVM), to identify houses from test images. The proposed ERI and SLI features improved the precision and recall by 5.6% and 11.2%, respectively. Norman et al. [22] focused on urban building detection using object-based image analysis (OBIA) and machine learning (ML) algorithms. The study employed a medium-resolution Sentinel-2B image and applied SVM and DT algorithms for the classification of buildings. The study underscored the significance of segmentation parameters and feature selection, with SVM outperforming DT and achieving an accuracy of 93%.

Frishila and Kamal [27] aimed to examine the effectiveness of spectral features in identifying and mapping building objects and assess the accuracy of the mapping result. The location of the study sample was in parts of Padang City, West Sumatra, and the image used was a pan-sharpened GeoEye-1 image (0.5 m pixel size). Image segmentation was done by the multi-resolution segmentation method to delineate candidate segments for building objects. Each segment was then assigned to building and non-building classes by applying a rule-based classification algorithm. Several spectral features were incorporated in discriminating the objects, including several band ratios that involve all bands in GeoEye-1 (Blue, Green, Red, and near-IR), iron oxide indices, mean value of red and NIR bands, border contrast of red and NIR bands, HIS, and Quantile of the bands. The map result indicates that building and non-building objects could be separated using spectral features of the GeoEye-1 image. However, there are some classification inaccuracies, mainly for the densely populated urban areas where buildings objects are close to each other. An area-based accuracy assessment indicated that the use of spectral features provides an overall accuracy of 68.7%.

Hossain and Chen [28] introduced several modifications to previously proposed hybrid segmentation methods for building extraction. They used the reference polygon to identify optimal parameters, a donut-filling technique to reduce over-segmentation

caused by roof elements, and illumination differences to restrict merging with shadow. Their methodology was tested on a UAV image with visible bands only and achieved better results compared to other methods. One of the strengths of their method was that there was no parameter tuning and user interaction at running time. In addition, it was able to segment both small and large buildings without using any scale or object size parameters.

Dornaika et al. [29] presented a generic framework that exploits recent advances in image segmentation and region descriptor extraction for the automatic and accurate detection of buildings on aerial orthophotos. The proposed solution is supervised in the sense that the appearances of buildings are learnt from examples. For the first time in the context of building detection, they used the matrix covariance descriptor, which proved to be very informative and compact. They introduced a principled evaluation that allows selecting the best pair segmentation algorithm-region descriptor for the task of building detection. The proposed approach presents several advantages in terms of scalability, suitability, and simplicity with respect to the existing methods. Furthermore, the proposed scheme (detection chain and evaluation) can be deployed for detecting multiple object categories that are present in images and can be used by intelligent systems requiring scene perception and parsing, such as intelligent unmanned aerial vehicle navigation and automatic 3D city modeling.

Argyridis and Argialas [30] developed a GEOBIA approach that integrates Deep Learning classification and Fuzzy Ontologies to monitor building changes in suburban areas of Greece. They employed deep belief networks (BDNN) on the lowest level of the segmentation hierarchy for the initial detection of areas of possible change. The classification result was then refined based on interpretation rules developed on the upper levels of the hierarchy. Their accuracy assessment indicated that 93.5% of the total number of changes were successfully detected, while the commission error was less than 20%.

While GeoBIA has shown considerable promise in building classification and segmentation, the spectral limitations of UAV-RGB imagery pose a challenge, especially when distinguishing between buildings and other urban features (3). Researchers have since used various ancillary datasets to address this drawback when VHR multispectral images are adopted for building extraction, the near-infrared (NIR) information has been established to be highly effective in differentiating vegetation from buildings [4]. Most often, various spectral indices such as the normalised difference vegetation index (NDVI), normalised difference built-up index (NDBI), and the normalised difference water index (NDWI), among others, are utilised to enhance building-background separability, thereby improving building extraction [31-33].

To address this challenge, many researchers have resorted to ancillary datasets, such as the RGB vegetative indices (VIs), to distinguish buildings from vegetative features [1, 4]. VIs can capture subtle spectral variations, and they present a promising approach for enhancing building classification and segmentation when integrated with the spatial context analysis of GeoBIA [1, 34].

While some research works have concentrated on improving building classification using RGB VIs, a comprehensive comparison evaluating the impact of each VI on classification accuracy has yet to be conducted. This study aims to bridge this gap. Consequently, the primary objective of this study is to investigate the impacts of incorporating RGB-based VIs into the GeoBIA classification pipeline for building extraction. To achieve this objective, four well-established VIs were utilized. These include the green leaf index (GLI), red-green-blue vegetation index (RGBVI), visual atmospherically resistant index (VARI), and triangular greenness index (TGI) were employed. These VIs were combined with UAV-RGB imagery to form separate datasets for the building classification task. The efficacy of each dataset was evaluated using key performance metrics, including overall accuracy (OA), precision (P), recall (R), and F-1 score.

2. Material and method

This study utilized the Google Earth Engine (GEE) Platform to perform the building extraction. GEE is a planetary-scale platform designed for Earth science and data analysis. The platform offers a web-based code editor equipped with a Javascript API for executing scripts. Consequently, it enables the use of cloud computing to quickly develop and perform complex geospatial workflows with ease.

The orthophoto of the study area had to be uploaded to the platform so as to perform the building extraction using the GeoBIA approach. The dataset was subsequently imported into the code editor, followed by the performance of the analysis. The workflow involved generating RGB VIs using the individual bands of the orthophoto, creating the datasets of each VI from the bands of the original orthophoto, adding each VI and the RGB image, performing an object-based segmentation on each dataset, selecting features for building and non-building classes, and training and testing a machine-learning classifier on the selected features.

The Randon Forest (RF) machine-learning classifier was adopted for this study, whereas the simple linear iterative clustering (SLIC) algorithm was exploited for the segmentation step. Figure 1 depicts the workflow adopted for this study.

2.1. Study area and dataset

The New Mankessim community is within the administrative jurisdiction of the Tarkwa Nsuaem Municipal Assembly, located approximately 19.30 kilometres southwest of the municipal capital, Tarkwa, in the Western Region of Ghana. From a geographical perspective, the community is positioned at latitude 5°5’ 29.45” N and longitude 2°6’ 4.70” W, nestled at an average altitude of 55 meters above mean sea level. In response to the evolving mining dynamics, a prominent mining company operating in the region initiated a resettlement program to relocate the community members from their previous dwellings to the current

location. Consequently, a well-planned layout is a notable feature of the New Mankessim community. In addition, a consistent architectural style marks this layout and reflects a cohesive and deliberate approach to urban development.

Aerial images of the area were acquired using a Phantom 4 UAV. These images were processed using Agisoft Metashape Pro photogrammetric software to obtain a georectified image of the community. Figure 2 depicts the georectified image of the study area.

2.2. Geographic object-based image analysis (GeoBIA)

GEOBIA is an image analysis approach that is commonly applied to VHR remote sensing data. It serves various purposes, such as land-cover mapping and identifying specific geographic objects like buildings, cars, and trees [35-36]. The workflow of the GeoBIA approach includes image segmentation, feature extraction, image classification, and accuracy assessment. These steps were all implemented using the Google Earth Engine platform.

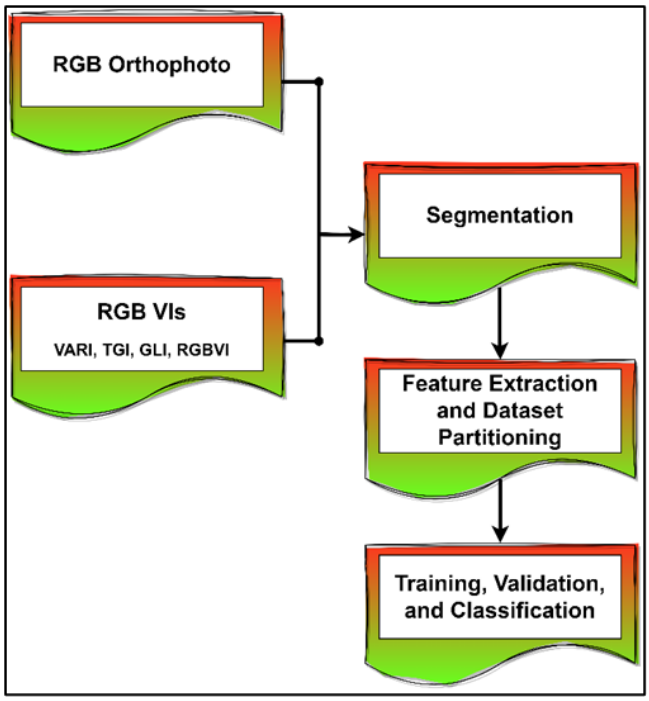

Figure 1. Methodological workflow.

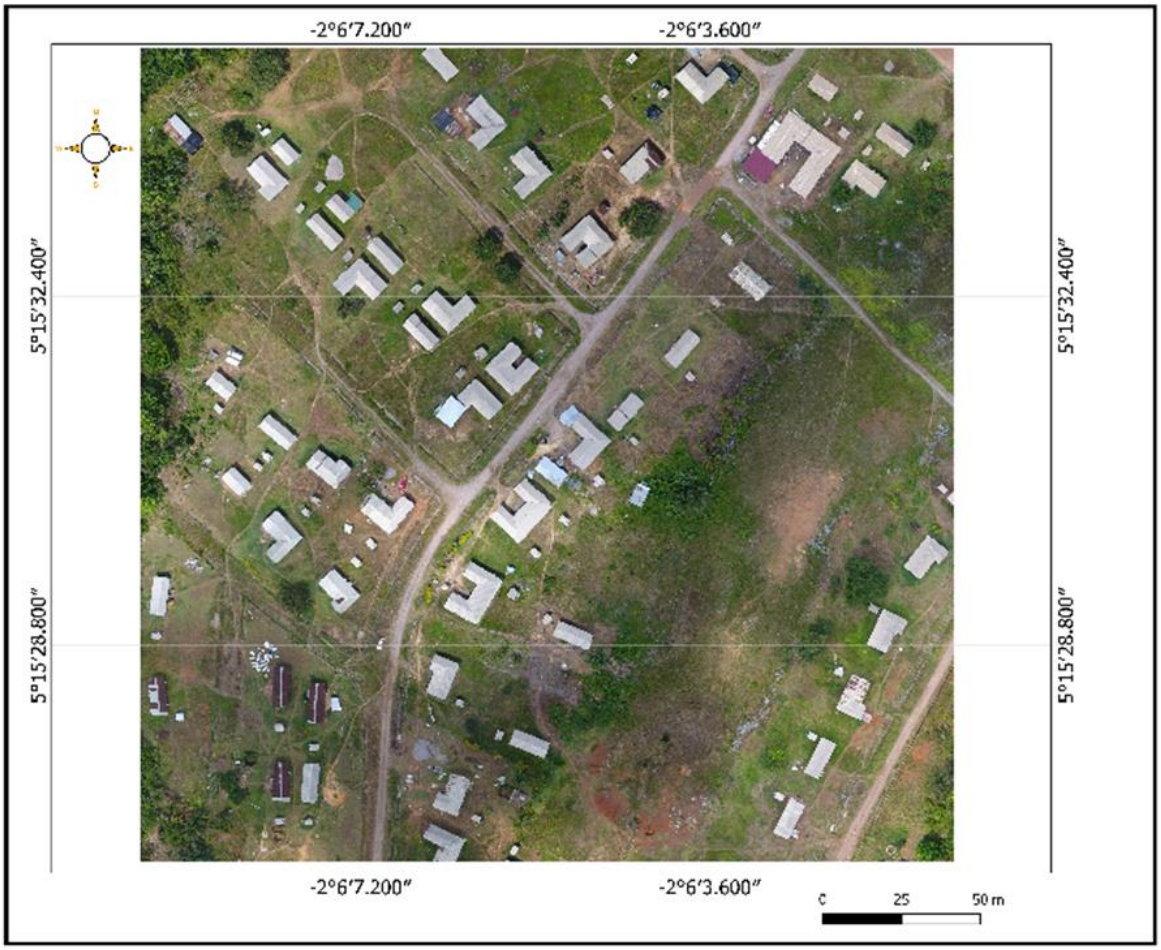

Figure 2. UAV image of New Mankessim.

2.2.1 Image segmentation

This is the first step of geographic object-based image analysis, and it involves segmenting images into homogenous objects [23]. Image objects are groups of neighbouring pixels representing objects within the orthophoto with similar spectral and spatial attributes. There are various methods for performing image

segmentation; however, the simple linear iterative clustering (SLIC) algorithm proposed by Achanta et al. [37] was utilized. SLIC is a seed-based clustering technique that uses a modified k-means clustering strategy to create highly efficient superpixels. Unlike prior methodologies, SLIC excels in preserving boundaries while offering improved speed and memory efficiency.

It also enhances segmentation performance and can be extended for super voxel generation. This method carefully incorporates considerations of both color homogeneity and shape uniformity, achieving a well-balanced trade-off between these aspects [38]. To obtain optimum and homogenous image objects using SLIC, several parameters, such as compactness, seed size, and grid type, need to be defined.

However, due to the vast search space of the parameters, choosing the optimum combination of parameters is challenging. If the parameter combination is not carefully chosen, it can result in under-segmentation or over-segmentation. Thus, there is a high chance of low performance when the wrong parameter combination is used [25]. For this work, the parameters were determined using a trial-and-error approach, adopted according to the approach in [39, 40].

2.2.2 Feature extraction and selection

This step involves capturing substantial information from the image segments' objects to characterize features within an image. Commonly extracted features include spectral information, texture, shape, size, and contextual relationships. The most relevant features are subsequently selected to contribute to and optimize the computational efficiency of the subsequent classification process [3].

The spectral attributes, primarily the mean values of the red, green, and blue (RGB) bands, were extracted for this study. In addition, the mean of the spectral indices, that is, the green leaf index (GLI), red-green-blue vegetation index (RGBVI), visual atmospherically resistant index (VARI), and triangular greenness index (TGI), were extracted. These mean spectral values were chosen as the primary features for building extraction and further characterization because they capture colour information for distinguishing building objects from other urban features.

A total of 916 samples, 456 representing buildings and the remaining non-building objects, were selected to train the machine learning classifier. The samples were randomly divided into training (80%) and validation or test (20%) sets to facilitate model training and evaluation. This partitioning ensures that the machine learning classifier is robust and reliable, permitting effective learning. Moreover, it enables assessing the model's performance in distinguishing between building and non-building classes.

2.2.3 Classification

The step involves using a machine learning classifier to classify the segments into respective classes. For this research, the random forest (RF) classifier that Breiman [41] proposed was employed to classify the selected features as either buildings or non-buildings. RF is an ensemble machine learning algorithm that combines multiple decision trees to make predictions. Each tree in the forest is trained on a different subset of the data with bootstrapping and random feature selection. The final prediction is determined by a majority vote or averaging of individual tree predictions, making it robust, accurate, and less prone to overfitting, making it robust and effective in handling complex classification tasks [42, 43].

For this research, the RF classifier was trained using the 769 training samples, with the mean values of each dataset serving as input features. Like the SLIC algorithm, RF also has several parameters that must be fine-tuned for optimum classification. These include the number of trees, variablesPerSplit, minLeafPopulation, bagFraction, and maxNodes seed. Choosing a prejudiced parameter can result in overfitting or underfitting. Other than the number of trees set to fifty (50), default values were maintained for all the other parameters.

Subsequently, the performance of the trained RF model was assessed using the test data. This was to ascertain how the RF model fared on unseen datasets, prior to classifying the entire dataset.

The final step was to assess the binary raster produced by each dataset. As such, the classified datasets were exported, and an evaluation was performed using ArcMap. The create accuracy assessment points and update accuracy assessment points functions in the spatial analyst toolbox were adopted for this approach. Using the create accuracy assessment points function, the equalized stratified random sampling technique was used to generate 1500 data points each for the building and non-building classes. The ground truth mask, generated from the digitized building polygons, was used as the target field for this operation.

Subsequently, the update accuracy assessment points function was utilized to generate reference points for each classified dataset. These reference points were used to assess the validity of the classified images with regard to the ground truth mask.

2.3 Evaluation metrics

A comprehensive validation approach was adopted to assess the accuracy of the building classification. The trained RF classifier was applied to the validation data to classify buildings and non-buildings. The results were then compared with ground truth data to evaluate classification performance. This evaluation was based on four metrics: overall accuracy, precision, recall, and F1-score, all of which were computed using a confusion matrix.

Recall is a metric that quantifies the proportion of building image objects that were successfully classified as buildings. It measures how effectively the proposed methodology captures all existing buildings within the validation dataset. Conversely, precision offers insights into the correctness of the approach by elucidating the probability that a detected structure is indeed a building [33].

F1-score is a metric that considers precision and recall, thereby providing a balanced assessment of the

approach's performance. It is an essential metric when there is an imbalance between positive and negative instances in the dataset.

Overall accuracy is a metric that measures the ratio of correctly classified building instances to the total number of building instances in the dataset. Equations (1) to (4) give the mathematical formulations for the evaluation metrics.

$$\text{Recall} \quad R = \frac{TP}{TP + FN} \tag{1}$$

$$\text{Precision} \quad P = \frac{TP}{TP + FP} \tag{2}$$

$$\text{Overall Accuracy} \quad OA = \frac{TP + TN}{TP + FP + TN + FN} \tag{3}$$

$$F_1\text{-score} \quad F_1 = \frac{2 * Precision * Recall}{Precision + Recall} \tag{4}$$

In Equations (1-4), TP represents correctly identified building segments, TN indicates correctly identified non-building segments, FP represents non-building segments erroneously classified as buildings, and FN denotes building segments incorrectly classified as non-building.

2.4 RGB-vegetative indices

Most consumer-grade UAVs are equipped with RGB cameras. RGB vegetation indices (VIs) are derived through mathematical equations applied to two or more spectral bands to emphasize specific aspects of vegetation greenness, thereby facilitating the identification of distinctive vegetation features within the imagery. This is possible as the digital number values of each band can be used to compute the pixel value in the RGB image. Several RGB VIs have since been created and developed [34, 44]. The RGB VIs utilized in this research are depicted in Figure 3, and their respective equations are in Table 1.

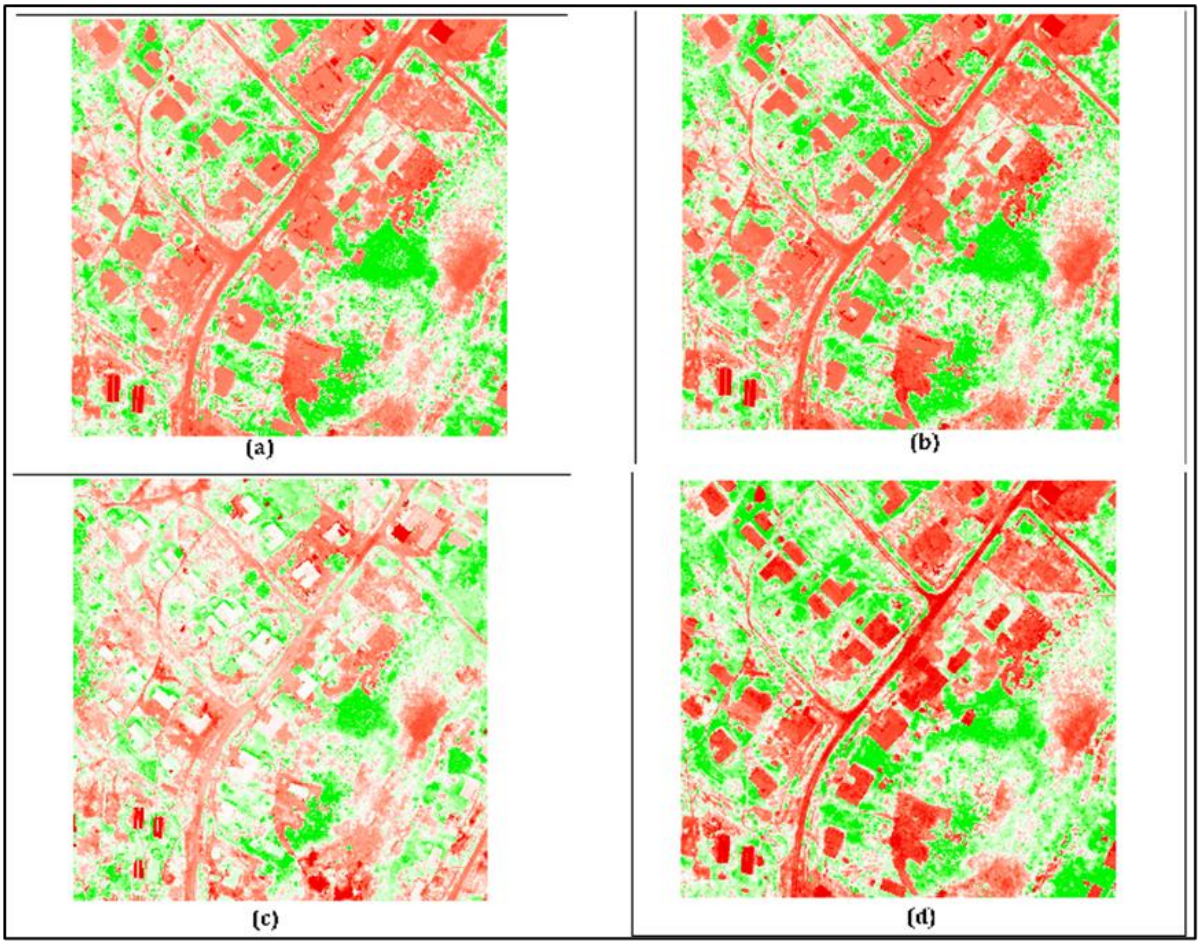

Figure 3. RGB VIs (a)GLI, (b)RGBVI, (c)VARI, and (d)TGI.

Table 1. RGB-VIs Utilized.

VI	Formula	Reference
Green Leaf Index	$GLI = \frac{(2 \times Green) - Red - Blue}{(2 \times Green) + Red + Blue}$	[45]
Red-Green-Blue Vegetation Index	$RGBVI = \frac{Green^2 - Blue \times Red}{Green^2 + Blue \times Red}$	[46]
Visual Atmospherically Resistant Index	$VARI = \frac{Green - Red - Blue}{Green + Red + Blue}$	[47]
Triangular Greenness Index	$TGI = Green - (0.39 \times Red) + (0.61 \times Blue)$	[48]

3. Results

This study generated five distinct datasets by combining the RGB VIs with the UAV-RGB image. These composite datasets included RGB with GLI, RGB with RGBVI, RGB with VARI, RGB with TGI, and RGB with all indices. Subsequently, each combination was used to train and validate the Random Forest (RF) classifier using selected spectral information.

The evaluation results obtained for each combination are detailed in Table 2. These results were derived from the 147 test datasets using the evaluation metrics, and these findings provide insight into how the random forest model performed on the test datasets. A visual representation of Table 2 is presented in Figure 4. The confusion matrix from the validation process using the test data is illustrated in Figure 5.

The quantitative assessment derived from the classification result for each dataset is outlined in Table 3. These findings give insight into how each classified output corresponds with the ground truth. Figure 6 is a bar chart providing a visual representation of Table 3. The confusion matrix for the post-classification assessment is depicted in Figure 7, and Figure 8 presents the classification results obtained by each dataset.

Table 2. RF performance on test dataset for various combinations.

Dataset	Metric			
	OA	P	R	F1
UAV-RGB only	0.9565	0.9643	0.9529	0.9586
RGB + GLI	0.9632	0.9897	0.9411	0.9648
RGB +RGBVI	0.9660	0.9671	0.9671	0.9671
RGB + VARI	0.9799	0.9806	0.9806	0.9806
RGB + TGI	0.9714	0.9880	0.9535	0.9704
RGB + All Indices	0.9507	0.9570	0.9368	0.9468

Table 3. Classification performance of various datasets.

Dataset	Metric			
	OA	P	R	F1
UAV-RGB only	0.9553	0.9401	0.9727	0.9561
RGB + GLI	0.9673	0.9655	0.9693	0.9674
RGB +RGBVI	0.9647	0.9491	0.9820	0.9653
RGB + VARI	0.9603	0.9429	0.9800	0.9611
RGB + TGI	0.9657	0.9580	0.9740	0.9660
RGB + All Indices	0.9660	0.9575	0.9753	0.9663

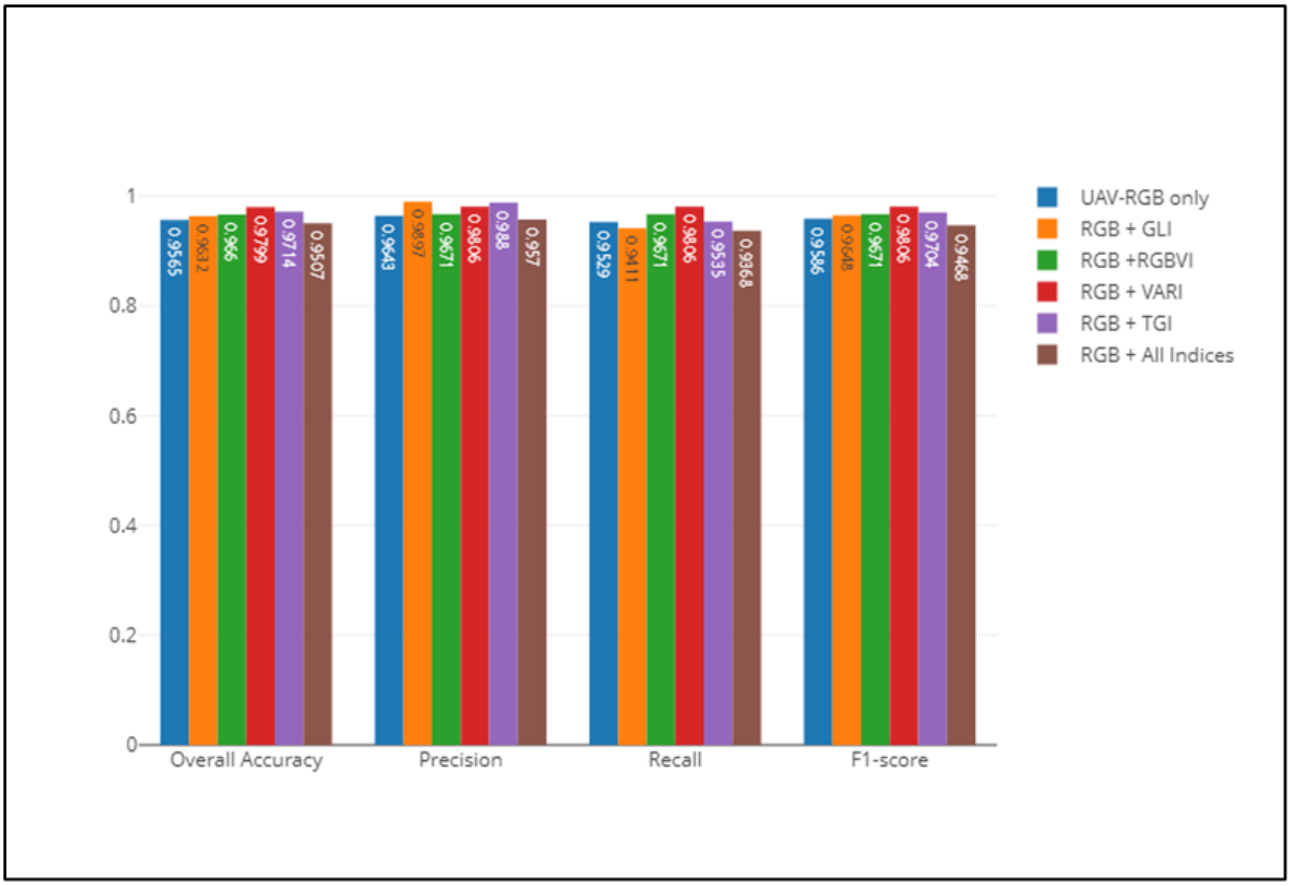

Figure 4. Plot of RF validation result.

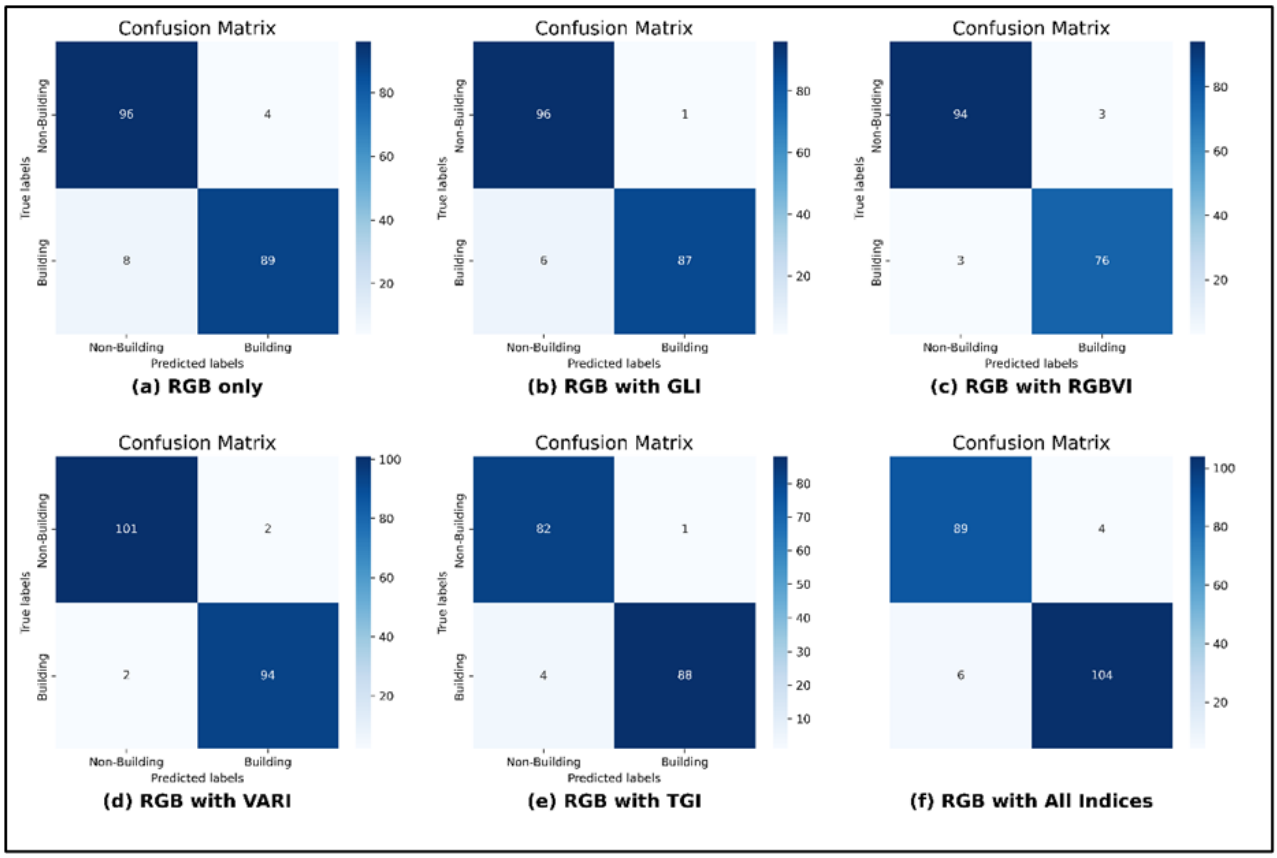

Figure 5. Confusion matrix for test data validation.

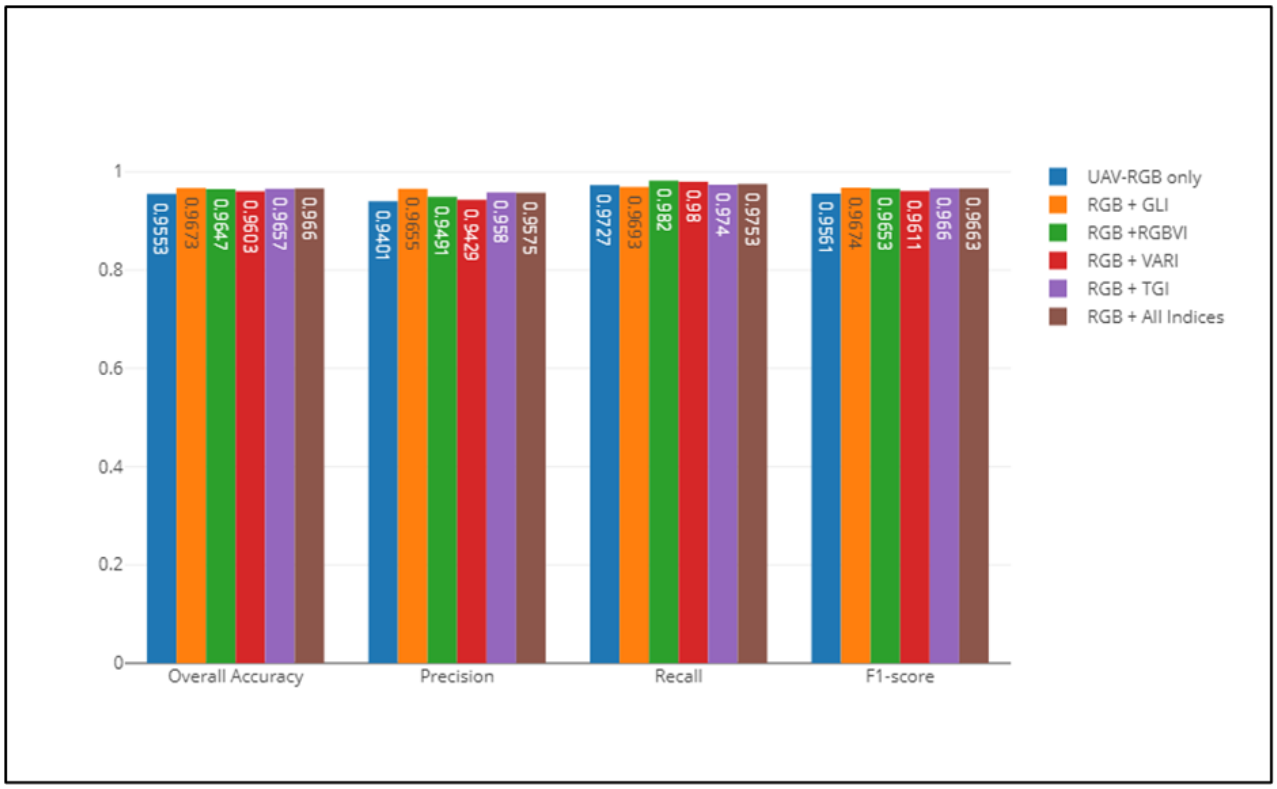

Figure 6. Bar plot of classification validation.

4. Discussion

From Table 2, which is the validation result based on the test data, it is observed that the combination of RGB and VARI achieved the highest overall accuracy (0.9799), recall (0.9806), F1-score (0.9806), and third-best precision (0.9806). This dataset improved the performance of the approach in classifying building instances, attaining a mean improvement of 1.9975.

The RGB and TGI combination achieved the second-highest OA of 0.9714, the highest precision and F1-score of 0.9880 and 0.9704, respectively, and the third-best recall value of 0.9368, amounting to an average improvement of 0.6900.

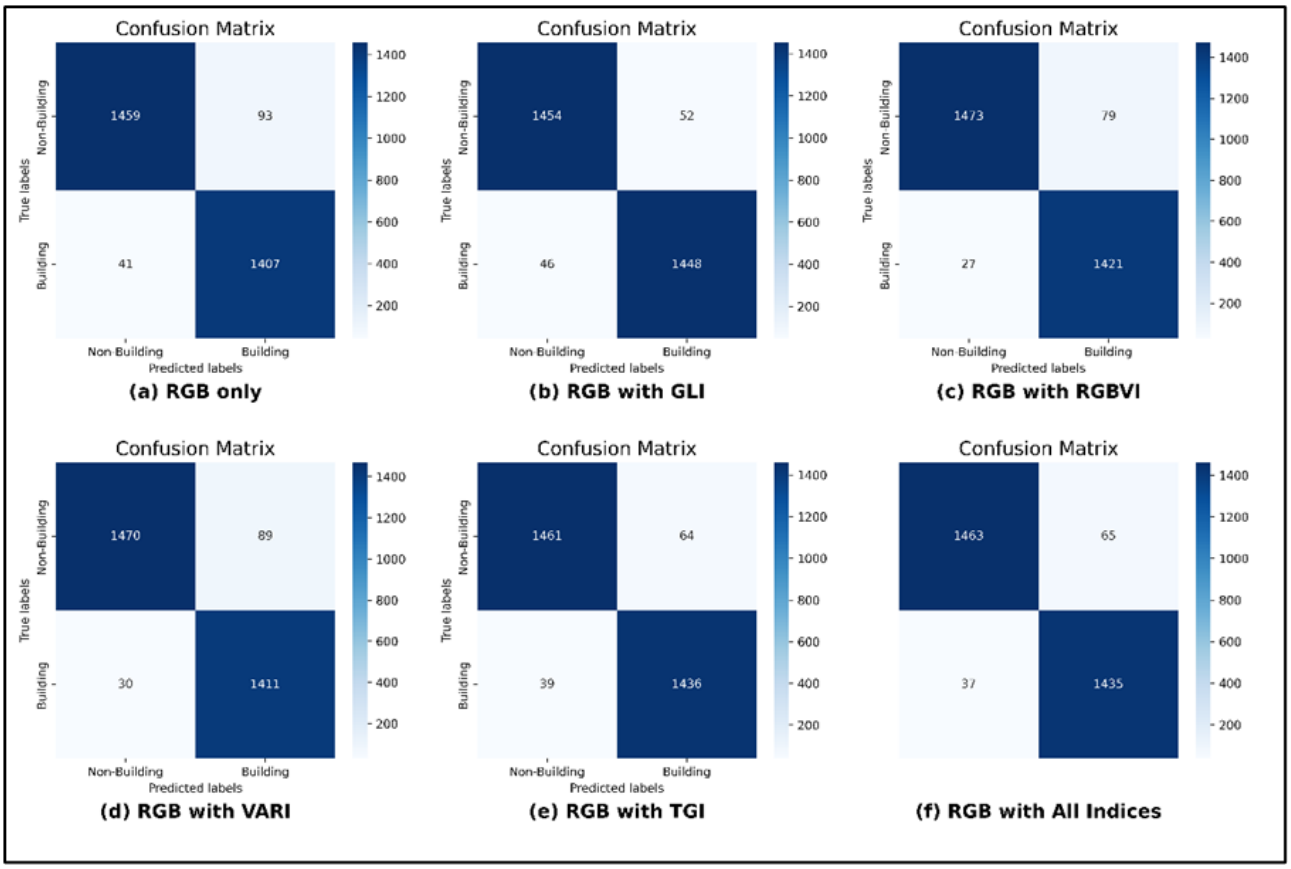

Figure 7. Confusion matrix for classification result validation.

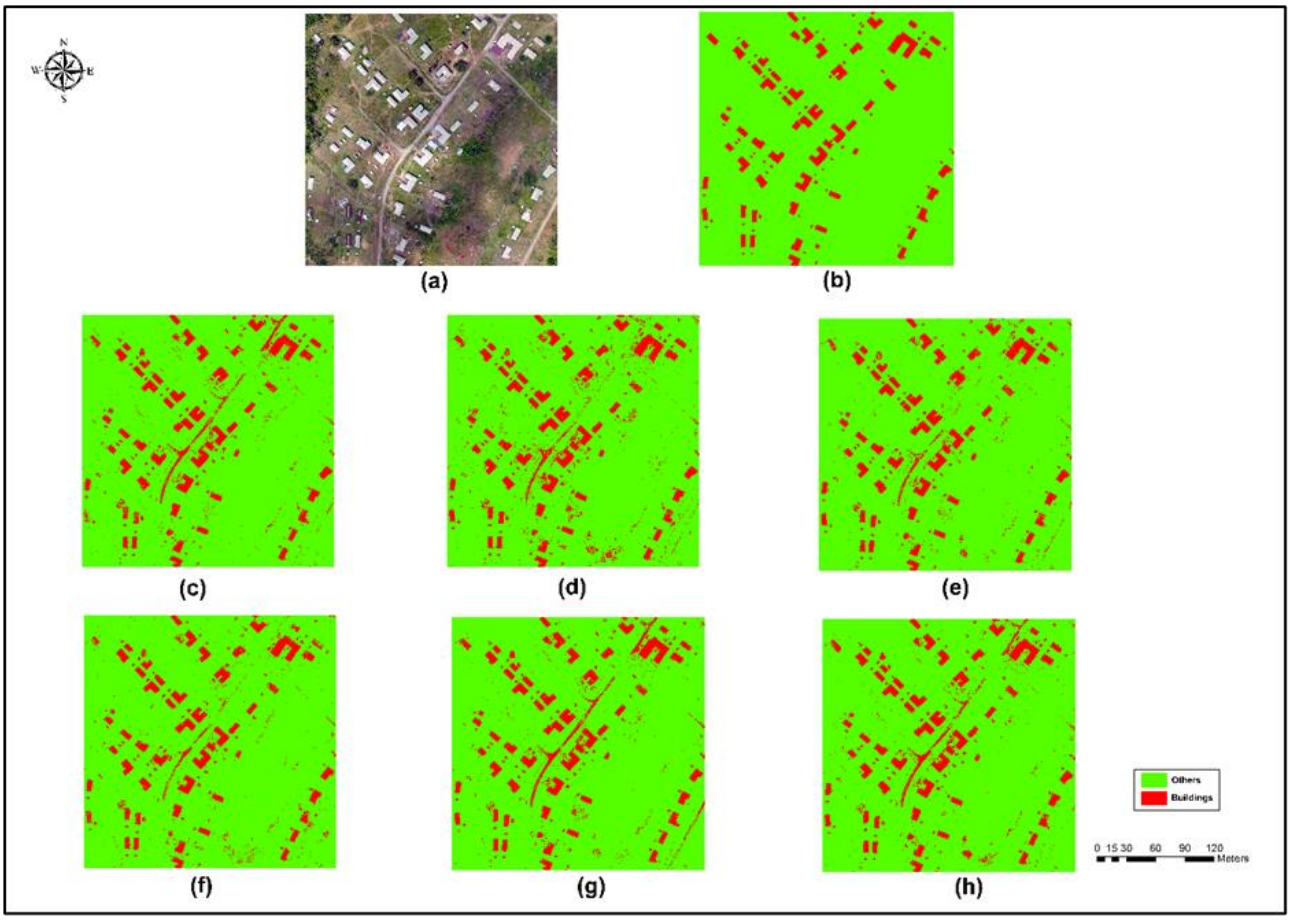

Figure 8. Building Extraction Results RF Classifier (a) UAV Image, (b) RGB + GLI, (c) RGB + RGBVI, (d) RGB + VARI, (e) RGB + TGI, and (f) RGB + All Indices.

The combination of RGB and RGBVI had the second-best recall (0.9671), third-best OA (0.9660), and F1-score (0.9671) values, and the fourth-best precision (0.9671). Thus, combining the RGBVI with the RGB orthophoto improved the classification approach by an average of 0.7075.

The RGB and GLI combination achieved the highest precision (0.9890). Notwithstanding, it ranked fourth in terms of overall accuracy (0.9632) and F1-score (0.9648) and fifth in recall (0.9411), which was lower than the standalone RGB combination. This combination attained a mean improvement of 0.6625.

The combination of all the RGB VIs and the RGB orthophoto had the least values for all the metrics, attaining an OA of 0.950, precision of 0.9570, recall of 0.9368, and F1-score of 0.9468. This result implies that combining all the VIs with RGB orthophoto decreased the performance of the building extraction approach by an average of -0.3975.

When considering only the RGB orthophoto, the overall accuracy, precision, recall, and F1-score values were 0.9565, 0.9643, 0.9529, and 0.9586, respectively, with the recall value ranking third, surpassing the RGB with GLI and RGB with all indices combinations.

The quantitative assessment of the classification result in Table 3 indicated that the RGB and GLI combination attained the best classification compared to the ground truth. The RGB and GLI attained the highest overall accuracy (0.9673), precision (0.9655) and F1-score (0.9674). Interestingly, this combination attained the lowest recall value of 0.9693.

Combining all the VIs with the RGB orthophoto achieved the second-best overall accuracy (0.9660) and F1-score (0.9663). This dataset combination also attained the third-best scores for precision (0.9575) and recall (0.9753). These scores contrast sharply to those attained for the test sample, where the dataset attained the lowest scores.

The third-best classification result was obtained by combining RGB and TGI. This dataset obtained the second-best score for precision (0.9580), the third-best score for overall accuracy (0.9657), and the F1-score (0.9660). For recall, this dataset obtained the fourth-best score of 0.9740.

From Table 3, the RGB and VARI dataset had the fourth-best classification output. This combination had the second-best recall value of 0.9800 and the fifth-best values for overall accuracy (0.9603) and precision (0.9429). Notwithstanding, the dataset attained the lowest value of 0.9611 for the F1-score.

The RGB and RGVI dataset achieved the fourth-best values for overall accuracy (0.9647) and precision (0.9491). This dataset also gained the fifth-best result (0.9653) for F1-score and the lowest value (0.9820) for recall.

Lastly, the RGB dataset had the lowest classification performance. This dataset had the lowest values of 0.9553 and 0.9401 for overall accuracy and precision, respectively. Nevertheless, the dataset attained the fourth-best value for F1-score (0.9561) and the fifth-best value for recall (0.9727).

These two results underscore the contribution of the VIs in the building extraction pipeline. Nonetheless, it is evident that the VIs had varying performances. From the test dataset, it is evident that the RGB and VARI dataset outperforms the other datasets in terms of overall accuracy (OA), precision (P), recall (R), and F1-score. It was also interesting to note that the RGB and all Indices dataset performed slightly worse than the UAV-RGB only dataset. This dataset attaining the worst performance on the test data can be attributed to the curse of dimensionality, where redundant spectral information from the VIs introduced noise and multicollinearity. Thus, the effectiveness of a classification model is hindered, and the chance of overfitting the training dataset is increased [49]. The result from the classification showed a slight difference from the testing sample results. While the RGB and VARI dataset still performs well, the RGB and GLI and RGB and all Indices datasets demonstrated an improved performance.

The qualitative maps in Figure 8 show that the datasets produced similar visual outputs. All the datasets could identify and extract the outlines of the buildings of within the image. However, just like most attempts of automation in building extraction, there is the need for some manual editing and revision [50]. From Figure 6, it is noticeable that there was confusion among building rooftops and impervious surfaces such as roads and soil surfaces. This cataclysm resulted in commission errors, leading to an inconsistent classification. This can be attributed to the VIs' strength in differentiating between vegetation and non-vegetation rather than among urban features. Figure 6 shows that all the datasets falsely classified a section of the central road as a building.

5. Conclusion

This study aimed to assess the contribution of four RGB VIs, GLI, RGBVI, VARI, and TGI, in improving building classification tasks from UAV imagery. To that aim, four datasets containing a combination of these VIs and RGB-UAV were created, and a GeoBIA approach was adopted to classify building features from these datasets. In addition, a fifth dataset was created by combining all the RGB VIs and the UAV image.

The experimental results highlight the advantages of integrating vegetative indices into building extraction from UAV-RGB imagery. The RGB and VARI dataset emerged as the top-performing combination, achieving the highest overall accuracy, precision, recall, and F1-score on the test dataset. However, it is worth noting that the RGB and GLI dataset stood out for its exceptional precision. This result was useful during the classification step, where the dataset attained the result. Thus, it produced a classification result that was similar to the ground truth mask.

In conclusion, integrating the RGB-based VIs into the GeoBIA classification pipeline significantly improved the accuracy of building extraction from UAV-RGB imagery. Nevertheless, the choice of VIs and their combination plays a crucial role in the performance of the extraction approach. The combined use of all indices does not consistently outperform individual indices, emphasizing the significance of selecting relevant combinations. Future research could focus on choosing the best combination of VIs that further enhance the performance

of building extraction. Also, other machine-learning classifiers can be adopted, and their performance can be assessed during the classification step.

Author contributions

Richmond Akwasi Nsiah: Conceptualization, Methodology, Investigation, Software and Scripting, Data Curation, Validation, Writing—original draft preparation, Writing—review and editing, **Visualization Saviour Mantey:** Conceptualization, Methodology, Investigation, Validation, Writing—original draft preparation, Writing—review and editing, Visualization, Supervision **Yao Yevenyo Ziggah:** Conceptualization, Methodology, Investigation, Validation, Writing—original draft preparation, Writing—review and editing, Visualization, Supervision.

Conflicts of interest

The authors declare no conflicts of interest.

References

1. Schlosser, A. D., Szabó, G., Bertalan, L., Varga, Z., Enyedi, P., & Szabó, S. (2020). Building extraction using orthophotos and dense point cloud derived from visual band aerial imagery based on machine learning and segmentation. Remote Sensing, 12(15), 2397. https://doi.org/10.3390/rs12152397
2. Hu, Q., Zhen, L., Mao, Y., Zhou, X., & Zhou, G. (2021). Automated building extraction using satellite remote sensing imagery. Automation in Construction, 123, 103509. https://doi.org/10.1016/j.autcon.2020.103509
3. Li, J., Huang, X., Tu, L., Zhang, T., & Wang, L. (2022). A review of building detection from very high resolution optical remote sensing images. GIScience & Remote Sensing, 59(1), 1199-1225. https://doi.org/10.1080/15481603.2022.2101727
4. Dai, Y., Gong, J., Li, Y., & Feng, Q. (2017). Building segmentation and outline extraction from UAV image-derived point clouds by a line growing algorithm. International Journal of Digital Earth, 10(11), 1077-1097. https://doi.org/10.1080/17538947.2016.1269841
5. Temenos, A., Temenos, N., Doulamis, A., & Doulamis, N. (2022). On the exploration of automatic building extraction from RGB satellite images using deep learning architectures based on U-Net. Technologies, 10(1), 19. https://doi.org/10.3390/technologies10010019
6. Daranagama, S., & Witayangkurn, A. (2021). Automatic building detection with polygonizing and attribute extraction from high-resolution images. ISPRS International Journal of Geo-Information, 10(9), 606. https://doi.org/10.3390/ijgi10090606
7. Lin, Huertas, & Nevatia. (1994). Detection of buildings using perceptual grouping and shadows. In 1994 Proceedings of IEEE Conference on Computer Vision and Pattern Recognition, 62-69. https://doi.org/10.1109/CVPR.1994.323811
8. Jaynes, C. O., Stolle, F., & Collins, R. T. (1994, December). Task driven perceptual organization for extraction of rooftop polygons. In Proceedings of 1994 IEEE Workshop on Applications of Computer Vision, 152-159. https://doi.org/10.1109/ACV.1994.341303
9. Chen, R., Li, X., & Li, J. (2018). Object-based features for house detection from RGB high-resolution images. Remote Sensing, 10(3), 451. https://doi.org/10.3390/rs10030451
10. Lu, T., Ming, D., Lin, X., Hong, Z., Bai, X., & Fang, J. (2018). Detecting building edges from high spatial resolution remote sensing imagery using richer convolution features network. Remote Sensing, 10(9), 1496. https://doi.org/10.3390/rs10091496
11. Cheng, G., & Han, J. (2016). A survey on object detection in optical remote sensing images. ISPRS Journal of Photogrammetry and Remote Sensing, 117, 11-28. https://doi.org/10.1016/j.isprsjprs.2016.03.014
12. Lefèvre, S., Weber, J., & Sheeren, D. (2007). Automatic building extraction in VHR images using advanced morphological operators. In 2007 Urban Remote Sensing Joint Event, 1-5. https://doi.org/10.1109/URS.2007.371825
13. Ahmadi, S., Zoej, M. V., Ebadi, H., Moghaddam, H. A., & Mohammadzadeh, A. (2010). Automatic urban building boundary extraction from high resolution aerial images using an innovative model of active contours. International Journal of Applied Earth Observation and Geoinformation, 12(3), 150-157. https://doi.org/10.1016/j.jag.2010.02.001
14. Yari, D., Mokhtarzade, M., Ebadi, H., & Ahmadi, S. (2014). Automatic reconstruction of regular buildings using a shape-based balloon snake model. The Photogrammetric Record, 29(146), 187-205. https://doi.org/10.1111/phor.12060
15. Huertas, A., & Nevatia, R. (1988). Detecting buildings in aerial images. Computer Vision, Graphics, and Image Processing, 41(2), 131-152. https://doi.org/10.1016/0734-189X(88)90016-3
16. Peng, J., & Liu, Y. C. (2005). Model and context-driven building extraction in dense urban aerial images. International Journal of Remote Sensing, 26(7), 1289-1307. https://doi.org/10.1080/01431160512331326675
17. Sirmacek, B., & Unsalan, C. (2008). Building detection from aerial images using invariant color features and shadow information. In 2008 23rd International Symposium on Computer and Information Sciences, 1-5. https://doi.org/10.1109/ISCIS.2008.4717854
18. Liow, Y. T., & Pavlidis, T. (1990). Use of shadows for extracting buildings in aerial images. Computer Vision, Graphics, and Image Processing, 49(2), 242-277. https://doi.org/10.1016/0734-189X(90)90139-M
19. Irvin, R. B., & McKeown, D. M. (1989). Methods for exploiting the relationship between buildings and their shadows in aerial imagery. IEEE Transactions

on Systems, Man, and Cybernetics, 19(6), 1564-1575. https://doi.org/10.1109/21.44071
20. Wu, G., Shao, X., Guo, Z., Chen, Q., Yuan, W., Shi, X., ... & Shibasaki, R. (2018). Automatic building segmentation of aerial imagery using multi-constraint fully convolutional networks. Remote Sensing, 10(3), 407. https://doi.org/10.3390/rs10030407
21. Kokeza, Z., Vujasinović, M., Govedarica, M., Milojević, B., & Jakovljević, G. (2020). Automatic building footprint extraction from UAV images using neural networks. Geodetski Vestnik, 64(04), 545-561. https://doi.org/10.15292/geodetski-vestnik.2020.04.545-561
22. Norman, M., Shahar, H. M., Mohamad, Z., Rahim, A., Mohd, F. A., & Shafri, H. Z. M. (2021). Urban building detection using object-based image analysis (OBIA) and machine learning (ML) algorithms. In IOP Conference Series: Earth and Environmental Science, 620(1), 012010. https://doi.org/10.1088/1755-1315/620/1/012010
23. Comert, R., & Kaplan, O. (2018). Object based building extraction and building period estimation from unmanned aerial vehicle data. ISPRS Annals of Photogrammetry, Remote Sensing and Spatial Information Sciences, 4(3), 71-76. https://doi.org/10.5194/isprs-annals-IV-3-71-2018
24. Aminipouri, M. (2009). Object-oriented analysis of very high resolution orthophotos for estimating the population of slum areas, case of Dar-Es-Salaam, Tanzania [Master's thesis, University of Twente].
25. Guo, Z., & Du, S. (2017). Mining parameter information for building extraction and change detection with very high-resolution imagery and GIS data. GIScience & Remote Sensing, 54(1), 38-63. https://doi.org/10.1080/15481603.2016.1250328
26. Benarchid, O., Raissouni, N., El Adib, S., Abbous, A., Azyat, A., Achhab, N. B., ... & Chahboun, A. (2013). Building extraction using object-based classification and shadow information in very high resolution multispectral images, a case study: Tetuan, Morocco. Canadian Journal on Image Processing and Computer Vision, 4(1), 1-8.
27. Frishila, A. A., & Kamal, M. (2019). The effectiveness of spectral features for building extraction using geographic object-based image analysis (GEOBIA). The 40th Asian Conference on Remote Sensing (ACRS 2019), 1-10.
28. Hossain, M. D., & Chen, D. (2022). A hybrid image segmentation method for building extraction from high-resolution RGB images. ISPRS Journal of Photogrammetry and Remote Sensing, 192, 299-314. https://doi.org/10.1016/j.isprsjprs.2022.08.024
29. Dornaika, F., Moujahid, A., El Merabet, Y., & Ruichek, Y. (2016). Building detection from orthophotos using a machine learning approach: An empirical study on image segmentation and descriptors. Expert Systems with Applications, 58, 130-142. https://doi.org/10.1016/j.eswa.2016.03.024
30. Argyridis, A., & Argialas, D. P. (2016). Building change detection through multi-scale GEOBIA approach by integrating deep belief networks with fuzzy ontologies. International Journal of Image and Data Fusion, 7(2), 148-171. https://doi.org/10.1080/19479832.2016.1158211
31. Davydova, K., Cui, S., & Reinartz, P. (2016). Building footprint extraction from digital surface models using neural networks. In Image and Signal Processing for Remote Sensing XXII, 10004, 187-196. https://doi.org/10.1117/12.2240727
32. Li, Y., Zhu, L., Shimamura, H., & Tachibanab, K. (2010). An integrated system on large scale building extraction from DSM. The International Archives of the Photogrammetry, Remote Sensing and Spatial Information Sciences, 38, 35-39.
33. Singh, D., Maurya, R., Shukla, A. S., Sharma, M. K., & Gupta, P. R. (2012). Building extraction from very high resolution multispectral images using NDVI based segmentation and morphological operators. In 2012 Students Conference on Engineering and Systems, 1-5. https://doi.org/10.1109/SCES.2012.6199034
34. Öztürk, M. Y., & Çölkesen, İ. (2021). The impacts of vegetation indices from UAV-based RGB imagery on land cover classification using ensemble learning. Mersin Photogrammetry Journal, 3(2), 41-47. https://doi.org/10.53093/mephoj.943347
35. Kucharczyk, M., Hay, G. J., Ghaffarian, S., & Hugenholtz, C. H. (2020). Geographic object-based image analysis: a primer and future directions. Remote Sensing, 12(12), 2012. https://doi.org/10.3390/rs12122012
36. Achanta, R., Shaji, A., Smith, K., Lucchi, A., Fua, P., & Süsstrunk, S. (2012). SLIC superpixels compared to state-of-the-art superpixel methods. IEEE Transactions on Pattern Analysis and Machine Intelligence, 34(11), 2274-2282. https://doi.org/10.1109/TPAMI.2012.120
37. Liao, N., Liu, H., Li, C., Ren, X., & Guo, B. (2022). Simple linear ıterative clustering with efficiency. Advances in Intelligent Information Hiding and Multimedia Signal Processing, 1, 109-117. https://doi.org/10.1007/978-981-19-1057-9_11
38. Zhang, H., & Zhu, Y. (2019). Kslic: K-mediods clustering based simple linear iterative clustering. In Chinese Conference on Pattern Recognition and Computer Vision (PRCV), 519-529. https://doi.org/10.1007/978-3-030-31723-2_44
39. Sibaruddin, H. I., Zulhaidi, H., Shafri, M., Pradhan, B., & Haron, N. A. (2018). UAV-based approach to extract topographic and as-built information by utilising the OBIA technique. Journal of Geosciences and Geomatics, 6(3), 103-123. https://doi.org/10.12691/jgg-6-3-2
40. Norman, M., Shahar, H. M., Mohamad, Z., Rahim, A., Mohd, F. A., & Shafri, H. Z. M. (2021). Urban building detection using object-based image analysis (OBIA) and machine learning (ML) algorithms. IOP Conference Series: Earth and Environmental Science, 620(1), 1-11. https://doi.org/10.1088/1755-1315/620/1/012010
41. Breiman, L. (2001). Random forests. Machine Learning, 45, 5-32.
42. Kumar, A., & Sinha, N. (2020). Classification of forest cover type using random forests algorithm.

In Advances in Data and Information Sciences: Proceedings of ICDIS 2019, 94, 395-402. https://doi.org/10.1007/978-981-15-0694-9_37
43. Xiao, Y., Huang, W., & Wang, J. (2020). A random forest classification algorithm based on dichotomy rule fusion. In 2020 IEEE 10th International Conference on Electronics Information and Emergency Communication (ICEIEC), 182-185. https://doi.org/10.1109/ICEIEC49280.2020.9152236
44. Jiang, J., Cai, W., Zheng, H., Cheng, T., Tian, Y., Zhu, Y., ... & Yao, X. (2019). Using digital cameras on an unmanned aerial vehicle to derive optimum color vegetation indices for leaf nitrogen concentration monitoring in winter wheat. Remote Sensing, 11(22), 2667. https://doi.org/10.3390/rs11222667
45. Hunt Jr, E. R., Doraiswamy, P. C., McMurtrey, J. E., Daughtry, C. S., Perry, E. M., & Akhmedov, B. (2013). A visible band index for remote sensing leaf chlorophyll content at the canopy scale. International Journal of Applied Earth Observation and Geoinformation, 21, 103-112. https://doi.org/10.1016/j.jag.2012.07.020
46. Bendig, J., Yu, K., Aasen, H., Bolten, A., Bennertz, S., Broscheit, J., ... & Bareth, G. (2015). Combining UAV-based plant height from crop surface models, visible, and near infrared vegetation indices for biomass monitoring in barley. International Journal of Applied Earth Observation and Geoinformation, 39, 79-87. https://doi.org/10.1016/j.jag.2015.02.012
47. Gitelson, A. A., Kaufman, Y. J., Stark, R., & Rundquist, D. (2002). Novel algorithms for remote estimation of vegetation fraction. Remote Sensing of Environment, 80(1), 76-87. https://doi.org/10.1016/S0034-4257(01)00289-9
48. Louhaichi, M., Borman, M. M., & Johnson, D. E. (2001). Spatially located platform and aerial photography for documentation of grazing impacts on wheat. Geocarto International, 16(1), 65-70. https://doi.org/10.1080/10106040108542184
49. Kaur, R., & Pandey, P. (2022). A review on spectral indices for built-up area extraction using remote sensing technology. Arabian Journal of Geosciences, 15(5), 391. https://doi.org/10.1007/s12517-022-09688-x
50. Tsai, Y. H., Stow, D., & Weeks, J. (2011). Comparison of object-based image analysis approaches to mapping new buildings in Accra, Ghana using multi-temporal QuickBird satellite imagery. Remote Sensing, 3(12), 2707-2726. https://doi.org/10.3390/rs3122707

Mersin Photogrammetry Journal

https://dergipark.org.tr/en/pub/mephoj

e-ISSN 2687-654X

Estimating the efficacy of solar photovoltaic panels in Lebanon using a digital surface model: A geospatial approach

Jean Doumit *[1]

[1] *Lebanese University, Faculty of Letters and Human Sciences, Department of Geography, Geospatial Lab, Lebanon, jeandoumit@gmail.com*

Cite this study: Doumit, J. (2024). Estimating the efficacy of solar photovoltaic panels in Lebanon using a digital surface model: A geospatial approach. Mersin Photogrammetry Journal, 6 (1), 22-31

https://doi.org/10.53093/mephoj.1401603

Keywords
Solar radiation
Solar duration
Solar photovoltaic
Photogrammetry
GIS

Research Article

Received: 07.12.2023
Revised: 08.01.2024
Accepted: 15.01.2024
Published:16.03.2024

Abstract

With the escalating need for alternative energy sources due to economic crises and fossil fuel shortages in Lebanon, solar photovoltaic (PV) panels have emerged as an attractive solution. This study examines the capacity and efficacy of rooftop-installed PV solar panels. Using geospatial technologies, including Digital Surface Models drone-based photogrammetry, the study assesses geometric and solar characteristics, seasonal solar radiation, solar duration, and power for 40 PV units installed in the study area. This research presents specific quantitative values for optimal orientations that result in high solar radiation across various seasons and identifies varying slopes influencing the performance of PV solar panels. Employing the Agglomerative Hierarchical Clustering (AHC) technique, PV units are systematically classified into clusters labeled as Moderate, High, Low, and Very Low solar power, offering quantitative metrics regarding the effectiveness of distinct panels. The high-efficiency Cluster exhibits an average solar power of 1868.114 kWh/m^2 during the summer season, whereas the Very Low Cluster, comprising panels with minimal solar power output, averages 150.578 kWh/m^2 in the same season. In conclusion, the most effective PV solar panels within the study area are those oriented between 195 and 225 degrees, with shallow inclination angles and larger surface areas contributing to enhanced performance in capturing solar radiation and generating power. These precise quantitative insights contribute to informed decision-making for optimizing the placement of PV panels to enhance energy generation. The study's recommendations are substantiated by specific numerical data, guiding future solar installations to maximize solar energy generation.

1. Introduction

Due to the economic crisis that struck Lebanon in late 2019, coupled with power outages caused by fossil fuel shortages and high prices, the depletion of global fossil fuel resources has prompted a critical search for alternative energy sources to meet contemporary demands. Once considered an expensive and inefficient method of generating electricity, solar PV panels have become increasingly affordable and appealing when compared to rising energy prices from non-renewable sources. Solar power has also grown more accessible to homeowners.

Individuals have installed solar panels on building roofs to generate electricity for their household needs. Certain residents have achieved energy independence and reduced reliance on the public electricity grid. PV technology directly converts solar energy into electricity based solely on the availability and quality of renewable resources, technical system performance, topographic limitations, and environmental and land-use constraints [1].

PV technology stands as one of the fastest-growing technologies worldwide. It boasts independence and adaptability to various scenarios, making it versatile. It can seamlessly integrate with smart grid networks and can also be tailored for small-scale applications like stand-alone PV power systems on rooftops [2,3].

Numerous solar radiation estimation models, such as remote sensing, geo-statistics, and Geographic Information Systems (GIS), have been developed to provide a more cost-effective and convenient way of measuring radiation, as opposed to deploying multiple sensors to the area for direct measurement.

Using GIS has gained momentum in renewable energy across various regions of the world. It has proven invaluable in developing spatial decision support systems, aiding decision-makers in resolving spatially

related issues by leveraging geographical controlling factors [4].

On a global scale, the primary controlling factors include latitude, distance from the sun, and the time of the year. On a local scale, significant sources of spatial variation encompass elevation above sea level, surface inclination, surface orientation, and the shadowing effects of nearby terrain features [5].

In this study, weather conditions were excluded due to their instability, unpredictability, and the challenges associated with modeling cloud patterns. Atmospheric conditions can span from overcast skies and clear skies to partly cloudy skies, direct sunlight, and uniform skies. The solar radiation for the study area was calculated under clear-sky conditions.

As interest in solar power generation continues to rise, the number of published studies evaluating the photovoltaic (PV) potential of different regions has steadily increased for more than a decade.

The Energy Sector Management Assistance Program (ESMAP) has identified the theoretical, practical, and economic potential of PV in each country, presented through maps and summary tables. This resource could serve as a foundation for global study [6].

One area of research is dedicated to precisely estimating the power production of photovoltaic (PV) systems installed on building roofs and identifying potential locations for solar energy harvesting [6].

The research conducted by [7] assessed the solar energy potential across Europe. On a more localized level, individual country and regional studies strive to pinpoint and suggest viable solar energy project opportunities. These studies utilize methodologies such as multiple-criteria decision-making (MCDM), the analytic hierarchy process (AHP), and fuzzy logic, to establish recommendations for solar energy development.

Choi et al. [8] reviewed geographic information system (GIS)-based methods and their applications in the planning and design of solar power systems. They categorized GIS-based studies into three main groups: 1) solar radiation mapping, 2) site evaluation, and 3) potential assessment. The review involved classifying previous GIS-based studies into subtopics based on factors such as the complexity of the GIS methods employed, the solar power conversion technology, or the scale of the study area.

The majority of GIS research and its applications in solar power have focused on identifying the potential for solar panels [9-11], suitability for PV farms [12], and feasibility of PV implementation [13,14]. There has been a lack of research examining the capacity of PV solar panels after installation using geospatial technologies.

Our study introduces a fourth category to the three groups identified by [8]. This category will delve into the efficacy of rooftop-installed PV solar panels, specifically focusing on their capacity to generate electricity. However, to our knowledge, no such assessment has been published at the micro level. This research gap underscores the significance of our study within the local solar industry, we analyze the capacity of rooftop PV solar panels within a small area of the El Meten region in Lebanon.

There are three primary causes of spatial variability in radiation at the land surface: (1) the orientation of the Earth relative to the sun, (2) clouds and other atmospheric inhomogeneities, and (3) topography. The first cause influences latitudinal gradients and seasons. The second cause is linked to local weather and climate, but it will not be addressed in this study. The third cause, including spatial variability in elevation, slope, aspect, and shadowing, can give rise to pronounced local gradients in solar radiation. These gradients support our study [15].

Topographic effects on direct radiation were calculated for each grid node in a Digital Surface Model (DSM) using the spatial analysis tool within ArcGIS Pro, over Fall, Winter, Spring, and Summer. Sun elevation and azimuth were factored in.

Digital Surface Models (DSM) and Ortho mosaics, generated through drone photogrammetry and Geographic Information System (GIS) technology, were utilized for analyzing the capacity and efficacity of the pre-installed rooftop PV solar panels.

The utilization of drones was preferred over previously available digital elevation data due to their higher precision and ability to identify rooftop solar panels accurately.

The surface model was also employed to calculate panel slopes and aspects, aiding in identifying the optimal locations and orientations for the installed photovoltaic solar cells. Solar radiation duration and power were computed for each of the four seasons: Fall, Winter, Spring, and Summer

This study serves as an initial step toward developing a plan by assessing the solar potential and power generation capacity of rooftop solar panels. Leveraging geospatial data enables the calculation of a more precise estimation of solar capacity for structures across the entire region. Traditional methods have often relied on less accurate datasets like bare earth Digital Elevation Models or time-consuming individual property assessments. Through the utilization of drone photogrammetry to generate high-resolution elevation data, the Digital Surface Model (DSM) can influence solar energy specifically on the Earth's surface [16].

It's important to note that not all rooftop PV systems are installed uniformly. Evaluating the efficacy of these solar panels can be achieved through manual surveys conducted by experts in the field. However, this approach is highly impractical for estimating PV efficacity over a larger region with numerous rooftops.

This study aims to address these questions:

1. What are the geometrical and solar characteristics of the installed PV units that exhibit high solar radiation and power?

2. How can PV solar panels be categorized based on their efficacity?

2. Materials and method

In Lebanon, a Middle Eastern country, there is an urbanized area of 5 hectares in the El Meten region. According to the Global Solar Atlas 2.0, the long-term yearly average of potential photovoltaic electricity production, covering the period between 1999 and 2018,

was 1583 kWh. This value is promising for conducting solar energy experiments [17].

The experiment area is relatively small due to restrictions on drone flights in urban areas and the limited endurance of drone batteries.

The study area in Figure 1 is characterized by its urban structure, which includes a variety of small private homes and large residential buildings suitable for the installation of PV solar panels.

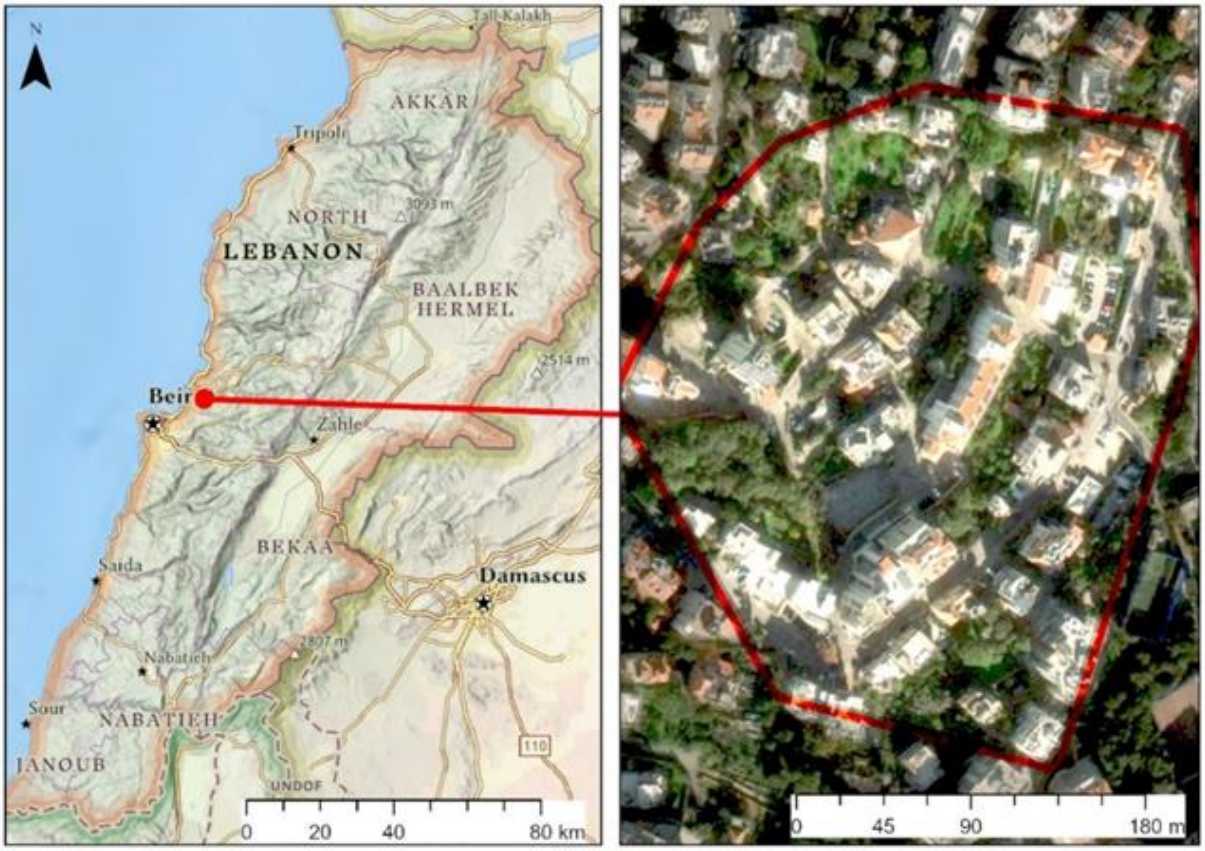

Figure 1. Study area.

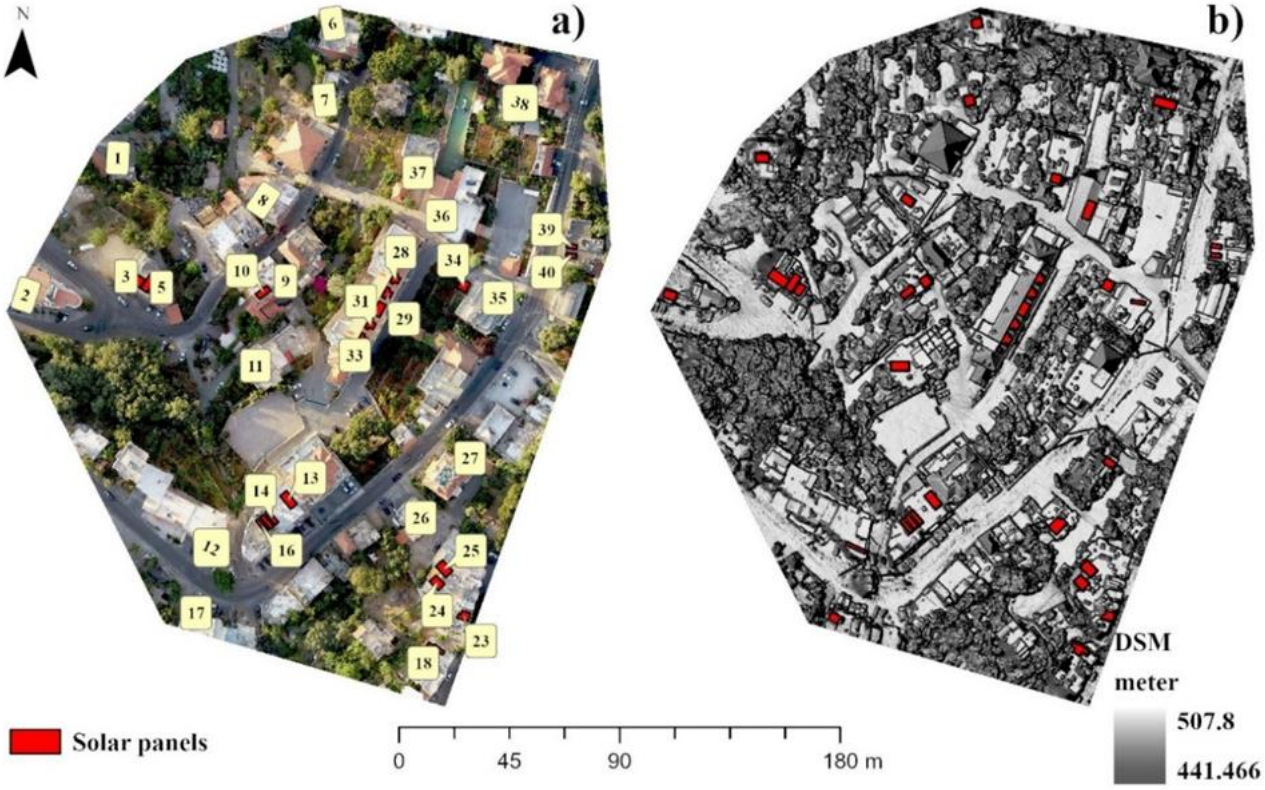

Figure 2. a) Ortho mosaic with the numbers of PV solar panels, b) The DSM with the PV solar panels.

For the photogrammetry mission, a DJI Phantom 4 with a 20-megapixel camera was employed. The drone was flown at a height of 100 meters from the take-off point, capturing 46 aerial frames with an 80% overlap and 70% side lap. These overlaps would generate a dense point cloud for Ortho mosaic and DSM production.

To ensure accuracy, 10 control points were strategically placed on the ground and surveyed using a differential Global Navigation Satellite System receiver. This receiver boasted a horizontal accuracy of 0.5 cm and a vertical accuracy of 2 cm, which proved to be more than adequate for solar study purposes.

The resulting Ortho mosaic, with a spatial resolution of 4 cm, was employed to digitize the PV solar panels in Figure 2a. Figure 2 depicts 40 PV units, each of which could consist of 2 or more panels.

Concurrently, a DSM was generated with a spatial resolution of 7 cm to be used for solar radiation and solar duration calculations.

Figure 2a of the Ortho mosaic showcases the 40 digitized PV units composed of solar panels with varying areas and orientations. These panels were installed without prior studies and are predominantly oriented towards the East-South direction.

Figure 2b of the DSM illustrates elevation intervals above sea level, ranging from 441 to 507 meters, effectively displaying building and tree heights.

Solar radiation received from the sun stands as the primary energy source for PV panels, rendering an understanding of its significance at landscape scales crucial for comprehending an array of natural processes and human activities.

Within landscape scales, topography emerges as a pivotal determinant of the spatial fluctuations in solar radiation. These fluctuations evolve with the progression of the day and the shifting of seasons, contributing to the variations in microclimates. These microclimatic differences encompass elements like air and soil temperatures, evapotranspiration, patterns of snowmelt, soil moisture, and light accessible for photosynthesis.

The computation of solar radiation was executed through the utilization of the area solar radiation tool within ArcGIS Pro, aligned with the DSM derived from drone-based photogrammetry as the primary input. However, this study did not delve into investigating the accuracy and quality of the resulting DSM.

The ArcGIS Pro Spatial Analyst extension facilitates the mapping and analysis of solar effects employing techniques rooted in the hemispherical viewshed algorithm [5]. This approach incorporates considerations for atmospheric influences, site latitude and elevation, slope steepness, compass direction (aspect), daily and seasonal variations in solar angles, and the impacts of shadows cast by surrounding topography, as expressed by the DSM grid.

The latitude (33.9304) at the center of the study area is employed in calculating solar declination and solar positioning. Given that the analysis is tailored for micro scales, the practice of utilizing a single latitude value for the entire DSM is generally acceptable. However, for global scales, insolation outcomes would notably diverge across distinct latitudes, necessitating division into zones characterized by different latitudes.

Solar effects are computed based on distinct seasonal periods—Fall, Winter, Summer, and Spring. When determining the most suitable orientation for installations, it is crucial to account for the sun's relative angular position throughout the year and day.

During Summer in the Northern Hemisphere, the region is inclined towards the sun, leading to more direct solar rays striking the ground from the first of June until the first of September. Conversely, in Winter, spanning from the first of December till the first of March, the Northern Hemisphere is oriented away from the sun [18].

Considering these factors, for installations within the Northern Hemisphere, a southern exposure is typically considered optimal for capturing the highest intensity of sunlight overall [19,20].

The solar radiation output raster data in Figure 3 are of the floating-point type and are measured in units of Kilowatt hours per square meter (kWh/m^2).

In the SAGA GIS software, the seasonal average solar duration was computed using the DSM derived from drone data. The resulting solar duration output, presented as an integer raster, represents the mean value across Fall, Winter, Spring, and Summer, measured in hours.

It's worth noting that the performance of PV solar power plants is generally not significantly impacted by temperature [12]. The value of solar radiation estimates the potential electricity generation within each PV unit.

The seasonal solar energy production is determined by the dimensions of the PV solar panels, which are outlined in a shape file digitized from the Ortho mosaic. The unit of solar electricity power (UP) is calculated following the method [21] outlined by Equation 1.

$$UP = A \times SR_{Season} \times 0.163 \times 0.8592 \quad (1)$$

UP = Unit Power (kWh)
r = 16.3% PV solar panel efficiency of PV modules
PR = 85.92% performance ratio (PV Watts Calculator: 14.08% system losses)
SR is the mean solar radiation received per unit area (kWh/m^2) each season,
A is PV solar panel unit area (m^2),

The value of the efficiency (r) used is adopted from the National Renewable Energy Laboratory of the USA [21].

To accurately estimate solar radiation across the study area throughout the four seasons, a high-resolution solar radiation raster was computed using the solar radiation module within ArcGIS Pro. This module considers a variety of factors, including atmospheric influences, site latitude and elevation, slope steepness, compass direction (aspect), daily and seasonal shifts in the sun angle, and the impacts of shadows cast by surrounding topography. It provides the flexibility to adjust the coefficient of atmospheric transmissivity, as detailed by [12].

The model's calculations encompass the summation of direct and diffuse radiation across all sectors of both sun maps and sky maps. The primary input parameters employed in this model were derived from the DSM

generated through drone-based photogrammetry, as depicted in Figure 2b.

Following the GIS processing steps for generating slopes, aspect, SR, SD, and UP values, a zonal statistics analysis was conducted for the PV units. This analysis facilitated the extraction of the geometric and solar characteristics of the 40 photovoltaic units.

3. Results and Discussion

The 40 PV units of solar panels were delineated from the ortho mosaic generated. Then utilizing the integrated DSM within ArcGIS Pro, the seasonal Solar Radiation (SR) depicted in Figure 3 was produced.

Four raster data displaying the average solar duration for each season—Fall, Winter, Spring, and Summer were generated. These raster data were developed by considering the elevations from the DSM data, utilizing SAGA software.

The Unit Power of the solar panels was calculated according to equation number 1.

In the fall season, the maximum solar radiation reaches 338.208 kWh/m^2, and this value declines to 252.428 kWh/m^2 during the winter period, as illustrated in Figure 3b. These calculations do not consider the influence of atmospheric conditions. Moving into the spring season, solar radiation increases to 473.158 kWh/m^2, further reaching an average of 537.235 kWh/m^2 during the summer. This increase is pronounced on rooftops and in open areas, exemplified by the red regions in Figure 3d.

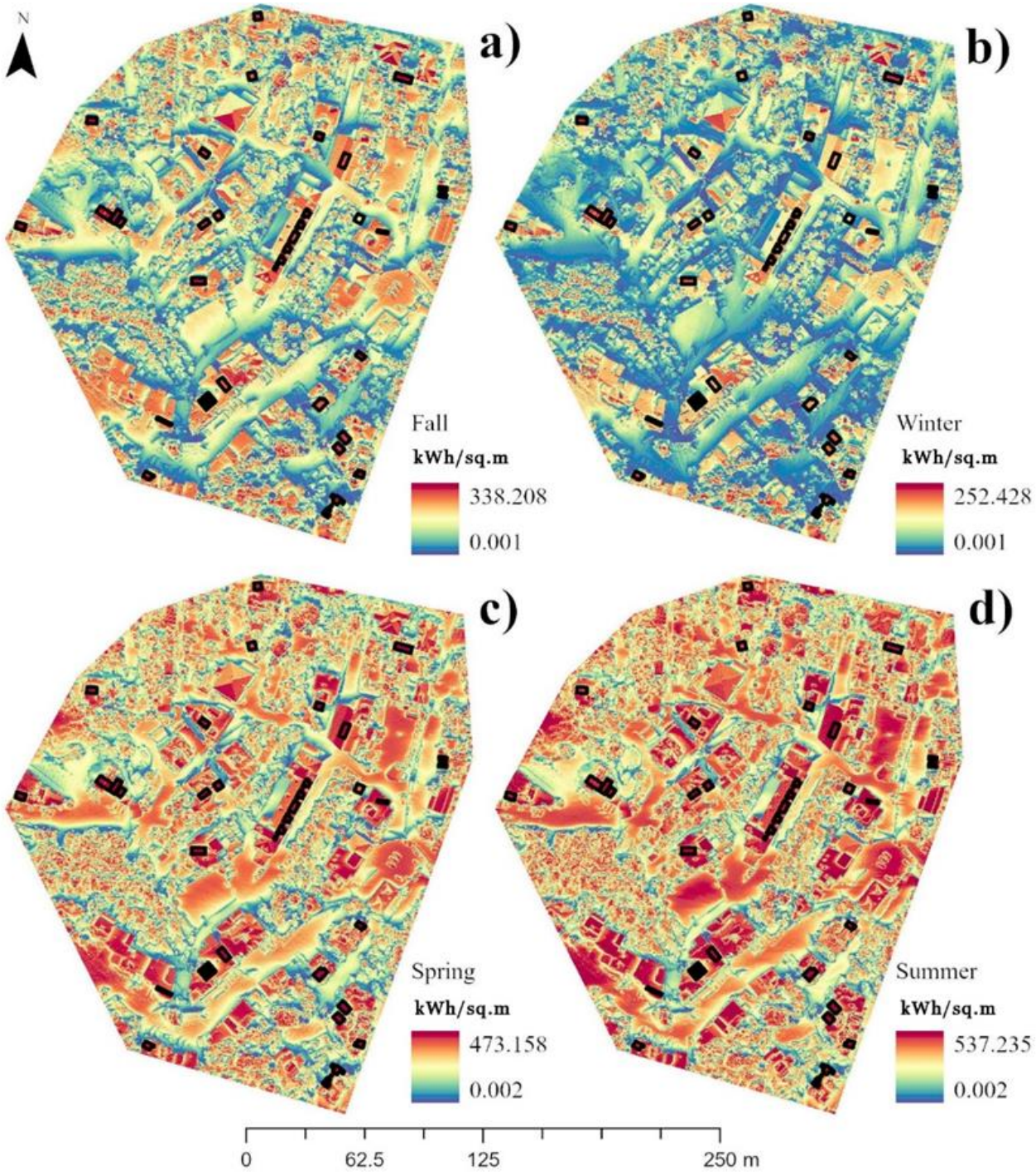

Figure 3. Seasonal solar radiation, a) Fall, b) Winter, c) Spring, and d) Summer.

The geometry of the PV solar panel units is defined by the area they cover, their orientation angle regarding the North direction (measured in degrees), and the slope of the installed panels (also in degrees).

The areas of the PV unit solar panels vary, ranging from 1.5 m^2 to 32.7 m^2. More than 20 PV solar panels among the 40 units under study have areas exceeding 20 m^2.

Figure 4 provides insights into the seasonal characteristics of the solar panels as determined by this study. These include the mean solar radiation (SR), the mean solar duration in hours, and the solar unit power (UP) measured in kWh.

Determining the optimal placement for photovoltaic (PV) panels involves a multitude of factors, encompassing geographical location, climate, available space, and the specific objectives of the PV system. The key considerations of the most suitable orientation for PV placement are listed in Table 1:

Table 1. Factors affecting the optimal PV panel orientations.

Factors	Affections
Solar Angle and Latitude	The angle of the sun and the latitude of the location affect the optimal panel orientation.
Direction	The cardinal direction (north, south, east, west) affects the exposure of the panels to sunlight.
Tilt Angle	The tilt angle of the panels can affect their efficacy in capturing sunlight.
Shading	Avoiding shading from nearby structures or vegetation is crucial to maximize energy production.
Energy Consumption Patterns	Aligning panel production with peak energy consumption times can optimize system performance.
Climate	Weather patterns, temperature, and cloud cover influence panel orientation choices.
Economic Factors	The costs associated with installations and potential energy savings play a role in orientation decisions.

In our study area, the PV panel units were installed with roof-oriented panels numbered 28, 29, 30, 31, 32, and 33. These panels are predominantly oriented to the South and Southwest, depending on installation feasibility.

PV panels with high Solar Radiation (SR) values are oriented between 180 and 233 degrees, corresponding to the south and southwest directions. However, the orientations associated with high Solar Duration (SD) values differ across seasons. In the fall season, the interval is between 228 and 231 degrees, in winter it's 227 to 233 degrees, in spring the high SD values are achieved with orientations between 180 and 195 degrees (toward the south), and in summer, when solar rays directly strike the ground, the interval tends towards the southwest (225-231 degrees).

The average slope of the installed PV unit solar panels with high SR values shows distinct patterns across seasons. Specifically:

Fall and Winter: Panels with high SR values have an average slope of 26 to 34 degrees.

Spring: High SR panels display an average slope ranging from 22 to 24 degrees.

Summer: Panels with low slope angles, typically between 6 and 16 degrees, attain higher SR values due to the direct solar rays striking the ground.

Interestingly, the PV units of solar panels that exhibit high SR values for the fall and winter seasons remain relatively consistent for spring and summer. However, the summer season introduces a shift in high SR values, where the panels that receive the most direct solar rays, such as panels numbered 14, 15, 16, and 24, achieve the highest SR values. This adjustment is noteworthy as these panels differ from those with high SR values in fall and winter (panels numbered 1, 23, 35, and 37). The result is a noticeable increase in SR values for panels 14, 15, 16, and 24 during the summer season.

In Figure 2, small areas housing PV solar panels 14, 15, and 16 exhibit high SR (Solar Radiation) values. These panels are on the same rooftop and share identical orientations with PV solar panel number 13. However, they are positioned at an elevated level and possess a slightly smaller inclination angle within the range of 6 degrees. Conversely, PV solar panels with a steeper inclination angle of 15.8 degrees (as stated in Figure 2) capture comparatively less solar radiation.

This observation highlights that PV solar panel units with lower inclinations (specifically, panels 14, 15, and 16) experience greater solar radiation across all seasons.

During the summer season, PV units of solar panels numbered 14, 15, 16, and 26 experience the highest Solar Duration, with 12 hours of sunlight each day. But in the winter season, the PV unit solar panel numbered 34 records the lowest solar duration of 3 hours per day Figure 4. This lower value in winter can be attributed to panel 34's location, in a lower area surrounded by taller buildings that cast shadows.

When considering the combination of high-power capacity and large panel areas (ranging from 25 to 32 m^2), panels numbered 3, 26, 36, and 38 stand out. In the summer season, these panels exhibit capacities between 509 and 517 kWh/m^2. Conversely, PV units of solar panels with high SR values and smaller areas, specifically panels numbered 14, 15, and 16, achieve a slightly higher capacity of 533 kWh/m^2 during the same season.

To confirm the accuracy of the acquired results for the Summer UP (Unit Power) during the season, data was collected on the 15th of August at noon. This data involved the solar power readings extracted from the inverters of specific PV solar panels, namely numbers 4, 8, 13, 24, and 38 as illustrated in Figure 5. The solar power produced by these inverters correlates with the Summer UP values of the respective PV solar panels. These values are arranged in ascending order: 8, 24, 4, 13, and 38. This identical order also aligns with the arrangement of UP values. These consistent findings validate the relationship between solar power production, utilization performance, and the specific characteristics of the mentioned PV solar panels.

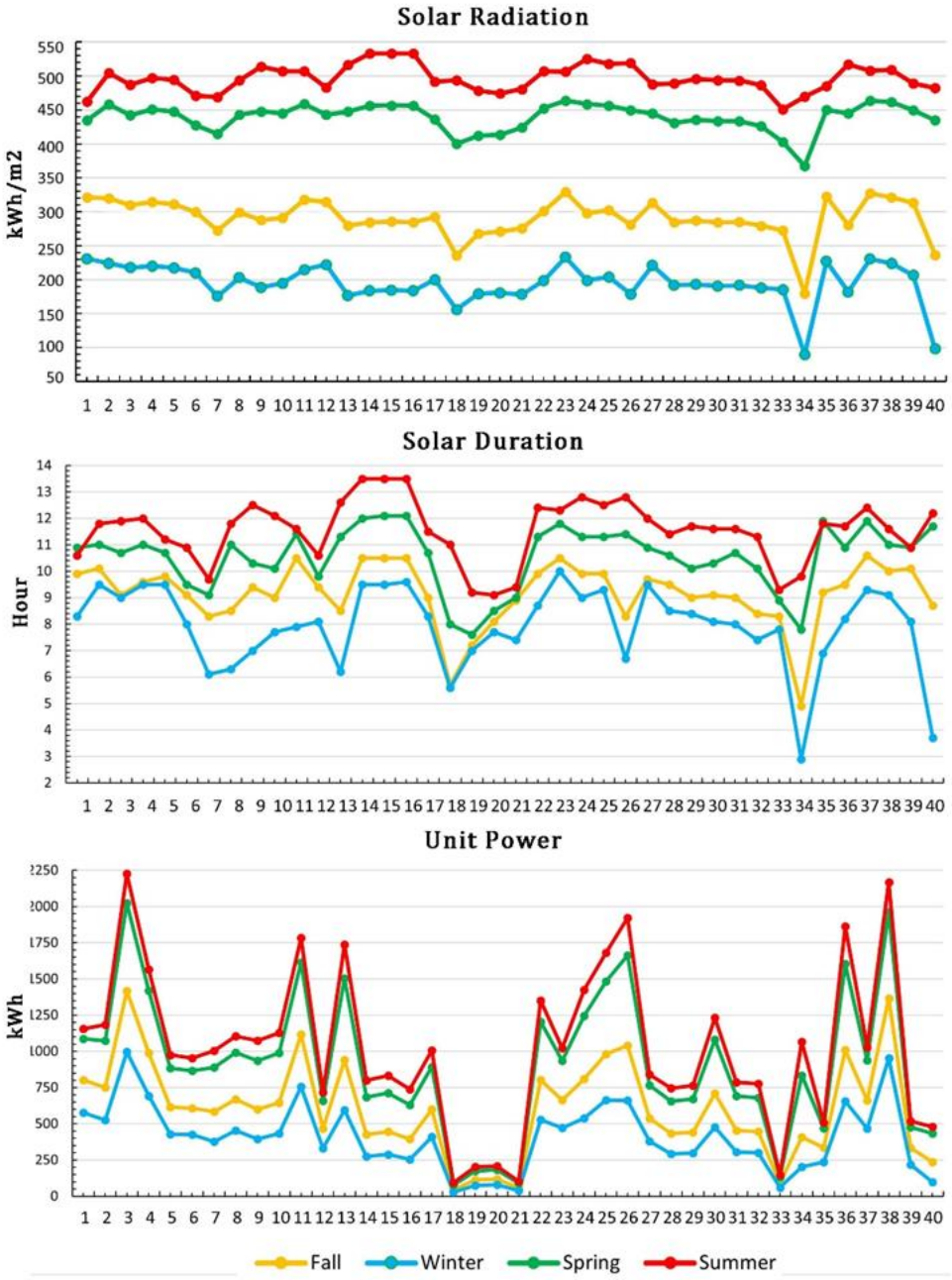

Figure 4. The season mean Solar radiation, mean solar duration and the unit power of the 40 photovoltaic units.

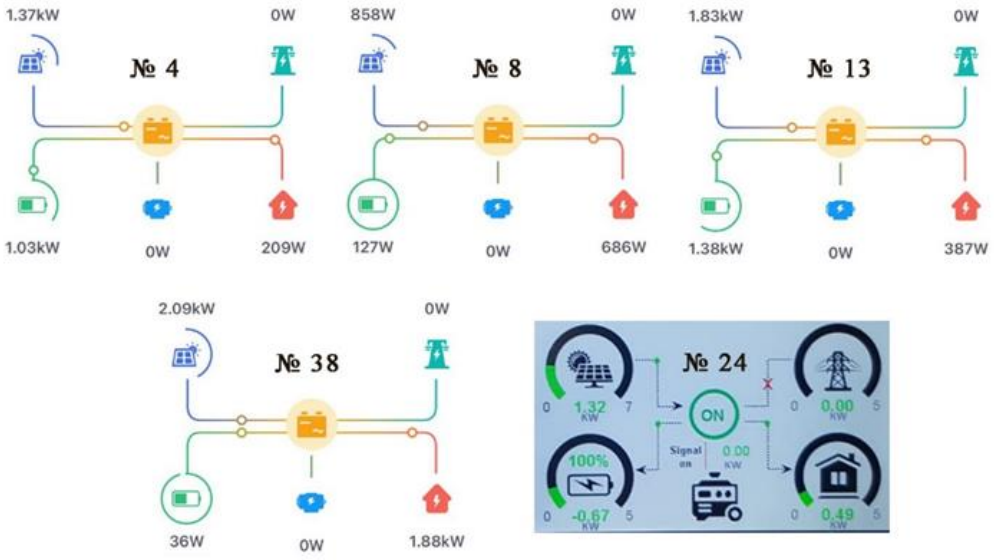

Figure 5. Solar power of the inverters of the PV Solar panels number 4,8,13,24 and 38.

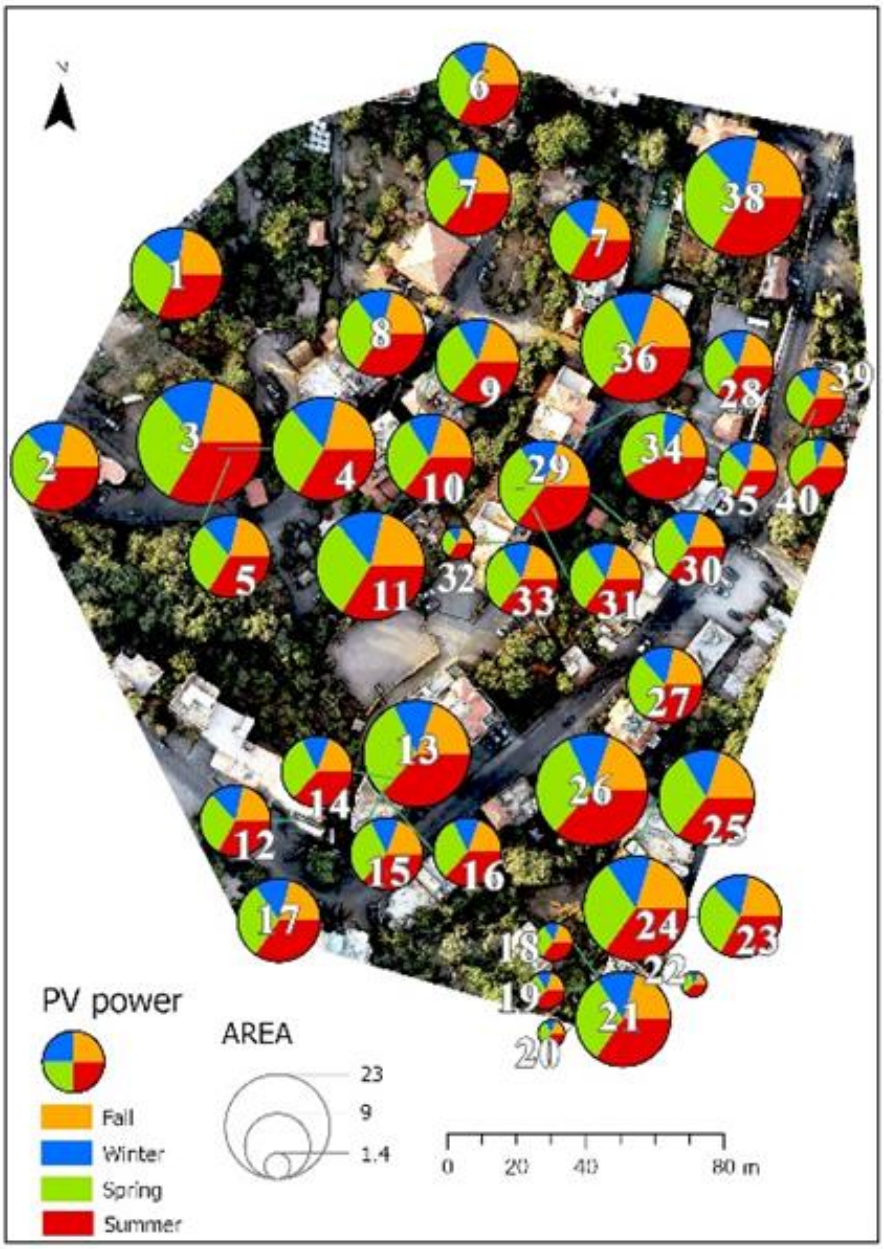

Figure 6. Bivariable map of seasonal PV solar unit power and area.

The bivariate map (Figure 6) showcasing Solar Power and Unit Area illustrates the seasonal solar power for each unit alongside the corresponding panel area. An evident pattern emerges wherein the solar power across all units and seasons—Fall, Winter, Spring, and Summer—is directly proportional to the unit's solar panel count and their respective areas. A notable example of this trend is observed with units numbered 38 and 3.

To gain a deeper comprehension of the relationships between PV units of solar panels within the study area, with a focus on seasonal power variations, the Agglomerative Hierarchical Clustering (AHC) technique was employed. This method, put forth by [22], facilitates the clustering of similar PV units based on their characteristics.

The Agglomerative Hierarchical Clustering (AHC) algorithm treats each PV unit's seasonal power values as a distinct cluster. It then calculates the similarity or dissimilarity between every pair of PV units utilizing the Euclidean distance metric.

In Figure 7 of the dendrogram, the vertical axis measures the dissimilarity or distance between clusters, providing insights into the relationships and groupings among clusters.

This involves identifying the proximity between clusters and merging the closest clusters based on the selected similarity metric. The process continues as the algorithm recomputes the similarity between the new clusters, ultimately generating an output comprising four distinct clusters, labeled as Moderate, High, Low, and Very Low solar power, as depicted in Table 2 which answers the study question.

How can PV solar panels be categorized based on their efficacy?

During this merging process, the AHC algorithm constructs a hierarchical structure of clusters, visually represented as a dendrogram. In this dendrogram, each leaf node corresponds to an individual PV unit, while the branches symbolize the evolving clustering hierarchy. This visual representation is presented in Figure 7.

Table 2 shows the four clusters' centroid values (average) of PV units' solar power in the four seasons. The first cluster C1 englobe all the PV units of moderate power, C2 cluster contains the high efficacy of solar power PV units.

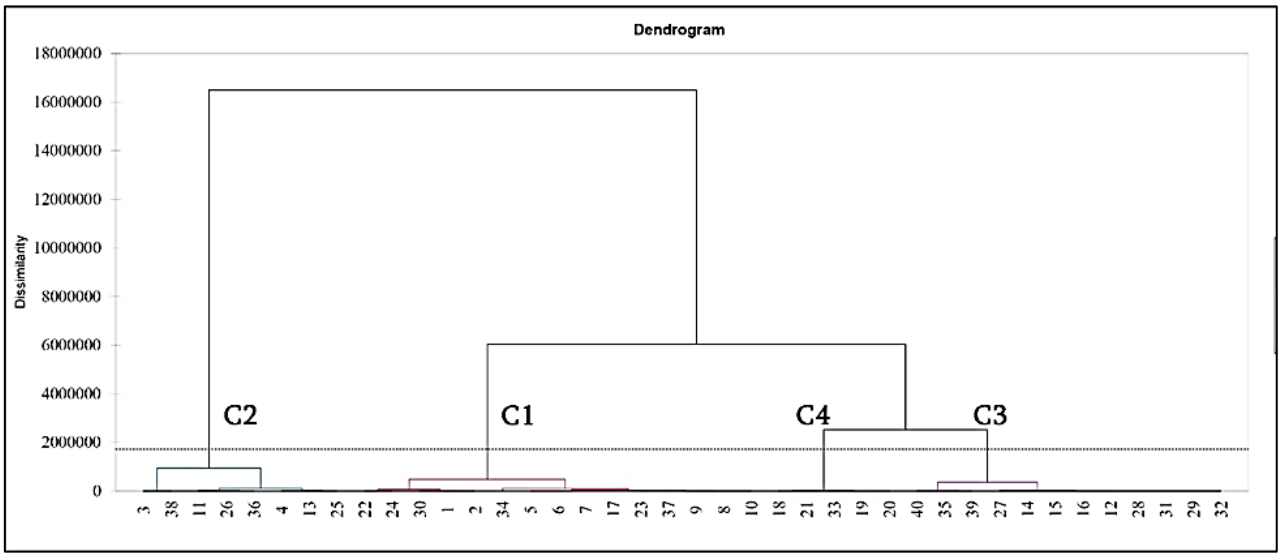

Figure 7. Dendrogram of the PV units clustering.

Table 2. Cluster centroid of PV solar panels based on solar power.

Cluster	PV №	Fall	Winter	Spring	Summer	Efficacy
C1	1,2,5,6,7,8,9,10,17,22,23,24,30,34,37	661.696	447.039	989.746	1113.559	Moderate
C2	3,4,11,13,25,26,36,38	1107.480	746.292	1659.153	1868.114	High
C3	12,14,15,16,27,28,29,31,32,35,39,40	412.772	273.003	627.339	708.448	Low
C4	18,19,20,21,33	84.765	56.542	130.570	150.578	Very low

The four clusters, namely C1, C2, C3, and C4, encompass PV solar panels that exhibit similar solar power levels across all seasons.

Cluster C2 comprises high-efficiency solar panels, with their performance influenced by factors such as installation position, orientation, and the number of panels (area). Cluster C4 includes panels with very low solar power output, suggesting that they do not yield the desired energy generation results. It is advisable to consider relocating these panels to enhance their productivity.

The productivity of solar panels within clusters C2 and C4 remains reasonable despite their fixed positions on the rooftops. This implies that, even in their current locations, these panels contribute a certain level of energy output.

To address the second research question, the PV units displaying elevated solar radiation and power possess specific geometrical and solar attributes. The most effective PV solar panels within the study area are those oriented between 195 and 225 degrees. These panels are positioned at a shallow inclination angle of 6 degrees and encompass a larger surface area or a greater number of individual panels. These factors collectively contribute to their enhanced performance in capturing solar radiation and generating power.

4. Conclusion

In a world grappling with energy crises and environmental concerns, solar photovoltaic (PV) panels have emerged as a promising solution. This study presents a comprehensive analysis of the capacity and efficacy of rooftop-installed PV solar panels within the El Meten region of Lebanon. Through integrating geospatial technologies like drone-based photogrammetry for DSM generation and GIS, a thorough examination of geometric and solar characteristics, seasonal solar radiation, solar duration, and unit power was conducted for 40 PV units.

The research unveiled critical insights regarding optimal panel orientation, seasonal power variations, and the clustering of panels based on their solar power efficacy. The Agglomerative Hierarchical Clustering (AHC) algorithm facilitated the categorization of panels into four distinct clusters: moderate, high, low, and very low solar power outputs. This clustering approach aids in identifying panels contributing efficiently to energy generation, those with potential for improvement, and those that may require reevaluation or relocation.

The study's outcomes offer valuable guidance for future solar installations in the region, enabling informed decisions on panel positioning, orientation, and efficacy optimization. As solar energy gains momentum as a sustainable power source, the findings of this study contribute to the ongoing dialogue on maximizing energy generation while reducing reliance on conventional fossil fuels. By harnessing the power of geospatial technologies and data-driven analysis, the research not only advances the understanding of rooftop solar panel efficacy but also promotes the broader adoption of renewable energy solutions to address pressing global energy challenges.

Acknowledgement

We would like to express our sincere gratitude to the Geospatial Lab of the Faculty of Letters and Human Sciences at the Lebanese University for their invaluable assistance during the execution of this experiment. Their expertise and resources have been instrumental in the successful completion of our research. We extend our appreciation to the entire team at the Geospatial Lab for their support and collaboration throughout this endeavor.

Conflicts of interest

The authors declare no conflicts of interest.

References

1. Milbrandt, A. R., Heimiller, D. M., & Schwabe, P. D. (2018). Techno-economic renewable energy potential on tribal lands. National Renewable Energy Laboratory, NREL/TP-6A20-70807. https://doi.org/10.2172/1459502
2. Charabi, Y., & Gastli, A. (2011). PV site suitability analysis using GIS-based spatial fuzzy multi-criteria evaluation. Renewable Energy, 36(9), 2554-2561. https://doi.org/10.1016/j.renene.2010.10.037
3. Gerbo, A., Suryabhagavan, K. V., & Kumar Raghuvanshi, T. (2022). GIS-based approach for modeling grid-connected solar power potential sites: a case study of East Shewa Zone, Ethiopia. Geology, Ecology, and Landscapes, 6(3), 159-173. https://doi.org/10.1080/24749508.2020.1809059
4. Strzalka, A., Alam, N., Duminil, E., Coors, V., & Eicker, U. (2012). Large scale integration of photovoltaics in cities. Applied Energy, 93, 413-421. https://doi.org/10.1016/j.apenergy.2011.12.033
5. Chaves, A., Bahill, A. T. (2010). Locating sites for photovoltaic solar panels pilot study uses DEM derived from LiDAR. ArcUser Fall 2010, 24-27
6. ESMAP. (2020). Global photovoltaic power potential by country. Washington, DC: World Bank
7. Šúri, M., Huld, T. A., Dunlop, E. D., & Ossenbrink, H. A. (2007). Potential of solar electricity generation in the European Union member states and candidate countries. Solar Energy, 81(10), 1295-1305. https://doi.org/10.1016/j.solener.2006.12.007
8. Choi, Y., Suh, J., & Kim, S. M. (2019). GIS-based solar radiation mapping, site evaluation, and potential assessment: A review. Applied Sciences, 9(9), 1960. https://doi.org/10.3390/app9091960
9. Clifton, J., & Boruff, B. (2010). Site options for concentrated solar power generation in the Wheatbelt. Wheatbelt Development Commission.
10. An, Y., Chen, T., Shi, L., Heng, C. K., & Fan, J. (2023). Solar energy potential using GIS-based urban residential environmental data: A case study of Shenzhen, China. Sustainable Cities and Society, 93, 104547. https://doi.org/10.1016/j.scs.2023.104547
11. Sun, Y. W., Hof, A., Wang, R., Liu, J., Lin, Y. J., & Yang, D. W. (2013). GIS-based approach for potential analysis of solar PV generation at the regional scale: A case study of Fujian Province. Energy Policy, 58, 248-259. https://doi.org/10.1016/j.enpol.2013.03.002
12. Charabi, Y., & Gastli, A. (2010). GIS assessment of large CSP plant in Duqum, Oman. Renewable and Sustainable Energy Reviews, 14(2), 835-841. https://doi.org/10.1016/j.rser.2009.08.019
13. Lara, E. G., & Garcia, F. S. (2021). Review on viability and implementation of residential PV-battery systems: Considering the case of Dominican Republic. Energy Reports, 7, 8868-8899. https://doi.org/10.1016/j.egyr.2021.11.208
14. Ramadhan, M., & Naseeb, A. (2011). The cost benefit analysis of implementing photovoltaic solar system in the state of Kuwait. Renewable Energy, 36(4), 1272-1276. https://doi.org/10.1016/j.renene.2010.10.004
15. Böhner, J., & Antonić, O. (2009). Land-surface parameters specific to topo-climatology. Developments in Soil Science, 33, 195-226. https://doi.org/10.1016/S0166-2481(08)00008-1
16. Dubayah, R., & Rich, P. M. (1996). GIS-based solar radiation modeling. GIS and Environmental Modeling: Progress and Research Issues, 129-134.
17. Global Solar Atlas 2.0, Solaris database version 2.1. https://solargis.com/maps-and-gis-data/download/lebanon
18. Mulherin, A. (2011). A spatial approach to determine solar PV potential for Durham homeowners. [Master's Thesis, Duke University].
19. Carrión, J. A., Estrella, A. E., Dols, F. A., Toro, M. Z., Rodríguez, M., & Ridao, A. R. (2008). Environmental decision-support systems for evaluating the carrying capacity of land areas: Optimal site selection for grid-connected photovoltaic power plants. Renewable and Sustainable Energy Reviews, 12(9), 2358-2380. https://doi.org/10.1016/j.rser.2007.06.011
20. Reijenga, T., & Ruoss, D. (2005). Technologies and integration concepts. Designing with solar power: a source book for building integrated photovoltaics, 22-52.
21. NREL (2022). 2022 Annual Technology Baseline. Golden, CO: National Renewable Energy Laboratory. https://atb.nrel.gov/electricity/2022/commercial_pv
22. Kaufman, L., & Rousseeuw, P. J. (1990). Finding groups in data: An introduction to cluster analysis. Wiley, New Jersey.

Mersin Photogrammetry Journal
https://dergipark.org.tr/en/pub/mephoj
e-ISSN 2687-654X

3D reconstruction of foot metatarsal bones of women using CT images

Hatice Çatal Reis *[1]

[1] Gümüşhane University, Department of Geomatics Engineering, Türkiye, hcatal@gumushane.edu.tr

Cite this study: Reis, H. Ç. (2024). 3D reconstruction of foot metatarsal bones of women using CT images. Mersin Photogrammetry Journal, 6 (1), 32-38

https://doi.org/10.53093/mephoj.1435928

Keywords
Metatarsal
CT-scan images
Medical photogrammetry
3D reconstruction
Medical image processing

Research Article

Received:12.02.2024
Revised: 10.03.2024
Accepted: 14.03.2024
Published:16.03.2024

Abstract

Bone morphology is a fundamental factor in human anatomy. However, foot and ankle bones have yet to be adequately evaluated in 3-dimensional. It is essential to present the biometric data of anatomical structures. This study formed 3D models of the metatarsal bones of the feet of young women using image processing techniques to examine biometric measurements and determine morphology on these 3D models. This study investigated bone lengths in the metatarsal bones of women feet in Türkiye. A total of ten young female subjects were included as the test group to measure the lengths of their foot metatarsal bones using CT (Computed Tomography) scans, and 20 feet (left/right) were examined. The parameters that were used for the analyses were detector collimation of 64x0.5 mm, section thickness of 0.5 mm, current of 100 mA, tube voltage of 120 kVp, and pixel spacing of 512x512 pixels with a monochrome resolution providing 16-bit gray levels. CT images were processed, and a 3D metatarsal reconstruction was gathered. Then, the biometric measurements were calculated on this 3D model. For the lengths of the volunteers' right/left foot metatarsal bones, statistically significant differences were calculated using a one-sample t-test. For the female metatarsal bones of the left and right feet, statistically significant differences in length were calculated on 3D models. The mean results of the metatarsal length measurements were MT1(metatarsal): 59.52±1.42 mm, MT2: 70.45±1.82 mm, MT3: 66.25±1.82 mm, MT4: 65.12±1.81 mm and MT5: 63.63±1.81 mm. The level of statistical significance was accepted as $p < 0.05$ for the one-sample t-test conducted for each metatarsal bone. The lengths of the right foot metatarsal bones were different from those of the left foot metatarsal bones in the sample. However, this difference was approximately one-tenth of a millimeter. The shortest bone was MT1, and the longest bone was MT2. These measurements are consistent with the anatomical information in the literature. The 3D models from the CT images and the biometric measurements of the metatarsal bones were found to be reliable and accurate.

1. Introduction

Medical photogrammetry has been used for decades to measure, model, or provide metric data on various parts of the body. Medical photogrammetry uses medical images to produce this data/information. Computer Tomography images of women's foot metatarsal bones have been used in this research. According to the Turkish Statistical Institute, the female population in Türkiye was 49.8% of the total population in 2018, and nearly 6.344 million of women were considered as young women. Metatarsal fractures are the most common foot injuries investigated in the literature [1-4], and, according to the reports, fractures between 67 and 75.4/100,000 per year [5]. Approximately 40% of injury patterns in dancers are observed in the lower leg, foot, and ankle [6]. The metatarsal bones of the human foot consist of five bone units, and metatarsal fractures in dancers' feet are usually seen in the second and fifth bones [7]. These dancers' bones are usually broken when they miss a step or are in a point state [8]. In some cases, it becomes challenging for doctors to determine stress fractures [9,10]. The9% of metatarsal fractures occur in athletes and sports [4]. Additionally, metatarsals are important in hallux valgus, which has a negative impact on gait mechanics [11]. The best treatment for this condition is still challenging [12]. The effect of the first metatarsal osteotomy on the midfoot bones in patients with hallux valgus was investigated [13]. What should be considered here is the ability to accurately detect any fracture, deformation, or anomaly through early diagnosis and treatment. It is of vital that athletes, dancers, or people can quickly return to their daily routines such as, sport, and dancing. Metatarsal researches are rarely studied in the current literature, generally focusing on treatment recommendations [5]. Comprehensive research for the

metatarsal bones is necessity [14]. 3D modelling provides an essential opportunity for overcoming such difficulties. With the assistance of various programs developed in recent years, 3D images are generated from instant 2D images, which are taken as intersections of parallel fields along relevant objects such as feet covered in this research. It is possible to use 3D modeling software for vector-based 3D geometric modeling, which conforms to the definition of tissue-bound geometry beyond the 3D display of tissues [15-17]. Researchers are developing various modelling methods, such as the repeatable kinematic multi–segment model [18]. In the literature, several techniques for 3D bone measurements have been introduced, allowing area, volume, surface, distance, and angular measurements of 3D models generated from CT or MRI images [18-21]. A study investigated bone morphology by creating a 3D model of rare foot disorders using MRI images [22]. Computer-aided design (CAD) [23] and Computer-assisted tomography (CAT), diagnosis [24], pre-operative planning, surgical navigation, and surgical processes have been used in the surgical management of such cases. CAD has supported detection and can improve the diagnosis for radiologists [25]. CT devices have been known as the best technique for bone imaging since the 1970s. With its resolution and 3D capability, the CAT scan images substantially revolutionized the medicine area. A series of CAT sectional images are obtained by moving the CT device vertically in the longitudinal direction. The device takes these images in large quantities depending on the resolution of the 3D longitudinal scan. Sections are then generated to form a 3D model [26]. Multi-detector Computed Tomography (MDCT) images may be used to design the subtalar prostheses and analyse surgical procedures of the ankle and the hindfoot [27]. 3D CT images of the bones create surface meshes, and bone angles are measured [19]. The creation and evaluation of 3D models for morphological calculations of human bones still need to be sufficiently done. There is still a need for new research and studies in this field. In this experimental research, after obtaining the 3D models of the women's metatarsal foot bones, the biometric measurements were taken, and deformations became detectable using image processing techniques.

The 3D models formed in this study were created using CT images. 3D rendering of metatarsals was used to diagnose disorders and to make morphological measurements of the metatarsal bones.

After reviewing the recent literature, we found a few pieces of research about the foot that employ biomedical measurements. Previous studies have usually focused on the shape and characteristics of the foot [28-31]. The study [21] designed a method for 3D morphological measurements of the normal calcaneus based on CT image processing techniques. Another study presented a semi-automatic segmentation approach for biometric measurement of the talus bone using CT images [32]. This study aimed to introduce a method for 3D morphological measurements of the metatarsal bones based on CT pre/post-processing techniques and measure biometric parameters in a female case. The research provides information about biometric measurements of the metatarsal bones of young women in Türkiye. This research constructed 3D models of the metatarsal bones of healthy female volunteers. The method studied here is expected to speed detection of the diagnosis and treatment in different medical fields, such as orthopedics, surgery, anatomy, sports medicine, and veterinary medicine. Thus, medical standards may be reachable, and repeatable measurements may be taken confidingly. 3D models provide a general and computationally efficient solution for biometric measurements and are suitable for the real-time modelling. Moreover, this study may provide a helpful information for developing foot—and ankle-related products or improving orthopedic footwear design for women and men. Additionally, for educational purposes, 3D bone modelling techniques may be used in anatomy classes and physical training at colleges.

2. Material and Method

This study employed 3D models of the metatarsal foot bones of Turkish women born in 1992 for the analysis of differences between the left and right foot using digital image processing techniques. MDCT images of 20 feet were examined and about 12000 CT images were processed. The general demographic data of the subjects were investigated, and the sample's mean age was 18, their mean shoe size was 37±1.2, their mean height was 165±8 cm, and their mean weight was 49.8±4.2 kg.

2.1. CT scans and image processing

During the scanning process, the health of the volunteers was considered as top priority of this study. This study was therefore carried out by paying a great attention to the standards of the existing procedures of the Declaration of Helsinki [33] and the Turkish Society of Radiology Computed Tomography Regulation [34] in accordance with the Clinical Research Ethics Committee documents (Decision No. 004,08/01/2010) to avoid the negative impacts on the volunteers participated in this study.

The participants were carefully selected from among those with no orthopedic disorders or a history of orthopedic disorders and women with no history of professional dancing or sports. The axial CT images of the volunteers were taken, and the metatarsal bones of the right and left feet were tested. A total of 20 feet were analysed in the study. The doses of radiation were adjusted within the allowed range, with respect to the scan parameters that do not harm the volunteers' health, and these experiments were conducted under experienced radiologist supervision. Additional parameters were applied to reduce the dose even further. The participants' feet were scanned side by side or separately using the CT device. The same image and scanning parameters were used for all the scanning process. To increase the accuracy of each image obtained by the MDCT device, the feet of the volunteers were fixed to the table to keep them still. The scans were carried out by high-resolution CT (Toshiba Aquillon, America Medical Systems). The parameters were 64x0.5 mm - 4x0.5 mm for detector collimation, 0.5 mm for section thickness, 100 mA of current, a tube voltage of 120 kVp, a matrix of 512x512 pixels for pixel spacing, and 16-bit

grey levels for monochrome resolution. When scanning the CT images, great attention was paid to getting the images with a minimal, harmless dose of radiation but with high resolution. Cross-section images were acquired and stored in the Digital Imaging and Communications in Medicine (DICM) format and then imported into the computer environment with a 3D analysis software called "3D-Doctor". Following this, 3D models were generated. The model's geometry was obtained from 3D reconstruction of the CT images of healthy female volunteers' left and right feet. These 3D models of the women's metatarsal bones were used for the biometric measurements.

All measurements were taken separately for the right and left feet. The 3D reconstructions of the metatarsal bones and the biometric measurements were calculated using the 3D-Doctor. $p<0.05$ was considered as critical value for statistical significance.

2.2. 3D Modelling

Two different techniques are usually performed for displaying 3D data. These are the volume and surface rendering techniques. In surface rendering, objects with a smooth geometry are expressed by the continuous functions. An exact function cannot define objects with non-specific geometry; instead, these surfaces are expressed as the definitions of small surface elements [35]. In volume rendering, the voxel values are determined by monitoring the rays passing through each voxel throughout the volume, or voxels on the object are processed by back-to-front or reverse transactions [35]. The axial images in the .dcm format were first imported to a computer with 3D modeling software, and calibration was automatically performed by the software. While processing the images, a median filter was applied to remove the spot or line noise in the CT images. The bone and non-bone materials were defined in each CT slice as Hounsfield Units. Hounsfield unit is determined as variable values between 32900-40000. Segmentation was performed to classify the pixels showing the same characteristics on the MDCT images. To create a surface model, object boundaries must be identified. This study utilized the region-growing segmentation method. The Hounsfield scale was also used for the interactive segmentation (Figure 1).

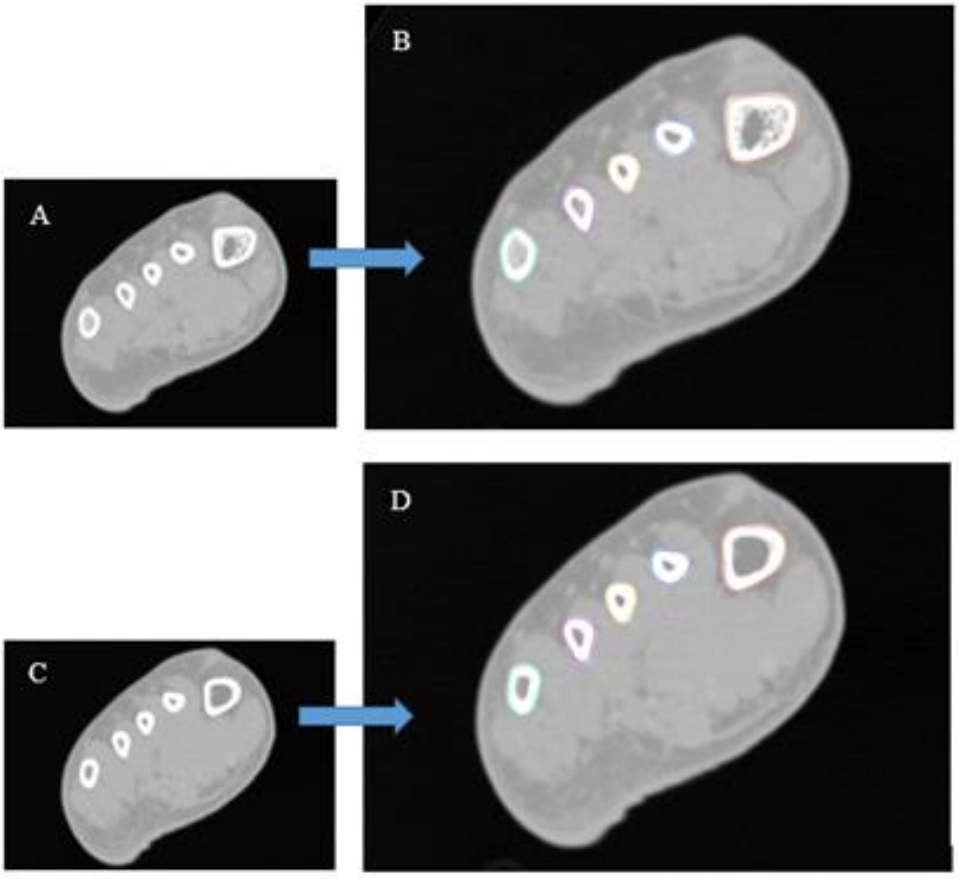

Figure 1. Demonstration of segmentation result of raw slices.

*A/C: raw CT slices, B/D: an interactive and automatic segmentation technique was applied to distinguish all components of the metatarsal bones.

The 3D structures of each metatarsal bone were reconstructed by shaded surface display (SSD) with a reconstruction. With the assistance of the perspective icon of SSD reconstruction, the defined boundary of the surface could be observed. Then, the metatarsal bone was generated and detected (Figure 2). Each length was calculated by the software (yellow line) (Figure 2).

Thus, the 3D models of the metatarsal bones were then generated individually as separate models in separate layers (Figure 3).

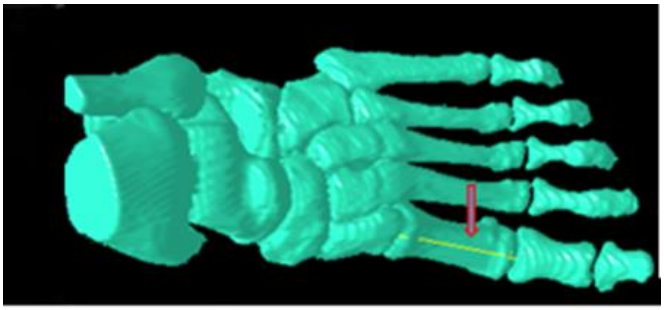

Figure 2. 3D-reconstructed images of the metatarsal bones in a woman foot and biometric measurement.

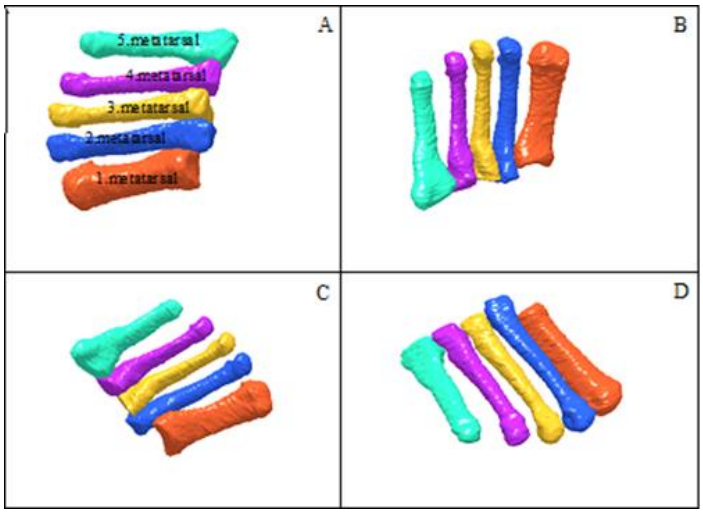

Figure 3. Reconstruction of 3D metatarsal bones.

*A/D: After the segmentation, the SSD reconstruction image of the 3D metatarsals presented the anterior. B/C: Posterior view of 3D model Biometric measurements were made on these models, and calculations were carried out using these measurements. The 3D measurement process was carried out as follows (Figure 4):

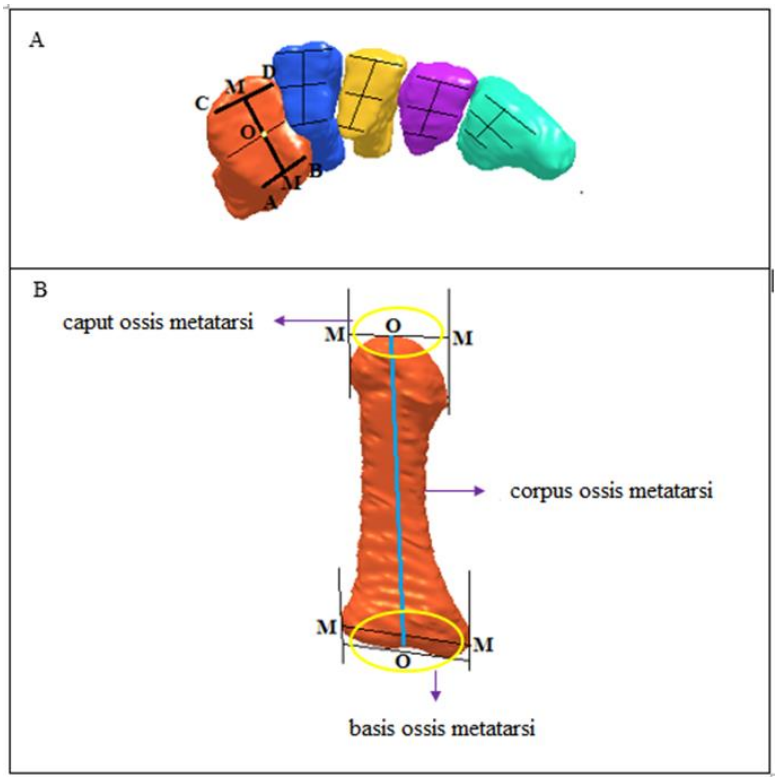

Figure 4. Three-dimensional morphological measurements of metatarsal bones.

Lengths from the caput ossis metatarsi to the basis ossis metatarsi were calculated. 4a, the length of M: the midpoint between A and B/ C and D, Figure 4a-4b, the height of the O: distance between M_1 and $M_2/2$.

2.3. Statistical analysis

The research methods include a qualitative analysis and quantitative measurement. Statistical analyses were performed in MATLAB. One-sample t-test was used to determine whether a sample from a population with a specific mean. Therefore, the mean length of the metatarsals of women were not always known, but sometimes hypothesised. The one-sample t-test for the non-parametric samples was applied to determine whether or not there were significant differences in the metatarsal bones' lengths in young women in Türkiye. $p<0.05$ was considered to be statistically significant for the one-sample t-test of each metatarsal bone. The alpha level was chosen as 5% (0.05) in the study. If the test result is a small p (≤ 0.05), this is strong evidence that the null hypothesis is invalid. If the test result is a large p (> 0.05), it means that the alternative hypothesis is weak, so the null hypothesis cannot be rejected. The mean parameters for all measurements for the lengths and the standard errors of mean (SEM) were calculated using the formulae below.

Arithmetic mean (Equation 1-2);

$$\bar{X} = \frac{X_1 + X_2 + \cdots X_n}{n} \quad (1)$$

$$\bar{X} = \frac{\sum X_i}{n} \quad (2)$$

i: 1, 2, 3

Standard deviation (Equation 3);

$$S = \sqrt{\frac{\sum (X_i - \bar{X})^2}{n}} \quad (3)$$

Standard error refers to the error of the sample mean (Equation 4).

$$SEM = \frac{S}{\sqrt{n}} \quad (4)$$

Sample mean is expressed with standard error (Equation 5-6).

$$\bar{X} + S_{\bar{X}} \quad (5)$$

$$Mean \pm SEM \quad (6)$$

One-sample t-test was performed (Equation 7).

$$t = \frac{X - m_0}{S_{\Delta_x}} \quad (7)$$

The bone lengths of the metatarsus-1, 2, 3, 4 and 5 were combined. The measurement value of each bone was obtained. The lengths of all bones in the right and left metatarsal bones in the sample were calculated. Their significance was examined in the one-sample t-test, and deformation analyses were thus performed. The same statistical processes were carried out for all the participants. The biometric values of the metatarsal bones in the left feet are given in Table 1.

Table 1. 3D biometrical parameters of metatarsal bones of the left foot.

Left foot	MT1 (mm)	MT2 (mm)	MT3 (mm)	MT4 (mm)	MT5 (mm)
1	53.68	65.78	61.88	59.24	63.16
2	58.98	69.41	62.38	61.95	57.76
3	54.68	66.98	62.58	60.04	64.56
4	59.58	69.99	63.08	62.25	58.36
5	58.96	66.98	63.19	63.10	58.00
6	60.36	73.27	68.32	66.98	66.93
7	61.12	72.93	65.80	66.59	65.94
8	63.00	75.68	71.47	69.75	67.37
9	62.43	75.89	73.86	71.36	68.96
10	62.33	72.54	67.94	67.68	64.79
mean	59.51	70.95	66.05	64.89	63.58

*MT1: metatarsal 1, MT2: metatarsal 2, MT3: metatarsal 3, MT4: metatarsal 4, MT5: metatarsal 5. The biometric values of the metatarsal bones in the right foot are given in Table 2. Table 2. 3D biometrical parameters of the metatarsal bones in the right foot.

Table 2. 3D biometrical parameters of metatarsal bones of the right foot.

Right foot	MT1 (mm)	MT2 (mm)	MT3 (mm)	MT4 (mm)	MT5 (mm)
1	53.69	63.92	63.92	61.32	62.01
2	59.02	67.12	62.01	62.00	60.37
3	54.99	65.82	64.92	62.32	63.01
4	59.99	68.12	63.23	62.00	60.69
5	58.58	65.47	63.35	62.25	56.75
6	60.76	73.61	68.46	67.92	66.87
7	61.12	72.93	65.80	66.59	65.94
8	63.01	75.06	71.17	70.32	67.50
9	62.15	75.22	73.47	71.06	68.70
10	61.99	72.21	68.10	57.58	64.94
mean	59.53	69.95	66.44	65.34	63.68

3. Results

For the metatarsal bones of the female left and right feet, statistical differences were calculated for the length of the 3D models. When the left feet of the participants were evaluated, human subject 8 had the longest foot length in the first metatarsal, while human subject 1 had the shortest length. In the second metatarsal, the ninth human subject has the largest length, while the first has the smallest value. While the ninth human subject has the largest length in the third and fourth metatarsals, the first human subject has the smallest value. Subject 2 had the smallest length in the fifth metatarsal, while human subject 9 had the largest length. When evaluating the participants' right feet, human subject 8 had the longest foot length at the first metatarsal, while human subject 1 had the shortest foot length. In the second metatarsal, human subject 9 has the largest length, while human subject 1 has the smallest value. While subject 9 has the largest length in the third metatarsal, human subject 2 has the smallest value. While subject 9 has the largest length in the fourth metatarsals, human subject 1 has the smallest value. Subject 2 had the smallest length at the fifth metatarsal, while human subject 9 had the largest length. The metatarsal lengths were obtained as

following: MT1: 59.52±1.42 mm, MT2: 70.45±1.82 mm, MT3: 66.25±1.82 mm, MT4: 65.12±1.81 mm, MT5: 63.63±1.81 mm. The shortest bone was MT1, and the longest bone was MT2. The data adhered to a normal distribution. We used one-sample Kolmogorov-Smirnov test for MT1: 0.096, MT2: 0,115, MT3: 0.109, MT4: 0.05, MT5: 0.2. The basic null hypothesis was that the population mean was equal to a hypothesised value,

H_0: μ_0 = Hypothesised value.

The one-sample t-test results and technical details are presented in the following order:

$P_{m1}<0.999$, $P_{m2}<0.997$, $P_{m3}<0.997$, $P_{m4}<0.995$, $P_{m5}<1$

A statistically significant difference was observed based on normal distribution.

4. Conclusion

Medical photogrammetry is applied in the measurements and calculations of many organs. This research focused on the morphometry of the foot metatarsal bone using the medical photogrammetric technique. Metric values were produced and presented on the 3D models of the metatarsal bones. The metatarsal bones of women were examined in this study. While the length value of each people worldwide is unique, the foot anatomies of the two feet (left/right) are also different than each other. Right-foot metatarsal bones are longer than left-foot metatarsal bones. However, this difference is about one-tenth of a millimetre. The main reason for this difference may be that the volunteers have a right dominant side. The statistical and biometric measures on the right and left feet of the participants were performed and analysed in detail. The results of this study and the measurements were analysed unbiased. Medical professionals make calculations using an imaging network/database or by directly reaching the bone. The reliability of these measurements and calculations depends on the expert's experience and knowledge. Minimizing the negative impact of human activity is crucial in this process. The 3D morphological measurements based on CT image processing were highly reliable and repeatable for the anatomic and morphological measurements of the metatarsals. This technique will be helpful for the anatomic reduction of metatarsal fractures and anomalies. Hence, this study underlined that doctors may benefit from pre-generated 3D models for the diagnosis and treatment related to metatarsal bones in such cases. This study contributes to high-accuracy visualization in areas such as anthropology, sports and dance injuries, anatomical training, forensic identification, orthopedics, and surgery. The results may be extended and become transferable for the other cases by increasing the number of participants in further studies.

Acknowledgement

The author is grateful to Selcuk University, Scientific Research Project Coordination for their technical help (Project No: 10101011).

Conflicts of interest

The authors declare no conflicts of interest.

References

1. Spector, F. C., Karlin, J. M., Scurran, B. L., & Silvani, S. L. (1984). Lesser metatarsal fractures. Incidence, management, and review. Journal of the American Podiatric Medical Association, 74(6), 259-264. https://doi.org/10.7547/87507315-74-6-259
2. Polzer, H., Polzer, S., Mutschler, W., & Prall, W. C. (2012). Acute fractures to the proximal fifth metatarsal bone: development of classification and treatment recommendations based on the current evidence. Injury, 43(10), 1626-1632. https://doi.org/10.1016/j.injury.2012.03.010
3. Cakir, H., Van Vliet-Koppert, S. T., Van Lieshout, E. M. M., De Vries, M. R., Van Der Elst, M., & Schepers, T. (2011). Demographics and outcome of metatarsal fractures. Archives of orthopaedic and trauma surgery, 131, 241-245. https://doi.org/10.1007/s00402-010-1164-6
4. Beddard, L., Roslee, C., & Kelsall, N. (2024). Acute and stress fractures of the metatarsals in athletes. Orthopaedics and Trauma, 38(1), 46-50. https://doi.org/10.1016/j.mporth.2023.11.008
5. Herterich, V., Hofmann, L., Böcker, W., Polzer, H., & Baumbach, S. F. (2023). Acute, isolated fractures of the metatarsal bones: an epidemiologic study. Archives of Orthopaedic and Trauma Surgery, 143(4), 1939-1945. https://doi.org/10.1007/s00402-022-04396-3
6. Macintyre, J., & Joy, E. (2000). Foot and ankle injuries in dance. Clinics in Sports Medicine, 19(2), 351-368. https://doi.org/10.1016/S0278-5919(05)70208-8
7. Lee, H. A., Batley, M. G., Krakow, A., Buczek, M. J., Sarkar, S., Talwar, D., ... & Davidson, R. S. (2023). New Classification for Pediatric Proximal Fifth Metatarsal Fractures. The Journal of Foot and Ankle Surgery, 63(2), 267-274. https://doi.org/10.1053/j.jfas.2023.11.015
8. Prisk, V. R., O'Loughlin, P. F., & Kennedy, J. G. (2008). Forefoot injuries in dancers. Clinics in sports Medicine, 27(2), 305-320. https://doi.org/10.1016/j.csm.2007.12.005
9. Goulart, M., O'Malley, M. J., Hodgkins, C. W., & Charlton, T. P. (2008). Foot and ankle fractures in dancers. Clinics in sports medicine, 27(2), 295-304. https://doi.org/10.1016/j.csm.2008.01.002
10. Van Dijk, C. N., & Marti, R. K. (1999). Traumatic, post-traumatic and over-use injuries in ballet: with special emphasis on the foot and ankle. Foot and ankle surgery, 5(1), 1-8. https://doi.org/10.1046/j.1460-9584.1999.51122.x
11. Dygut, J., & Piwowar, M. (2022). Muscular Systems and Their Influence on Foot Arches and Toes Alignment—Towards the Proper Diagnosis and Treatment of Hallux Valgus. Diagnostics, 12(12), 2945. https://doi.org/10.3390/diagnostics12122945

12. Barg, A., Harmer, J. R., Presson, A. P., Zhang, C., Lackey, M., & Saltzman, C. L. (2018). Unfavorable outcomes following surgical treatment of hallux valgus deformity: a systematic literature review. JBJS, 100(18), 1563-1573. https://doi.org/10.2106/JBJS.17.00975
13. Cruz, E. P., Sanhudo, J. A. V., Iserhard, W. B., Eggers, E. K. M., Camargo, L. M., & de Freitas Spinelli, L. (2024). Midfoot width changes after first metatarsal osteotomy in hallux valgus surgery: a biomechanical effect?. The Foot, 102070. https://doi.org/10.1016/j.foot.2024.102070
14. Khurana, A., Alexander, B., Pitts, C., Brahmbhatt, A., Cage, B., Greco, E., ... & Shah, A. B. (2020). Predictors of malreduction in zone II and III Fifth metatarsal fractures fixed with an intramedullary screw. Foot & Ankle International, 41(12), 1537-1545. https://doi.org/10.1177/10711007209474
15. Černochová, P., Kaňovská, K., Kršek, P., & Krupa, P. (2005). Application of geometric biomodels for autotransplantation of impacted canines. World Journal of Orthodontics, 1.
16. Krupa, P., Kršek, P., Černochová, P., & Molitor, M. (2004). 3-D real modelling and CT biomodels application in facial surgery. In Neuroradiology. Berlin: European Society of Neuroradiology, 141, 1. ISBN 0028-3940.
17. Krupa, P., Krsek, P., Javorník, M., Dostál, O., Srnec, R., Usvald, D., ... & Necas, A. (2007). Use of 3D geometry modelling of osteochondrosis-like iatrogenic lesions as a template for press-and-fit scaffold seeded with mesenchymal stem cells. Physiological research, 56(1), 107-114. https://doi.org/10.33549/physiolres.931308
18. Stebbins, J., Harrington, M., Thompson, N., Zavatsky, A., Theologis, T., Repeatability of a model for measuring multi-segment foot kinematics in children. Gait & Posture 2006; 23:4- 401–410. https://doi.org/10.1016/j.gaitpost.2005.03.002
19. Gutekunst, D. J., Liu, L., Ju, T., Prior, F. W., & Sinacore, D. R. (2013). Reliability of clinically relevant 3D foot bone angles from quantitative computed tomography. Journal of foot and ankle research, 6, 1-9. https://doi.org/10.1186/1757-1146-6-38
20. Eckstein, F., Cicuttini, F., Raynauld, J. P., Waterton, J. C., & Peterfy, C. (2006). Magnetic resonance imaging (MRI) of articular cartilage in knee osteoarthritis (OA): morphological assessment. Osteoarthritis and cartilage, 14, 46-75. https://doi.org/10.1016/j.joca.2006.02.026
21. Qiang, M., Chen, Y., Zhang, K., Li, H., & Dai, H. (2014). Measurement of three-dimensional morphological characteristics of the calcaneus using CT image post-processing. Journal of foot and ankle research, 7, 1-9. https://doi.org/10.1186/1757-1146-7-19
22. Stindel, E., Udupa, J. K., Hirsch, B. E., Odhner, D., & Couture, C. (1999). 3D MR image analysis of the morphology of the rear foot: application to classification of bones. Computerized medical imaging and graphics, 23(2), 75-83. https://doi.org/10.1016/S0895-6111(98)00070-6
23. Mori, K., Hahn, H. K. (2019). Medical Imaging 2019: Computer-Aided Diagnosis, San Diego, California, United States, 16-21 February 2019. SPIE Proceedings 10950.
24. Park, H. J., Kim, S. M., La Yun, B., Jang, M., Kim, B., Jang, J. Y., ... & Lee, S. H. (2019). A computer-aided diagnosis system using artificial intelligence for the diagnosis and characterization of breast masses on ultrasound: added value for the inexperienced breast radiologist. Medicine, 98(3), e14146. https://doi.org/10.1097/MD.0000000000014146
25. Ben-Cohen, A., & Greenspan, H. (2020). Liver lesion detection in CT using deep learning techniques. In Handbook of medical image computing and computer assisted intervention (pp. 65-90). Academic Press. https://doi.org/10.1016/B978-0-12-816176-0.00008-9
26. Gonzalez, R. C. (2009). Digital image processing. Pearson Education İndia.
27. Beimers, L., Tuijthof, G. J. M., Blankevoort, L., Jonges, R., Maas, M., & van Dijk, C. N. (2008). In-vivo range of motion of the subtalar joint using computed tomography. Journal of biomechanics, 41(7), 1390-1397. https://doi.org/10.1016/j.jbiomech.2008.02.020
28. Mochimaru, M., Kouchi, M., & Dohi, M. (2000). Analysis of 3-D human foot forms using the free form deformation method and its application in grading shoe lasts. Ergonomics, 43(9), 1301-1313. https://doi.org/10.1080/001401300421752
29. Nilsson, M. K., Friis, R., Michaelsen, M. S., Jakobsen, P. A., & Nielsen, R. O. (2012). Classification of the height and flexibility of the medial longitudinal arch of the foot. Journal of foot and ankle research, 5, 1-9. https://doi.org/10.1186/1757-1146-5-3
30. Rodrigo, A. S., Goonetilleke, R. S., & Witana, C. P. (2012). Model based foot shape classification using 2D foot outlines. Computer-Aided Design, 44(1), 48-55. https://doi.org/10.1016/j.cad.2011.01.005
31. Luo, X. D., Xue, C. H., & Li, Y. (2017). Study on the foot shape characteristics of the elderly in China. The Foot, 33, 68-75. https://doi.org/10.1016/j.foot.2017.04.004
32. Reis, H. C., Bayram, B., & Seker, D. Z. (2016). A semiautomatic segmentation approach to biometric measurement of the talus bone of sedentary women and ballerinas using CT images. Asian Biomedicine, 10(5), 455-459. https://doi.org/10.5372/1905-7415.1005.508
33. Goodyear, M. D., Krleza-Jeric, K., & Lemmens, T. (2007). The declaration of Helsinki. British Medical Journal, 335(7621), 624-625. https://doi.org/10.1136/bmj.39339.610000.BE
34. https://www.turkrad.org.tr/
35. Doğan, S., & Altan, M. O. (2010). CT, MR kesitleri ve dijital görüntüler kullanılarak tümörlerin belirlenmesi. İTÜDERGİSİ/d, 2(4), 45-55

Mersin Photogrammetry Journal

https://dergipark.org.tr/en/pub/mephoj

e-ISSN 2687-654X

Close-range photogrammetry for analysis of rock relief details: An investigation of symbols purported to be Jewish Menorahs in Rough Cilicia

Daniel Crowell Browning Jr *[1]

[1] *Pearl River Community College, Humanities Department, USA, dbrowning@prcc.edu*

Cite this study: Browning Jr, D. C. (2024). Close-range photogrammetry for analysis of rock relief details: An investigation of symbols purported to be Jewish Menorahs in Rough Cilicia. Mersin Photogrammetry Journal, 6 (1), 39-51

https://doi.org/10.53093/mephoj.1434605

Keywords
Photogrammetry
DEM
Rock Reliefs
Rough Cilicia
Symbols

Research Article

Received: 09.02.2024
Revised: 24.02.2024
Accepted: 27.02.2024
Published:16.03.2024

Abstract

Close-range photogrammetry of certain rock reliefs in Rough Cilicia was used to investigate published claims that symbols in them represent Jewish menorahs, but with five branches instead of the usual seven. Details of ancient rock reliefs are difficult to assess because of mottled rock texture, color variation, wear or damage, and conditions of lighting. Thus, published photos of the rock reliefs in question are insufficient for evaluation of claims about them. Simple photogrammetry, however, produces 3D and digital elevation models that eliminate visual ambiguity and provide certainty of detail for analysis. This study describes the simple, non-invasive, and inexpensive data collection technique and the photogrammetry software processing workflow for creation of such models. Resulting models in various presentation formats provide factual data for reevaluation of the claimed menorahs themselves and their relationship to other elements of the reliefs. These findings contribute to informed discussion on interpretation of the symbols and their meaning. Adoption of the process described here is encouraged for subsequent publication, analysis, and interpretation of rock relief details in the region.

1. Introduction

Photogrammetry has firmly established itself as a tool in archaeology and recent years have seen a significant increase in its use [1]. The availability of unmanned aerial vehicles (UAVs), innovations in photogrammetry software, and the relative cost decreases in both have now made it a routine alternative to traditional methods for making site plans, elevations, and sections [1-2]. The most often employed form in archaeological work is modeling using the technique called “structure from motion” (SfM), in which tie points between overlapping photos, as well as camera positions and angles are determined and used by complex software packages. The principles and processes of SfM are well-established and documented [2-3] and do not need to be rehearsed here. Simple SfM photogrammetry can be utilized in the field efficiently, with data collection carried out by non-photogrammetry experts having minimal training [3].

The potential of SfM for high accuracy detail has been well-established in geomorphology [4]. In archaeology, its utility for detail detection is demonstrated by recent use in caves for reassessment of Paleolithic figural art [5] and to reveal artwork imperceptible to the human eye under difficult conditions [6]. Meanwhile, the technique has been increasingly used as a simple and low-cost option for documentation of petroglyphs [7] and other forms of rock art [8-9]. The combination of accuracy, ease, and low cost make SfM photogrammetry an ideal tool for analysis of detail in rock reliefs, as well as for routine documentation and presentation of them.

A recent review of SfM applications laments that most current publications are “proof-of-concept” studies, and that photogrammetry is rarely used for actual analysis of archaeological material [10]. This article presents such analysis; conducted with close-range photogrammetry to reveal and clarify details of previously published rock reliefs depicting certain symbols in the region known as Rough Cilicia.

Rock-cut reliefs are a prominent and significant feature of the archaeological remains in Rough Cilicia. Figural reliefs are especially well-documented, and their context is generally understood [11]. Symbols are also prominent in the region, appearing most often in relief on

building components but also on living rock. These are more difficult to assess and interpret. Some symbols have been grouped and plausibly identified, [12] but their function and meaning for ancient persons remains obscure [13].

In many cases, assessment and identification of symbols is hampered in the field and in documentation for publication by problems inherent in rock reliefs. These include: conditions of lighting; mottled color and texture of the rock; growth of lichens; and wear or damage to the surface.

This study examines such a case; rock relief symbols I believe to be misidentified and misinterpreted. It also demonstrates the great potential of simple and low-cost close-range SfM photogrammetry for this type of research. Finally, it encourages adoption of this technology—heretofore underutilized by archaeological work in Rough Cilicia—for documentation, assessment, and publication of rock reliefs; and, indeed, for analysis and reevaluation of details as conducted here.

2. Method

The work reexamined a set of rock reliefs, each apparently including the same symbol. All were previously published in archaeological reports with monochrome photographs and verbal descriptions. Each relief was visited in December 2023 and documented in a non-invasive manner by digital cameras for later photogrammetric processing. The resulting 3D models greatly facilitated analysis of the subject examples. Results also provide exemplars for other archaeological research by demonstrating potential for presentation, analysis, and interpretation.

2.1. The Reliefs

The three subject reliefs examined here feature a certain symbol identified by various researchers as a Jewish menorah, a view questioned or rejected by other scholars [14], including a colleague and myself [15]. Hereafter, this symbol is designated by the neutral term *semeion* (ancient Greek *σημεῖον*, "sign," "token," or "mark") [16]. Each of the three reliefs feature the *semeion* in combination with known pagan symbols; two on door lintels at Köşkerli and OÖ rendibi, and one accompanying a larger figural scene called the Athena Relief. All occur in the territory of Olba, a city of the Hellenistic through late Roman periods in the present district of Mersin, part of the region known in antiquity as Rough Cilicia (Figure 1).

The basis for identification of the relief symbols as menorahs comes from a small limestone altar in the Silifke museum, said to originate from the Olba area, on which a *semeion* appears prominently (Figure 2). The original publisher identified the symbol as "without a doubt" related to Judaism, despite the fact that the *semeion* on the altar has only four "branches" as opposed to the usual seven on a Jewish menorah. He argued that the star above "replaced" one branch and that five branches is a "very frequent simplification" [17].

The same symbol in each relief of this study is called a "menorah" [18-19] and "five branched" by subsequent scholars [20]. Published photos do not provide the detail necessary to dispute this claim. Thus, these reliefs provide excellent examples of the difficulties in description of rock relief details, as well as the shortcomings of usual monochrome photographic documentation. More importantly, they demonstrate the advantages of close-range photogrammetry for those

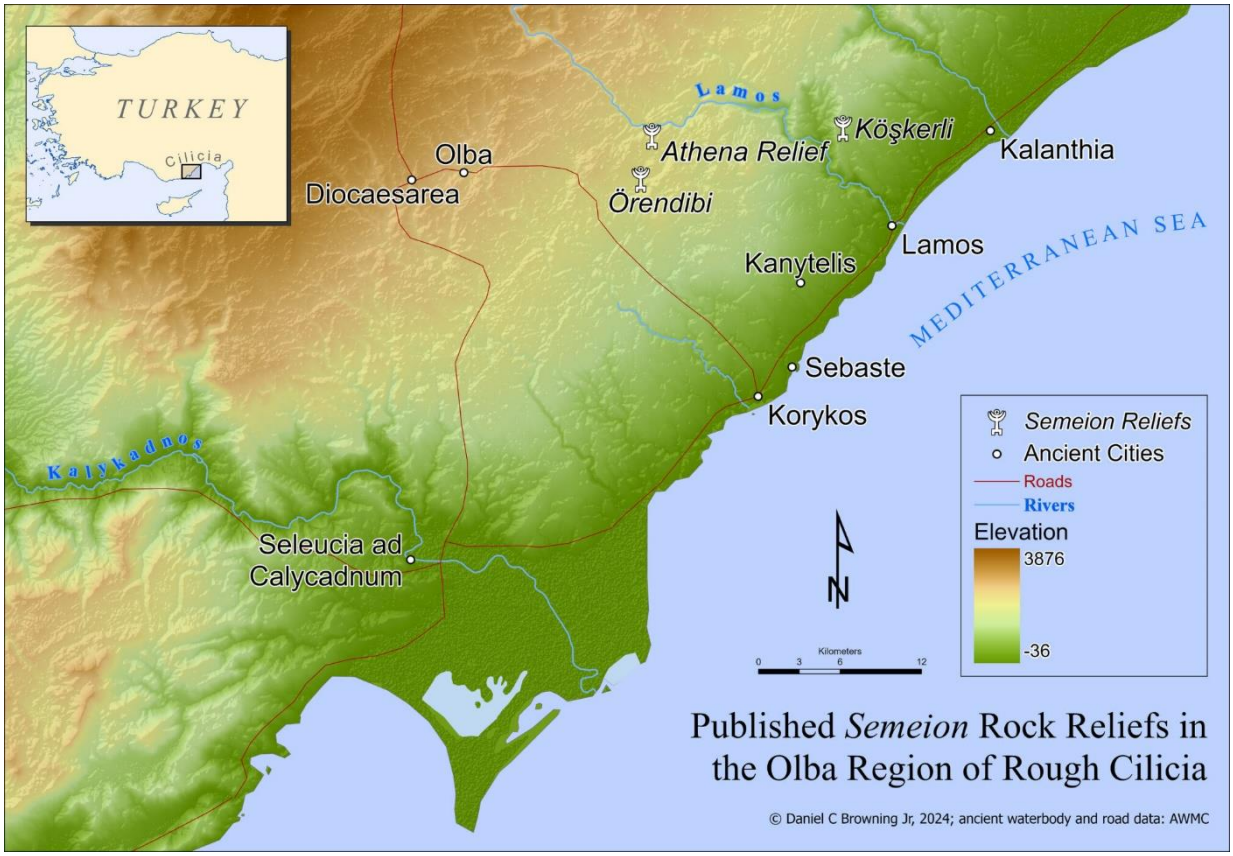

Figure 1. Map of published *semeion* relief sites in eastern Rough Cilicia.

tasks and its utility for reassessment by other researchers.

Figure 2. The Silifke Museum altar with *semeion* motif.

2.2. Photography

The sufficiency of inexpensive DSLR cameras for close-range object photogrammetry has already been established in archaeology [7, 21]. This study emphasizes the practical use of low-cost equipment and ease of data collection for survey projects. Accordingly, an older consumer grade Canon EOS Rebel T2i with a 50mm lens served as the main camera. Also on hand was a second Canon T2i with a 28-55mm zoom lens for tight areas and a UAV-mounted Hasselblad L1D-20c for high shots. The Canon T2i cameras do not contain onboard GPS and thus do not embed location or reference system information in image EXIF fields as do professional or specialized cameras like the Hasselblad L1D-20c.

Most photogrammetry tasks currently use SfM software, in which camera positions and angles are determined in image space without coordinates or scale. Professional software, however, automatically extracts geographic coordinate system and position information from EXIF data, if it is available, and creates position and scale. Even so, large projects such as UAV mapping, cultural monument documentation, or the like, employ ground control points (GCPs) to improve location accuracy and ensure precision in measurement. Experiments in SfM documentation of petroglyphs show that the time-consuming and complex use of GCPs is not required to obtain results comparable to laser scanning for such projects [3]. Moreover, placement of GCP markers involves physical contact with and potential damage to the artifact.

To avoid contact with the reliefs, GCP markers were not used in this study. However, as noted below (section 2.3.2), a reference scale is required for creating a digital elevation model (DEM). A 10cm photogrammetric scale was placed in the photographic scene where possible to provide that reference.

Reliefs of interest were photographed in a simple fashion without tripods or special lighting. Autofocus was used, but other camera settings were set manually for most images. Depending on lighting conditions, shutter speed was kept at 1/160 if feasible, and apertures as small as possible for greater depth of field. Each relief scene was covered entirely with maximum overlap of photos from numerous positions and an effort to keep angles at less than 30 degrees from perpendicular to the surface. More photos than needed were taken so lower quality ones could be identified by the software and excluded. Figure 3 illustrates camera positions relative to a sparse cloud of the Köşkerli lintel (after initial processing described below).

Photographic shooting requires only a single person in theory. However, the greatest impediment to full coverage of reliefs in Rough Cilicia is blockage by foliage, especially the ubiquitous scrub oaks of the region. For the fallen lintel at Köşkerli as well as the standing lintel at Örendibi, an assistant held back scrub branches to enable a clear view during shooting. Another potential impediment is orientation of fallen reliefs to the ground or other remains, limiting shooting distances or angles. Hence the backup Canon T2i with a wide angle zoom lens; but it was not required for these subjects. The Athena Relief, however, could not be photographed from above the symbols by hand-held camera without contact with the monument. Therefore, the UAV-mounted Hasselblad provided higher elevation photos and embedded reference data for scale.

2.3. Data Processing

2.3.1. Photogrammetry software and general workflow

All photogrammetry processing employed Agisoft Metashape Professional 2.1.0, which has emerged as the dominant software for archaeological work [10]. Table 1 outlines the basic “Workflow” steps in Metashape with options used for each relief. Metashape terminology appears hereafter with quote marks on first use. Photo organization and static output image processing used ACDSee Photo Studio Ultimate 2020, version 13.0.

The sequence in Table 1 was carried out for the full surface of each relief to provide perspective and relationship between the symbols. Each resulting full model “chunk” could then be duplicated and cut down using selection and delete tools to focus on *semeion* representations and other symbols of interest.

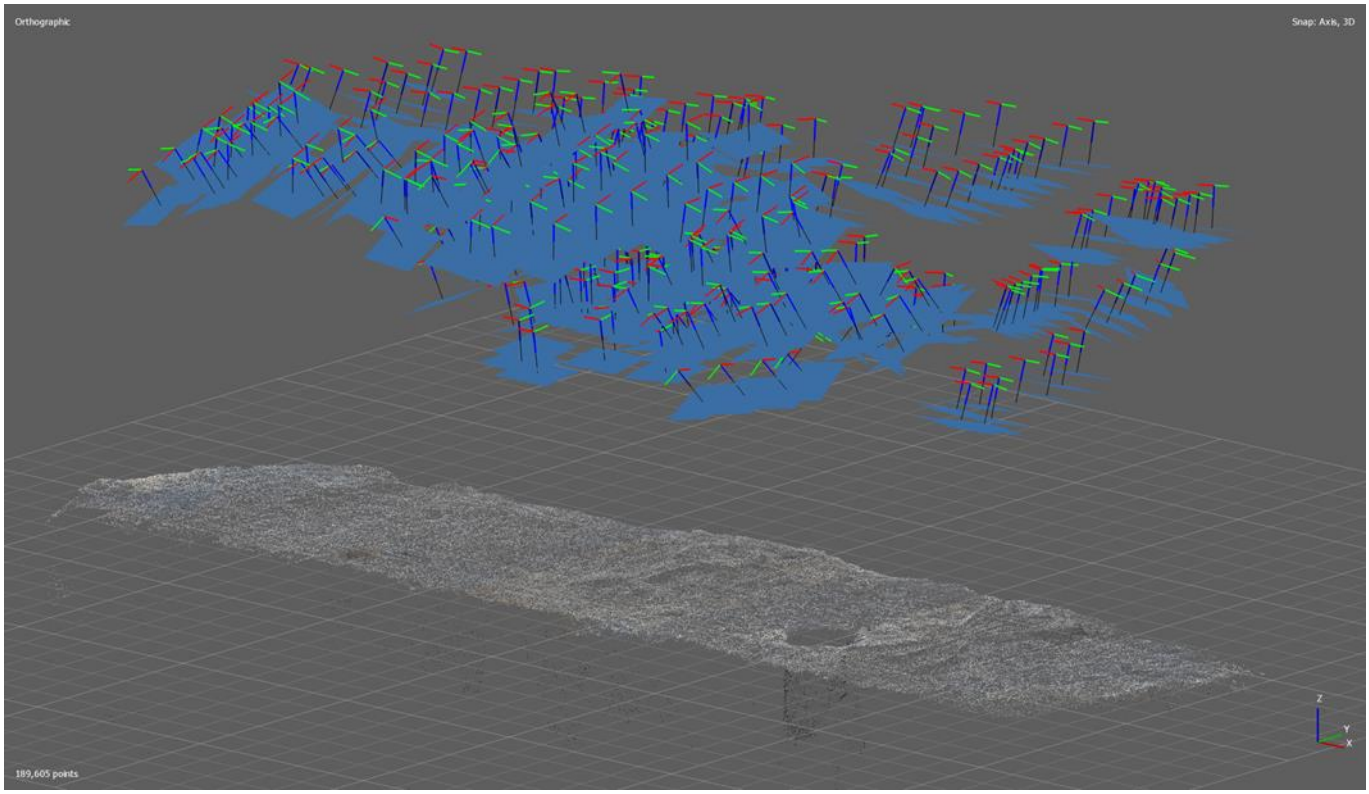

Figure 3. Metashape calculated camera positions and sparse cloud (tie points) for the Köşkerli lintel.

Table 1. Photogrammetry workflow in Agisoft Metashape Professional 2.1.0.

Metashape Workflow step	Non-default options used	Subsequent tools; operations prior to next step	Result (alternate terms)
Add Photos	(Add folders)	Estimate image quality; disable photos with value < 0.500	
Align Photos	Accuracy: High	Optimize Cameras; rotate and resize "region" to limit processing area	Tie point cloud (sparse cloud)
Build Point Cloud	Quality: High Depth filtering: Aggressive	Use selection tools to highlight and delete extraneous points	Dense cloud
Build Mesh	Surface type: Arbitrary (3D) ✓ Calculate vertex colors	Duplicate 3D model for multiple texture options	3D surface model (wireframe)
Build Texture	Diffuse and Occlusion	Reorientation and referencing required before DEM creation (details in text)	Photorealistic surface for model
Create DEM		Change display options for best visual representation	Orthometric DEM

2.3.2. Special considerations and procedures for analyzing rock relief symbols

The goal in photogrammetric analysis of rock relief symbols is clear revelation of the carved design details. Therefore, relative heights of various parts of the work above the background plane must be highlighted. For reliefs, the default background plane equals the X-Y axis plane and heights, or "elevations," are along the Z axis. Most rock reliefs have a vertical orientation, with heights along the Z-axis parallel to the ground towards a standing viewer. Therefore, a plan view ("top" view in Metashape) actually shows the front or "face" of the relief. Orientation of the photogrammetry-derived model to those axes is important for presentation and assessment, especially for depiction of relief height detail.

If photos with EXIF GPS data are used for processing, Metashape (and other software packages) automatically assigns a default geographic coordinate system as the reference system to the resulting digital model "object." This reference system must be cleared and replaced with a "local coordinate system" to align the object to the X, Y, and Z axes as noted above. If photos do not have embedded GPS data, the software assumes a local coordinate system without reference or precise scale and with arbitrary orientation, so object reorientation to the axes is still required.

For each relief, the digital model was rotated and moved so the background plane of the relief aligned with the X and Y axes. Because relief background planes (the rock surfaces) are not completely smooth or even, this procedure involved visual judgement. Viewing the object as a point cloud in the "elevation" display option along each axis provided the best means for making this judgement (Figure 4). Both the object and its "region" (the boundaries for processing) were rotated and adjusted using Metashape's transform tools. The "update transform" tool fixed the new orientation. This procedure could be done after creation of the point cloud or at any point later to the full model.

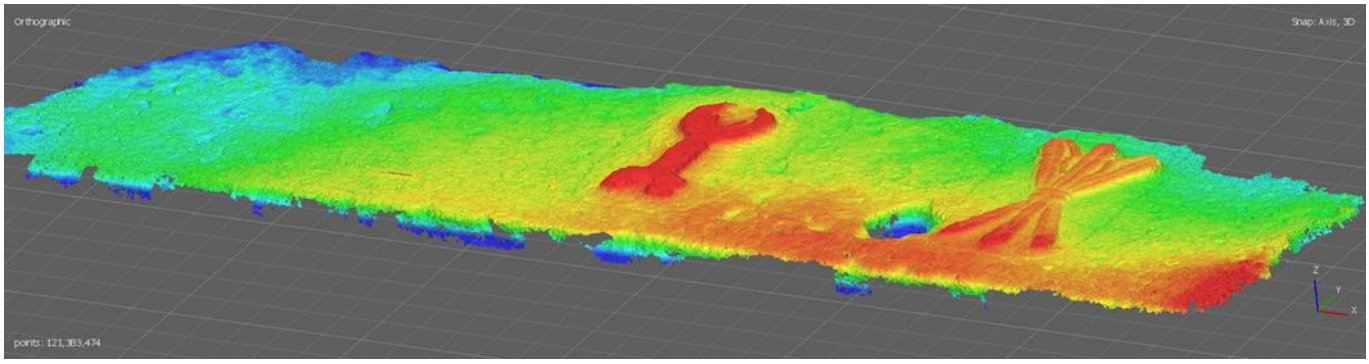

Figure 4. The Köşkerli lintel face dense point cloud with elevation display in Metashape.

To produce a DEM in Metashape, the properly oriented object must be referenced or scaled. The 10cm measuring card placed in the photographic scene allowed creation of reference scale using the following procedure (using tools in the reference pane of Metashape): 1) add markers at beginning and end of the 10cm scale; 2) select both markers; 3) create scale bar; 4) edit scale bar by assigning 0.01(m) to the distance field; and 5) update transform.

If no measuring scale could be safely placed and embedded GPS data from the photos were relied upon for scaling or reference, this will be lost when the reference system is cleared for reorientation to the X, Y, and Z axes. In this case, the following workaround was developed (described using Metashape tools and terminology): 1) add two or three pairs of separated markers at different orientations on the object's surface; 2) using the ruler tool, measure and note distances between each pair of markers; 3) clear GPS data from photos and "uncheck" them; 4) open reference settings for "chunk" and set coordinate system, camera reference, and marker reference to "Local Coordinates (m)"; 5) for each pair of markers, select and create scale bar; 6) edit scale bars by assigning noted distances; 7) "check" markers and scale bars; 8) update transform.

Using a local coordinate system for reference establishes arbitrary zero points for the main axes of each object. For this study no CGPs were placed, and no physical measurements were made of any monuments or remains. Therefore, all indicated elevation and other metric figures should be considered accurate relative to the objects concerned, but not verified in terms of absolute precision.

2.3.3. Output for display and analysis

The 3D model can be displayed within the software in various modes: as tie points, dense cloud, or polygonal surface model. Multiple display options exist for each mode. After the "Build Mesh" step, the resulting polygonal surface model can be displayed as a wireframe, showing the vertices of all polygons; or as a solid, with all polygons in the same neutral color. All mesh models for this study were built with the "calculate vertex colors" option, so polygon vertices have color determined by the dense cloud points. This allows the "shaded" display mode, described below. If the source photos were taken under conditions that created significant shadows and highlights, Metashape's "remove lighting" tool could mitigate these before creating texture. Photos for the models created here did not require this process.

2.3.3.1. Interactive 3D models

The final step for display of solid 3D models with a photo-realistic surface is creation of texture. The default texture for 3D models is a "diffuse map," with color for each polygon determined from the original photos. Models of the three examples below with diffuse texture provided detailed, realistic, and accurate representations for each relief. The diffuse display, however, retains some of the problems for interpreting relief details from photos or in person: the mottled color and texture of the rock (Figure 5).

A model can be exported from Metashape into any standard 3D object format and viewed with interactive rotation to inspect all details using a computer, tablet, or phone with proper software. Even with interactive 3D viewing, models with diffuse texture did not reveal the symbols as clearly and unambiguously as desired. Publishing 3D models online also requires permanent specialized accounts and/or embedded viewing software which creates complication, maintenance, and additional expense. Furthermore, interactive 3D models do not conform with most current print or journal publication options.

Metashape and other high-end photogrammetry software allow other display options that fit with this study's goal of demonstrating relatively simple and inexpensive options for publication and analysis of rock relief details. For each relief in the study, a wide variety of options were set up within Metashape and saved as static images. The following display types proved to be the most useful.

2.3.3.2. Static model display

The most straightforward method of creating figures for traditional publication is to save static images of 3D models in orientations that best illustrate details. But the limitations of the 3D model with a diffuse display were even more problematic with this approach (Figure 5). Other display options provided better detail clarity in both interactive 3D viewing and static display in a standard plan view.

Since polygon vertices were calculated with color while creating the mesh for each model, they could be displayed with effective realism without the textures

map. The "shaded" view option displays polygons with colors interpolated from the vertices and shading created by a default ambient light. For each relief, this highlighted more surface detail (Figure 8a) than diffuse texture. More ambiguity was eliminated by the "solid" display option, in which all polygons have the same neutral color with relief highlighted by the default ambient lighting (Figure 8b).

Figure 5. Perspective of Köşkerli lintel *semeion* model with texture display.

The least ambiguous display for relief detail resulted from a technique used to achieve photorealistic display of 3D models or computer graphics. In the "Build Texture" step of general workflow (Table 1), one option allows creation of an "occlusion" map, in which each polygon is shaded according to how much ambient light reaches it. Normally combined with other textures to create shaded color, the resulting black-to-white ambient occlusion (AO) map revealed excellent detail when displayed alone without lighting (Figure 8c). This technique arguably provides the best illustration of the sculptor's intent, as it incorporates the effects of ambient lighting with elevation of relief.

2.3.3.3. Point cloud with elevation display

Since elevation above the background plane is the essence of relief work, elevation display options in the software were extremely helpful in analysis. The point cloud display mode with elevation option facilitated orientation of the full relief models (section 2.3.2 and Figure 4). It also provided an option for presentation in plan view.

For analysis of individual symbols, the full relief model was duplicated and reduced with selection tools and deletion of unnecessary areas. In some cases the remaining model required reorientation to its own local background plane. The elevation color ramp for point cloud display is the same as for DEMs in Metashape, with the range determined by point cloud field thickness. Trimming extraneous points on the back side of the symbol model (invisible in plan view) modified the color distribution for optimal presentation. Adjusted in this way, point cloud representation as elevation dramatically revealed symbol details as relative height (Figure 6, 8d).

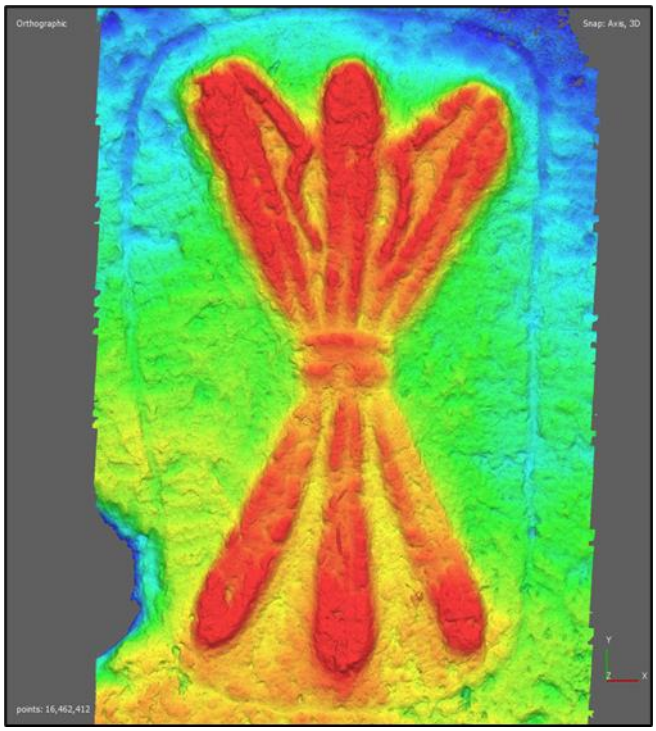

Figure 6. Köşkerli thunderbolt point cloud with elevation display option.

2.3.3.4. DEM and section profiles

Properly oriented and referenced models also permitted the creation of meaningful DEMs with relative elevations above the background plane. DEMs produced by Metashape (and other software, such as Pix4D) default to a widely used violet-to-red color ramp for stretch display. This accepted standard presents elevation changes in relief quite well when combined with hillshading (also a default in Metashape for DEMs). The stretch color ramp was manually adjusted by assigning values to colors in the palette for most effective presentation of specific reliefs (Figure 8e). Substituting a grayscale palette gives a different option suitable for publishing in black and white or as a basis for a drawing of the figure (Figure 8f).

From the DEM, cross section profiles were created for areas of interest on reliefs. In Metashape a polyline was created along a section of interest. The context menu "measure" tool produced sections with profiles using the elevation color ramp. These profiles proved instructive for defining relationships between symbols.

3. Results

These described methods result in a variety of graphic options for presentation and tools for analysis of details and relationships in rock reliefs. They are

demonstrated in the following sections for the three rock reliefs of this study.

3.1. Köşkerli

About 125 m southeast of the Byzantine church ruins at Köşkerli lies a fallen and broken door lintel with a relief preserving a thunderbolt and *semeion* (Figure 7). The earliest published references to it describes the latter as a "simplified version of a menorah-candelabrum" [18] and (collectively with the following two examples) a menorah with "five arms" [20]. Both publications include the same black and white photograph from which the claimed descriptions cannot be verified or effectively refuted. The photogrammetric 3D model of the Köşkerli lintel relief removes ambiguity about the relief details and offers several display options that allow descriptive certainty. The *semeion* provides an excellent example.

Figure 7. Köşkerli: fallen lintel with relief of thunderbolt and *semeion.*

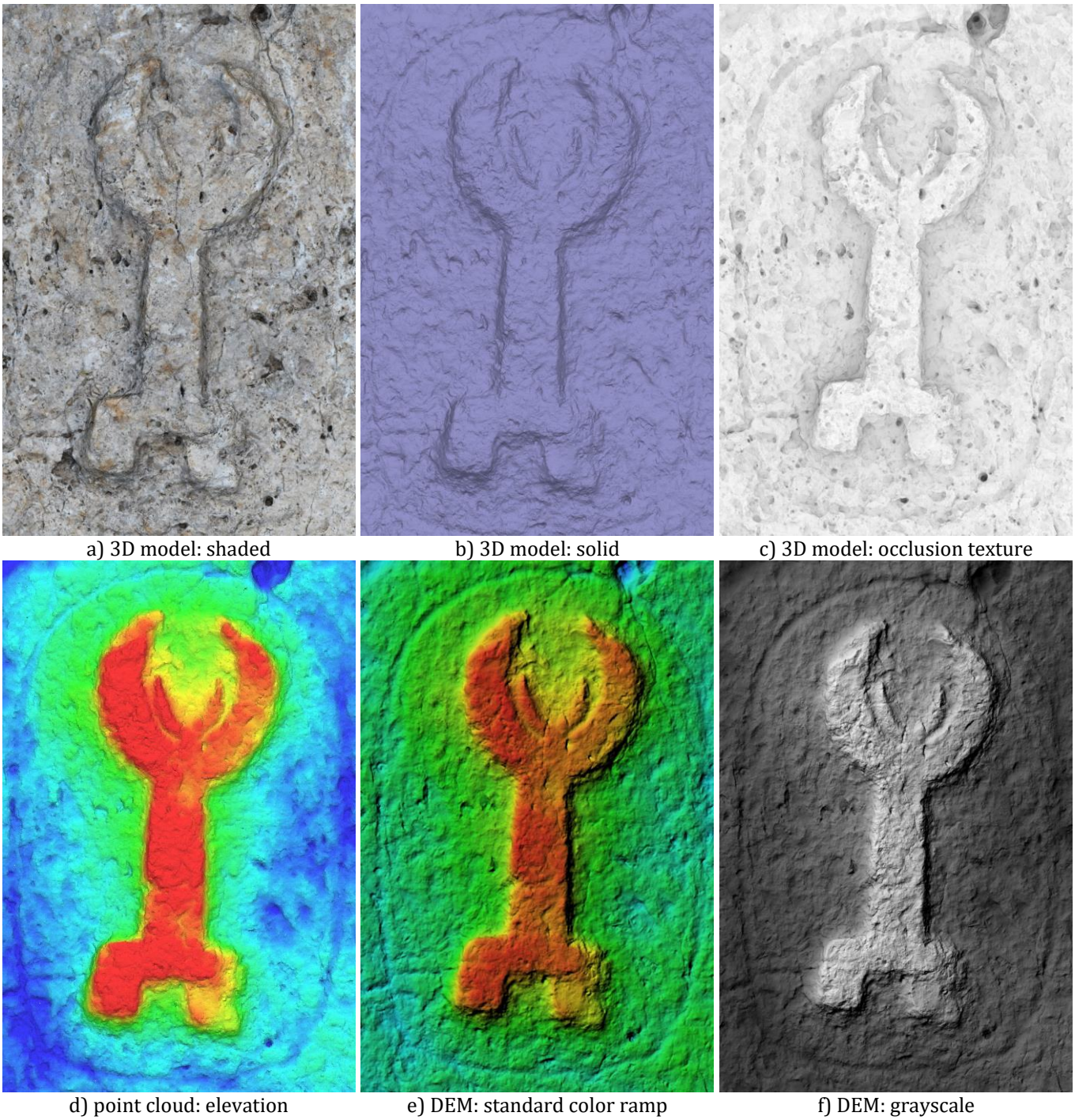

a) 3D model: shaded b) 3D model: solid c) 3D model: occlusion texture

d) point cloud: elevation e) DEM: standard color ramp f) DEM: grayscale

Figure 8. The Köşkerli lintel *semeion*: photogrammetric model in various display options.

As shown above, the 3D model displayed with diffuse texture does not reveal detail (Figure 5). A shaded view (Figure 8a) offers slight improvement and a solid view (Figure 8b) even more. These views make it clear that the symbol features two nested crescent shapes on a column rising from a two-footed stand or base; the same elements as the symbol on the Silifke museum altar (Figure 2) but with differing proportions and lacking the star above.

An optical illusion created by fissures and the ambient lighting on the 3D model in the shaded and solid views allows the viewer to imagine a central fifth "branch," as claimed by earlier interpreters [20]. Model views with occlusion only (Figure 8c) and point cloud elevation (Figure 8d), however, eliminate that possibility. They also preclude any claim that a star (substituting for a fifth branch per the original publication of the Silifke museum altar) [17] was part of the figure. The DEM displays (Figure 8e, 8f) offer additional confirmation and provide alternate views suitable for presentation or publication.

3.2. Örendibi

Ruins called Örendibi, west of the village of Somek, contain a standing door lintel with three symbols in relief: an apparent *semeion*, thunderbolt, and shield (Figure 9). The *semeion* is somewhat smaller than the other two symbols, slightly skewed, and less detailed than those at the other sites. It was identified by the initial investigator as a "candlestick" (Türkçe *şamdan*) [22], later as a "menorah-candelabrum" [19], and then as a menorah having "five arms" [20]. Of these, only the latter publication contains a photo; again, with insufficient detail for judgement and without showing the full lintel.

The photogrammetric model permits detailed assessment of the Örendibi symbol. The 3D model diffuse texture display (Figure 10a) retains the difficulties of a photo, in this case complicated by lichen growth. The other display options (Figure 10b-10d) reveal the *semeion* design clearly, with a two-footed stand and shaft supporting nested crescent shapes. As at Köşkerli, the symbol elements match those of the Silifke museum altar *semeion* but in different proportions and without the star. Some incongruities are notable in the field but not shown in the only previously published photo of the Örendibi lintel [20]. The three symbols are not arranged in the center of the lintel and the right side of the lintel is quite rough, hinting that something there was effaced in antiquity (Figure 9). The *semeion* is significantly smaller than the thunderbolt and shield. If another symbol once existed to the right of the shield, separated congruently with the thunderbolt opposite, those three symbols (alone, without the *semeion*) would compose a set appropriately centered on the lintel. A 3D model of the full lintel face provides easy access to data for discussion. A plan view of the shaded model (Figure 11) confirms field observations of the spacing of symbols and roughness on the right side. The DEM of the lintel face (Figure 12) highlights degradation on the right side and reveals that the smaller *semeion* symbol is executed in lower relief than the thunderbolt and shield. A section profile (Figure 12, top) further demonstrates the lower relief of the *semeion* and suggests a lowered background plane than for the other two symbols. It also underscores the extent of damage to the surface on the right side of the lintel. These details are consistent with the following possibilities: 1) an original third large symbol on the right side of the lintel was intentionally effaced; and 2) the *semeion* was added after the large symbols by lowering the background plane left of the thunderbolt and executing the symbol in much lower relief.

Figure 9. Örendibi: standing lintel with (l to r) *semeion*, thunderbolt, and shield.

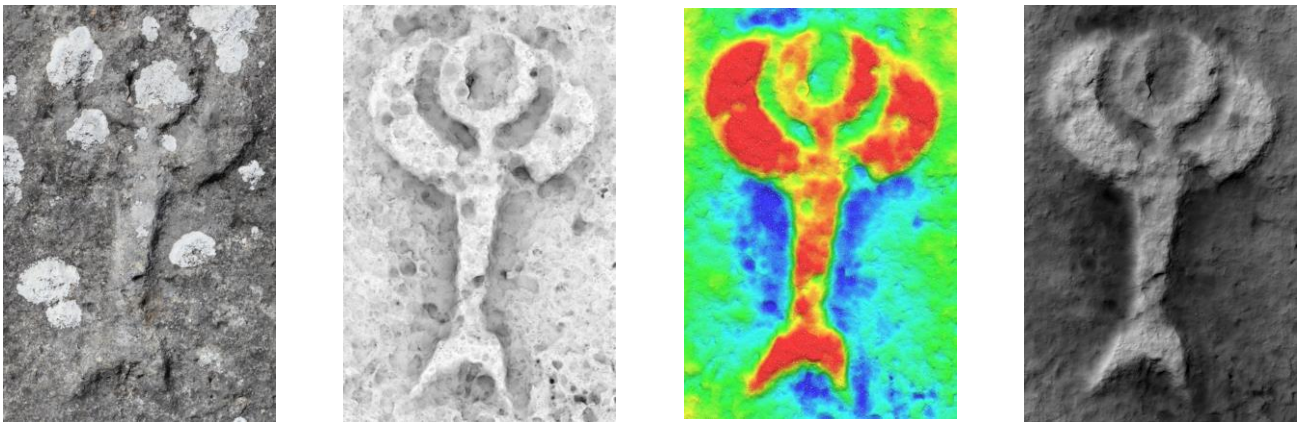

a) 3D model: textured b) 3D model: occlusion c) point cloud: elevation d) DEM: grayscale

Figure 10. The Örendibi lintel *semeion*: photogrammetric model in selected display options.

Figure 11. Örendibi lintel model in shaded view.

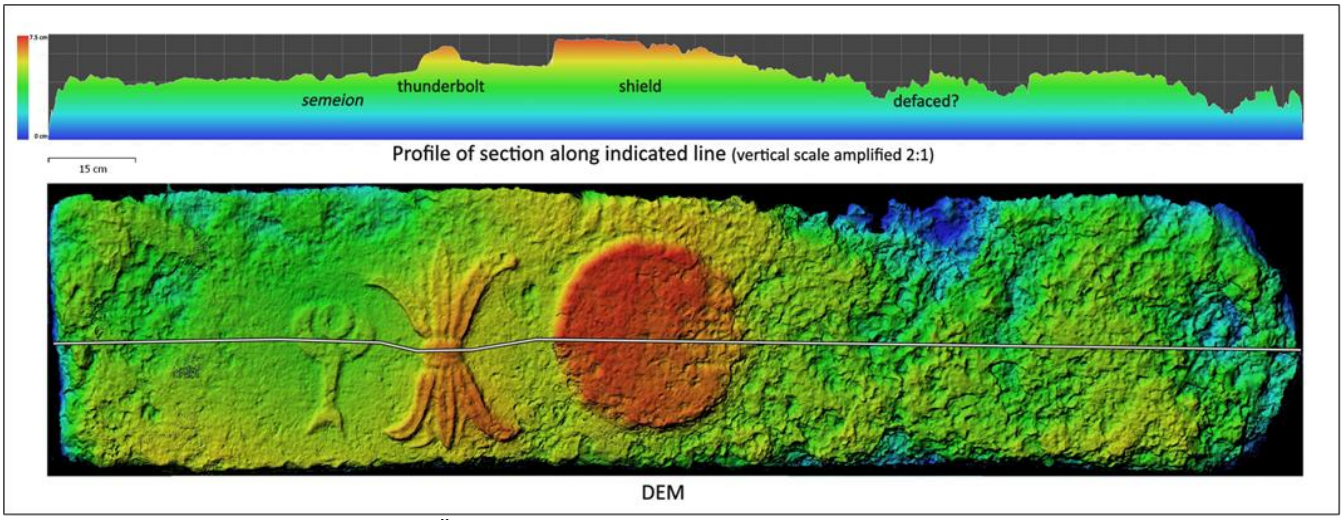

Figure 12. Örendibi lintel DEM (below) with section profile (above).

3.3. Athena Relief

A similar situation exists at the Athena Relief near Sömek, where a *semeion* and other symbols are found as adjuncts to an impressive shrine created for the goddess Athena (Figure 13) [11]. Two pilaster columns frame the scene; the one on the viewer's right decorated with three figures in relief: a crescent and star, an unidentifiable defaced object, and a thunderbolt. Outside the frame, right of the pilaster, a *semeion* in relief stands alone.

3.3.1. The Semeion

The Athena relief *semeion* is the clearest of the three rock relief examples in this study. The two-legged base, shaft, and nested crescents are evident in person and discernable in published photographs [11, 20]. Like the symbols at Köşkerli and Örendibi, however, it has been cited without argument as a "five-branched menorah" [20] when a fifth "branch" is not at all evident. One commentator, apparently relying on the assumption that a star substitutes for a fifth branch in the Silifke museum altar *semeion* [17] (see section 2.1 and Figure 2), asserts that Athena Relief example "contains a star at the top center of the menorah" [23].

The rock surface and texture could allow an observer to imagine a much-eroded star above the crescents. But the photogrammetric model eliminates speculation and doubt. Multiple views demonstrated that there is no fifth "branch" and no evidence for a star substituting for one. The 3D model with occlusion map display and DEM views are provided here (Figure 14a-14b).

Figure 13. Athena Relief.

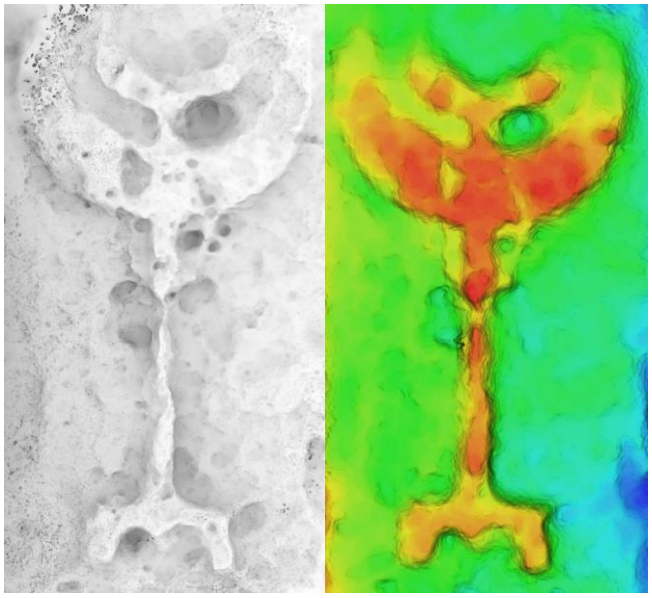

a) 3D occlusion b) DEM

Figure 14. Athena relief *semeion* model views.

3.3.2. Chronological order of the relief and symbols

The relationship of the symbols to the Athena relief is somewhat enigmatic and therefore subject to speculation. The original investigator assumed that the symbols were all part of the original design [11]. Some details, however, allow the possibility that the symbols were added later. Collectively, the symbols are more detailed and sharper than the Athena composition inside the pilaster frame, suggesting a different sculptor. Also, the pilaster surfaces are noticeably set back from their capitals and base (only the right base is preserved); more than necessary and even awkwardly. This would be the case if symbols in relief were added later by trimming back the pilaster. The full model of the Athena relief supplies data for discussion.

Figure 15 shows a DEM of the entire Athena relief with the XY plane as the background surface behind the goddess and the outer surface of the two pilaster column capitals at the same z-elevation. The DEM representation highlights certain details not immediately obvious in the field or in photos. Figure 16, created by assigning dense cloud points to "classes" in Metashape, provides a key for discussion.

The following observations stand out: 1) the left pilaster column surface is cut back more than the right; 2) the right pilaster column's left edge is uneven adjacent to the relief figures on it because of undercutting by the relief inside the frame; 3) three composition elements inside the frame (snake head, horse snout, and shield) seem truncated where they extend out to the plane of the adjacent pilaster surface; 4) a small "channel" separates the rim of Athena's shield from the right pilaster edge (left of the thunderbolt); 5) the natural rock falls away rapidly outside the right pilaster; and 6) the background surface for the *semeion* to the right inclines inward towards the pilaster. Section profiles of the DEM model enhance these observations (Figure 17-18).

The overall low height of the column surfaces as seen in section A-A' (Figure 17, top) is consistent with the theory that they were cut back at a later period to allow placement of the symbols on the right pilaster. Vertical section C-C' (Figure 18) also supports that supposition. That three elements—the snake's head on the upper left, the horse's snout on the right, and the rim of Athena's shield below the horse—would extend beyond the frame of the pilasters in the original composition seems unlikely. Their truncation at the existing pilaster face planes (Figure 15) is thus also consistent with a suggestion that the symbols were added later. For the rim of the shield, reduction of the pilaster would also have created a need for the defining "channel" between it and the pilaster surface. Section B-B' (Figure 18) highlights that relationship.

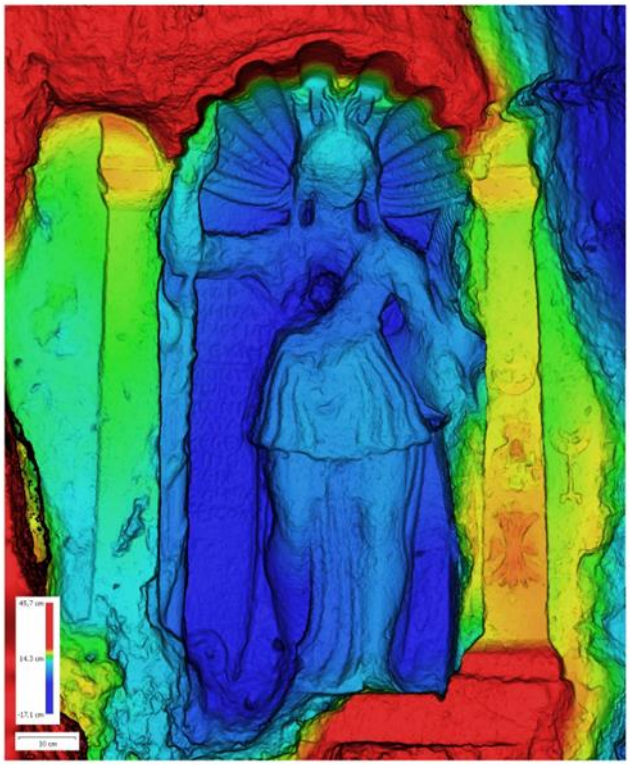

Figure 15. Athena relief: DEM.

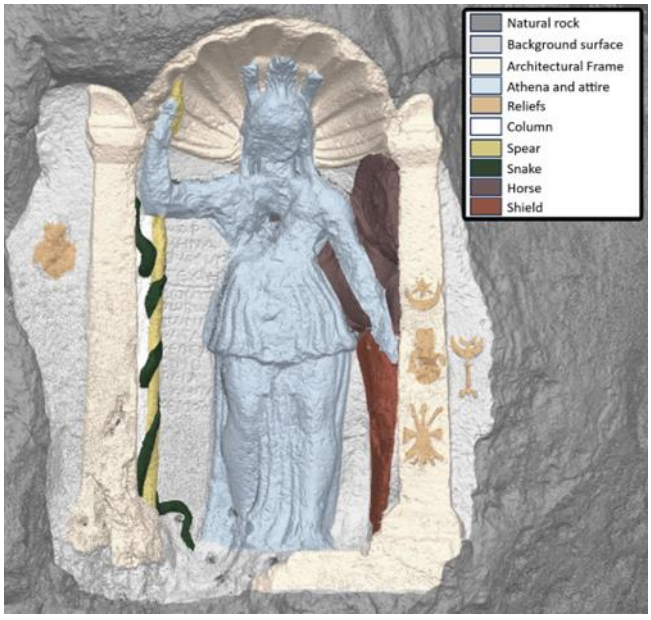

Figure 16. Athena relief: key for discussion.

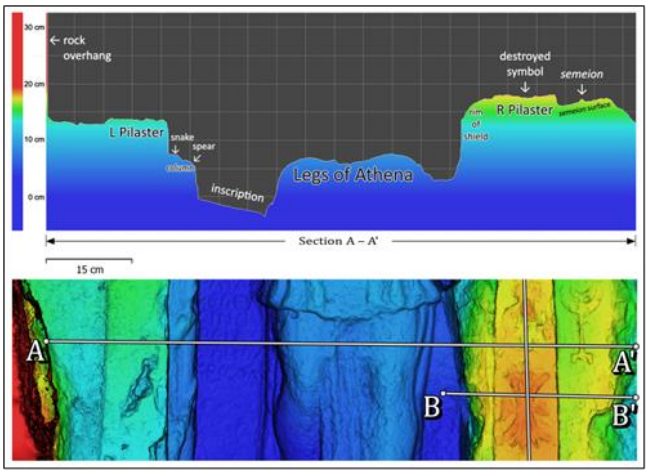

Figure 17. Athena Relief detail: DEM showing section lines (bottom) with section profile A-A' (top)

Finally, sections A-A' and B-B' clearly demonstrate the inclined background surface for the *semeion* carved outside the right pilaster (Figure 17, 18). If the *semeion* was added after the symbols on the pilaster itself, creation of such a surface would have constituted the most economical solution in the limited space still available.

4. Discussion

4.1. The Semeion: Data for Identification and Interpretation

Photogrammetric 3D models created in this study supply unambiguous data for discussion and evaluation of the Köşkerli, Örendibi, and Athena reliefs. Details illuminate the semeion representations as well as their relationship to other symbols appearing in the reliefs.

The models demonstrate conclusively that the symbols of interest in the three reliefs share the following features: 1) a two-legged base; 2) a vertical shaft; and 3) two nested crescent shapes of unequal size supported by the shaft.

These same features are found in the Silifke museum altar example. It is thus reasonable to equate the symbols; that is, each represents a semeion in the naming convention adopted here. However, the encapsulated star above the semeion on the altar is not present with the three rock relief symbols. Nor is there any other evidence for an additional arm or branch on them. Consequently, the published descriptions of the semeions at Köşkerli, Örendibi, and the Athena relief as "five branched" menorahs must be rejected as false.

Other details shown by the models are certain but require interpretation. For example, in every semeion, the nested crescent shapes taper to pointed ends. They resemble lunar crescents, horns, or even wings, rather than evoke the branches of menorahs. Also, the two crescents of each semeion are not always geometrically similar. The ones at Köşkerli and Örendibi are quite dissimilar when compared to the uniformity of the Silifke museum specimen. One reasonable conclusion is that the two crescent shapes are meant to represent two separate ideas. Taken together, these features mitigate against identification of the symbols as Jewish menorahs.

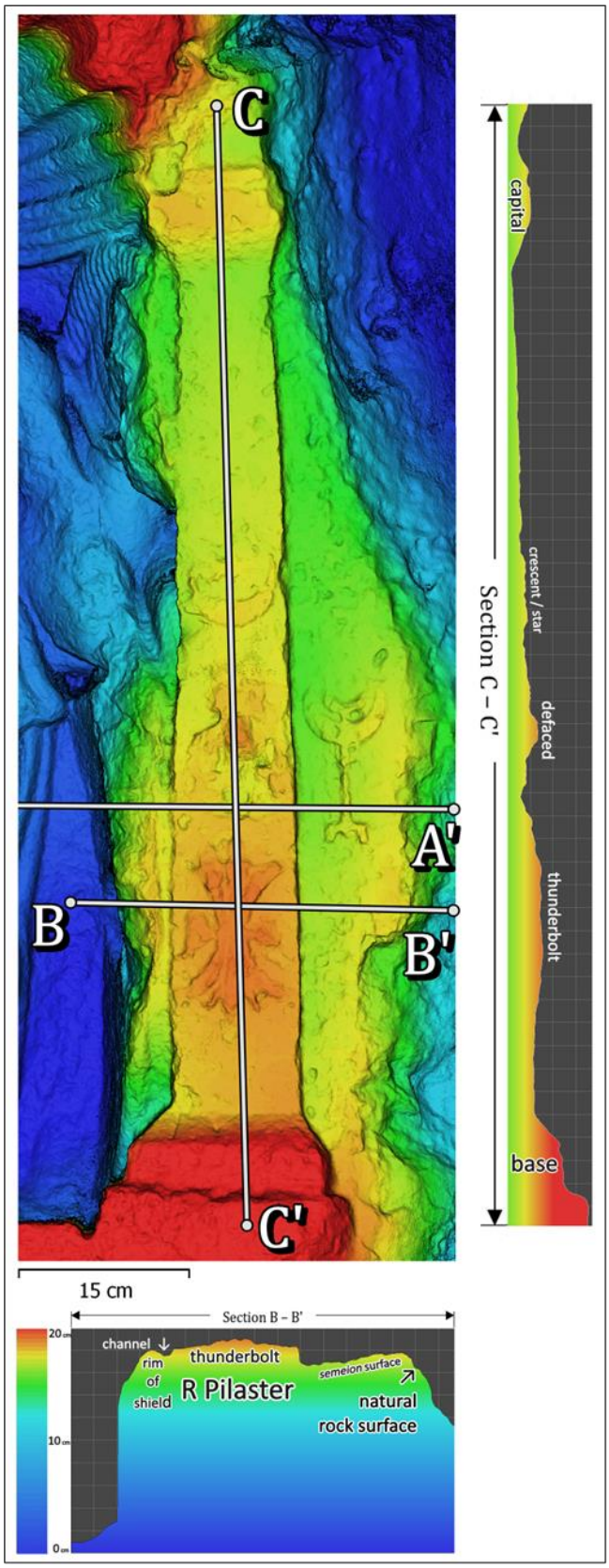

Figure 18. Athena Relief, right pilaster and symbols: DEM with section lines (top); section B-B' profile (bottom); and section C-C' profile (right).

Whether identified as menorahs or not, the relationship between the semeion and other symbols in each relief remains a question of interest. For this also, photogrammetry provides relevant data for discussion and interpretation. Setting the Silifke museum altar

aside, it is noteworthy that in each published rock relief in which the semeion appears, it occurs alongside a thunderbolt, conventionally understood as a symbol of Zeus. In two cases it occurs with a shield, the symbol of Athena: on the lintel at Örendibi (Figure 9, 11-12), and at the Athena relief where the shield is part of the main composition (Figure 16). The lintel at Köşkerli is broken (Figure 7), so it would be unsurprising to find a shield relief on the missing portion if it were located.

As observed in section 3.2, the semeion at Örendibi is smaller than the thunderbolt and shield. The DEM for the lintel shows it is also carved in significantly lower relief than the accompanying symbols. It also suggests that the area around it was lowered so the semeion could be added after the original composition. Furthermore, the right side of the lintel is heavily pitted and damaged, consistent with the intentional effacing of a now-lost symbol that would have evenly balanced the original composition without the semeion.

The Athena relief also has attributes that suggest later addition of the symbols to the right pilaster. The 3D model facilitates inspection of these features, while the DEM and section profiles add visual representation to their description and furnish factual data for arguments. The details outlined above (section 3.3.2) provide solid evidence to support a hypothesis that the symbols on the right pilaster were added to the Athena relief sometime after the original composition. They also provide support for conjecture that the semeion outside the frame represents an even later supplement to the monument.

Taken together, the photogrammetric data from Örendibi and the Athena relief give pause to any assumption that combinations of symbols including the semeion were always created together. This is an important consideration for any attempt to interpret the symbols and their collective meaning.

4.2. Close-range photogrammetry as a tool for archaeological presentation and analysis

Claims for identification of symbols like the semeion must be based on accurate description of their attributes. This is difficult when dealing with details of rock reliefs because of lighting conditions in the field, texture or color variations in the rock itself, lichen growth, and wear or damage. After identification and publication, evaluation of claims and reinterpretation become equally difficult for scholars relying on documentation by written description and/or monochrome photographs only.

The use of close-range photogrammetry provides objective presentation views with explicit detail and graphic representation of spatial relationships. These permit evaluation or reevaluation based on empirical evidence and allow arguments for identification founded on certainty. To put it another way, photogrammetry can eliminate subjective and potentially spurious claims involving physical details. Reconstruction and interpretation always involve some level of subjectivity in social sciences like archaeology and ancient history. Photogrammetry, however, provides one way to decrease uncertainty and provide more factual data in cases like the one in this study.

The above discussion (section 4.1) concerning the identification of the semeion and its relationship to other symbols was made possible by a simple process of collecting a sufficient number of suitable photographs in the field. The data collection process requires minimal training, can be performed with widely available and inexpensive equipment, and takes very little time. The only appreciable expense is the software for processing the data and the only expertise required is that of the software user. For most survey or synthesis research, the latter elements could easily be incorporated through inter-departmental cooperation and/or interdisciplinary project design.

5. Conclusion

The simple close-range photogrammetry method utilized in this study leads to conclusions in the specific case investigated, as well as for archaeological methodology.

For the *semeion*, this study demonstrates conclusively that prior identifications of the symbol as a "five branched" menorah are based on inaccurate assessments of the three rock reliefs and must be rejected. Other questions of interpretation remain open, such as whether the *semeion* has any connection to the Jewish menorah and how it relates to the other symbols with which it appears in the rock reliefs. For these issues, the photogrammetry results provide factual data that can be incorporated into interpretive arguments. This is not the appropriate venue for complete evaluation and historical interpretation of this intriguing symbol. A forthcoming study will present full arguments elsewhere.

For archaeological methodology, this analysis shows the value of close-range SfM photogrammetry for reevaluation of previously published rock relief symbol identifications. By extension, it also highlights its potential utility for initial assessment and publication of such elements. Given the relative ease and economy of simple close-range photogrammetry for data-gathering, it should become a standard part of research design for all projects that involve the reporting, identification, and interpretation of rock relief details—perhaps especially in Rough Cilicia, where reliefs with enigmatic symbols abound

Acknowledgement

Support for the acquisition of Metashape software was provided by the Faculty and Staff Association of the Forrest County Campus of Pearl River Community College, Mississippi. Special thanks are also due to my longtime friend and colleague David Maltsberger, for research collaboration in our larger joint project and assistance in data gathering.

Conflicts of interest

The authors declare no conflicts of interest.

References

1. Marín-Buzón, C., Pérez-Romero, A., López-Castro, J. L., Ben Jerbania, I., & Manzano-Agugliaro, F. (2021). Photogrammetry as a new scientific tool in archaeology: Worldwide research trends. Sustainability, 13(9), 5319. https://doi.org/10.3390/su13095319
2. Verriez, Q., Tomasinelli, A., & Thivet, M. (2023). A Guide to Orthophotographic Surveying Using Photogrammetry as Applied to Archaeological Heritage: From the Choice of Tools to Process Settings Within the Open-source Software MicMac (IGN ENSG). Presses universitaires de Franche-Comté.
3. Peña-Villasenín, S., Gil-Docampo, M., & Ortiz-Sanz, J. (2019). Professional SfM and TLS vs a simple SfM photogrammetry for 3D modelling of rock art and radiance scaling shading in engraving detection. Journal of Cultural Heritage, 37, 238-246. https://doi.org/10.1016/j.culher.2018.10.009
4. Verma, A. K., & Bourke, M. C. (2019). A method based on structure-from-motion photogrammetry to generate sub-millimetre-resolution digital elevation models for investigating rock breakdown features. Earth Surface Dynamics, 7(1), 45-66. https://doi.org/10.5194/esurf-7-45-2019
5. Strasser, T. F., Murray, S. C., van der Geer, A., Kolb, C., & Ruprecht Jr, L. A. (2018). Palaeolithic cave art from Crete, Greece. Journal of Archaeological Science: Reports, 18, 100-108. https://doi.org/10.1016/j.jasrep.2017.12.041
6. Simek, J. F., Alvarez, S., & Cressler, A. (2022). Discovering ancient cave art using 3D photogrammetry: pre-contact Native American mud glyphs from 19th Unnamed Cave, Alabama. Antiquity, 96(387), 662-678. https://doi.org/10.15184/aqy.2022.24
7. Sanz, J. O., Docampo, M. D. L. L. G., Rodríguez, S. M., Sanmartín, M. T. R., & Cameselle, G. M. (2010). A simple methodology for recording petroglyphs using low-cost digital image correlation photogrammetry and consumer-grade digital cameras. Journal of Archaeological Science, 37(12), 3158-3169. https://doi.org/10.1016/j.jas.2010.07.017
8. Castagnetti, C., Rossi, P., & Capra, A. (2018, June). 3D Reconstruction of rock paintings: a cost-effective approach based on modern photogrammetry for rapidly mapping archaeological findings. In IOP Conference Series: Materials Science and Engineering, 364(1), 012020. https://doi.org/10.1088/1757-899X/364/1/012020
9. Jalandoni, A., & May, S. K. (2020). How 3D models (photogrammetry) of rock art can improve recording veracity: a case study from Kakadu National Park, Australia. Australian Archaeology, 86(2), 137-146. https://doi.org/10.1080/03122417.2020.1769005
10. Magnani, M., Douglass, M., Schroder, W., Reeves, J., & Braun, D. R. (2020). The digital revolution to come: Photogrammetry in archaeological practice. American Antiquity, 85(4), 737-760. https://doi.org/10.1017/aaq.2020.59
11. Durugönül, S. (1989). Die Felsreliefs im rauhen Kilikien. B.A.R.
12. Bent, J. T. (1890). Cilician Symbols. The Classical Review, 4(7), 321-322.
13. Durugönül, S. (1998). Türme und Siedlungen im Rauhen Kilikien: eine Untersuchung zu den archäologischen Hinterlassenschaften im Olbischen Territorium. Habelt.
14. Hachlili, R. (2018). The Menorah: Evolving into the Most Important Jewish Symbol. Brill.
15. Browning Jr, D. C., & Maltsberger, D. (2017). Memes, Moons, or Menorahs? Analysis of Claimed Syncretistic Jewish-Pagan Relief Symbols in Rough Cilicia. American Schools of Oriental Research 2017 Annual Meeting, Boston, MA.
16. Liddell, H. G., & Scott, R. T. (1889). An Intermediate Greek-English Lexicon: Founded Upon the Seventh Ed. of Liddell and Scott's Greek-English Lexicon. Clarendon Press.
17. Dagron, G., & Feissel, D. (1987). Inscriptions de Cilicie. De Boccard. No. 14.
18. Aydınoğlu, Ü. (2008). Olive oil production in Rough Cilicia: Production Installations–Settlement Pattern–Dating. In Olive Oil and Wine Production in Anatolian During the Antiquity, International Symposium, 1-18.
19. Aydınoğlu, Ü. (2010). The farms in rough Cilicia in the Roman and Early Byzantine periods. Adalya, (13), 243-282.
20. Durugönül, S., & Mörel, A. (2012). Evidence of Judaism in Rough Cilicia and its associations with Paganism. Istanbuler Mitteilungen, 62, 303-322.
21. Yunus, K., Şenol, H. İ., & Polat, N. (2021). Three-dimensional modeling and drawings of stone column motifs in Harran Ruins. Mersin Photogrammetry Journal, 3(2), 48-52. https://doi.org/10.53093/mephoj.1012937
22. Aydın, A. (2004). Silifke, Sömek Köyü Kiliseleri Yüzey Araştırması 2003. Anadolu Akdenizi Haberleri, 110-112.
23. Fairchild, M. R. (2014). The Jewish Communities in Eastern Rough Cilicia. Journal of Ancient Judaism, 5(2), 204-216. https://doi.org/10.30965/21967954-00502007